# HOT DUST OBSCURED GALAXIES ENVIRONMENTS

**TESIS PRESENTADA POR**

**DEJENE ZEWDIE WOLDEYES**

**AL**

**INSTITUTO DE ESTUDIOS ASTROFÍSICOS**

**FACULTAD DE INGENIERÍA Y CIENCIAS**

**Para optar al Grado de Doctor en Astrofísica**

**Profesor guía: Roberto J. Assef**

**UNIVERSIDAD DIEGO PORTALES**

**Santiago, Chile**

**2023**

# Hot Dust Obscured Galaxies Environments

A Thesis submitted in partial fulfillment of the requirements of
a Ph.D Degree in Astrophysics
at Instituto de Estudios Astrofísicos

by

**Dejene Zewdie Woldeyes**
Instituto de Estudios Astrofísicos
Facultad de Ingeniería y Ciencias
Universidad Diego Portales

Supervised By

**Prof. Roberto J. Assef**
Instituto de Estudios Astrofísicos
Facultad de Ingeniería y Ciencias
Universidad Diego Portales

Santiago, 2023

# Hot Dust Obscured Galaxies Environments

*by*

**Dejene Zewdie Woldeyes**

Instituto de Estudios Astrofísicos

Facultad de Ingeniería y Ciencias

Universidad Diego Portales

*Supervisor:*

**Roberto J. Assef**

Instituto de Estudios Astrofísicos

Facultad de Ingeniería y Ciencias

Universidad Diego Portales

## Examiners' Committee

| Name and affiliation | Signature |
| --- | --- |
| **Prof. Isabelle Gavingnaud**<br>Facultad de Ciencias Exactas<br>Universidad Andrés Bello. | . . . . . . . . . . . . . . . . . . . . |
| **Prof. Valentino Gonzalez**<br>Departamento de Astronomía<br>Universidad de Chile. | . . . . . . . . . . . . . . . . . . . . |
| **Dr. Claudio Ricci**<br>Instituto de Estudios Astrofísicos<br>Facultad de Ingeniería y Ciencias<br>Universidad Diego Portales | . . . . . . . . . . . . . . . . . . . . |
| **Dr. Manuel Aravena**<br>Instituto de Estudios Astrofísicos<br>Facultad de Ingeniería y Ciencias<br>Universidad Diego Portales | . . . . . . . . . . . . . . . . . . . . |

Date: October 2023

With profound honor and deep remembrance, this endeavor is dedicated to the cherished memory of my late father, Zewdie Woldeyes. His unwavering commitment and substantial sacrifices to nurture my education, even though he didn't have the opportunity for contemporary learning, remain an everlasting source of inspiration for our family.

I love you, DAD!

The only way to be actually win is to get better each day.

- Bill Walsh

# Acknowledgment

Embarking on the journey of studying and writing a Ph.D. thesis is a profound experience, marked by challenges, growth, and countless moments of discovery. This academic odyssey has been made all the more meaningful by the presence and support of some remarkable individuals and groups. As I reflect on this transformative experience, I am honored and deeply grateful to those who contributed significantly to shaping my academic path.

First and foremost, I express my gratitude to my academic advisor, Prof. Roberto J. Assef, for accepting me into his group. During my Ph.D. studies journey, he provided unwavering support, guidance, and enthusiasm. I truly appreciate his invaluable advice and unwavering encouragement, which played a pivotal role in shaping the direction of my research and fostering my academic growth. He is not only my academic advisor; he was also there during my challenging times. His guidance and unwavering support have been instrumental in shaping my academic journey and personal growth, and for that, I am truly grateful.

I would like to express my gratitude to our first Ph.D. program Director, Prof. Lucas Cieza. Especially, during the beginning of my Ph.D. studies and throughout the COVID-19 pandemic, he provided support, and words of wisdom, and guided me through my struggle; his support was crucial for me. I also extend my heartfelt gratitude to Dr. Paula Jofré, my non-academic mentor (during the pandemic), whose unwavering support and reassuring conversations during the COVID-19 pandemic were a beacon of hope and strength throughout those challenging times. Her empathy and guidance made a profound impact on my well-being and determination.

I extend my gratitude to Dr. Tanio Diaz-Santos for all the scientific and psychological support at the beginning of my Ph.D. study journey and my life in Santiago. I thank Dr. Chira Mazzucchelli for her support since we first met at the beginning of my PhD studies when she gave a seminar at UDP in 2019. I am also thankful to Alessia Tortosa and my non-academic mentor, Dr. Camilla Eldridge, for their valuable discussions on both academic and non-academic topics.

I thank Kriti, with whom I shared this academic journey from the beginning. I would also like to extend thanks to Grace, Prachi, Trystan, and Manuel for their unlimited support and friendly encouragement. Special thanks should be given to Danelie for her support in taking me to the observatory to gain observing experience.

To all my family members, whose unwavering love and support have been my anchor throughout this pursuit, I want to express my deepest gratitude, especially to my incredible sisters, Tigist and Likelesh, and my amazing mom, Desta and brother, Gizaw. Their unwavering understanding, boundless patience, and constant encouragement have been the driving force behind my success in achieving my Ph.D.

I thank the small group of the Ethiopian community in Chile (Tamrat, Yosef, Mihret, and Messay), for their moral support during my Ph.D. study journey.

I thank Ana for organizing the football game and the UDP football group for creating an amazing experience; we had a great time, and thank you.

And finally, I would like to thank and extend my appreciation to my friends Kidist (Kidi), Emirt, and Shewayiref who have cheered

me on and offered moral support throughout this journey. I also want to extend my thanks to my friends Tilahun and Alene (Ph.D. candidate, SSGI-EORC) whose belief in me has been a source of motivation and strength.

# Abstract

In the realm of astrophysics, galaxy evolution is a fundamental process marked by the complex interactions of various physical mechanisms, including star formation, mergers, and interactions with the intergalactic medium. This cosmic process plays a pivotal role in our understanding of the evolution of galaxies throughout cosmic epochs, contributing to our comprehension of the universe.

In the first project of this thesis, we studied the physical properties of galaxies with faster inside-out assembly at lower redshifts using publicly available imaging and spectroscopy data, such as the Sloan Digital Sky Survey (SDSS) Data Release 8 (DR8) MPA-JHU catalog, the Wide-field Infrared Survey Explorer (WISE), the Galaxy Evolution Explorer (GALEX), and Galaxy Zoo. We studied a sample of 48,127 Inside-Out Assembled Galaxy (IOAG) candidate galaxies within a stellar mass range of $\log M* = 10.73 - 11.03 M_\odot$ and redshift $z < 0.1$. We classified our samples using optical spectroscopy and found that 20% were star-forming galaxies, 40% were Active Galactic Nuclei (AGN), and 40% were composite galaxies.

Additionally, we split them based on their morphology and although about half of them had uncertain classifications in Galaxy Zoo. Of the rest, the majority (37%) are classified as spirals, and the remaining ones are elliptical (12%). Among the BPT-classified star-forming IOAG candidates, the majority display spiral morphologies and align with the main sequence. While Seyfert 2 and composite galaxies also predominantly exhibit spiral morphologies, they, in contrast, exhibit quiescent star formation rates (SFRs). Our analysis further revealed that most IOAG galaxies fall below the main sequence of star formation, residing within the green valley or red sequence.

Our analysis suggests that a substantial fraction of IOAG candidates may currently be undergoing quenching, transitioning from the blue cloud to the red sequence. Notably, AGN-classified candidates consistently demonstrate lower SFRs in comparison to star-forming galaxies, hinting at a potential correlation between the AGN activity and the quenching process. However, the spiral morphology of these galaxies remains unaltered, indicating that central star formation is suppressed before any noticeable morphological transformation occurs.

The other two studies of this thesis, were dedicated to studying the overdensity of Lyman Break Galaxies (LBGs) around 3 of the most luminous Hot Dust-Obscured Galaxies (Hot DOGs) known. In one study, we used deep Gemini Multi-Object Spectrographs South (GMOS-S) imaging in $r$-, $i$-, and $z$-bands to estimate the surface density of companion LBGs and probe the Mpc-scale environment of WISE J224607.56–052634.9 (W2246–0526) to characterize its richness and evolutionary state. We identified LBG candidates in the vicinity of W2246-0526 using the selection criteria developed by Ouchi et al. (2004) and Yoshida et al. (2006) in the Subaru Deep Field (SDF) and in the Subaru XMM-Newton Deep Field (SXDF), slightly modified to account for the differences in filters used, and we found 37 and 55 LBG candidates, respectively. We estimated the overdensity of LBGs around the W2246–0526, $\delta = N_{found}/N_{expected}$, to be $\delta = 7.1^{+1.1}_{-1.1}$ ($\delta = 5.1^{+1.2}_{-1.2}$) when compared with the O04 study of the SDF (SXDF). compared with the Y06 study of the SDF field, we found $\delta = 5.2^{+1.4}_{-1.4}$ . The average overdensity is hence $\delta = 5.8^{+2.4}_{-1.9}$. Our findings suggest that this Hot DOG lives in an overdense environment.

In a follow-up study, we used deep Inamori-Magellan Areal Camera

and Spectrograph (IMACS) imaging in the $g$-, $r$,- and i-bands for WISE J041010.60–091305.2 (W0410–0913) at $z = 3.631$ and WISE J083153.25+014010.8 (W0831+0140) at $z = 3.912$ to study LBGs located therein. We optimized the selection function for the redshift of each Hot DOG using the Cosmic Evolution Survey (COSMOS2020) catalog. We also reanalized the observations of W2246-0526 but now optimizing the selection function in the same manner. The optimization of the photometric selection criteria only considered sources fainter than those Hot DOGs. Since LBGs are unlikely to be brighter, we also consider sources fainter to have been detected with our observations.

Comparing the density of LBG candidates with that of the COSMOS2020 blank field, we estimate an overdensity of sources surrounding each Hot DOG, considering both without ($\delta$) and with possible contaminants ($\delta'$) in the COSMOS field. This corresponds to the entire field of view (the maximum area that keeps the Hot DOG at the center in all directions, only for W0410–0913 and W0813+0140). For W0410–0913, we found $\delta = 1.56^{+0.12}_{-0.12}$ and $\delta' = 5.37^{+0.95}_{-0.95}$ ($\delta = 2.47^{+0.35}_{-0.35}$ and $\delta' = 12.44^{+4.31}_{-4.31}$). For W0813+0140, we found $\delta = 4.62^{+0.36}_{-0.36}$ and $\delta' = 30.83^{+6.39}_{-6.39}$ ($\delta = 5.29^{+0.82}_{-0.82}$ and $\delta' = 36.00^{+14.9}_{-14.9}$). For W2246–0526, we found $\delta = 2.12^{+0.40}_{-0.40}$ and $\delta' = 6.88^{+2.6}_{-2.6}$.

Our analysis of the two Hot DOGs observed with IMACS, W0410–0913 and W0813+0140, revealed a steep decline in overdensity beyond a physical scale of $\sim 1.4$ Mpc. We also observed a similar steep decline in the overdensity of LBG candidates around W2246–0526, occurring beyond a physical scale of $\sim 0.5$ Mpc when using an optimized selection function. However, in our previous study, where we used modified selection criteria and the Subaru field as a blank field, we were unable to see this profile. We were unable to confirm

this pattern for W2246-0526 using both (optimized and modified) selection functions. Furthermore, this radial profile does not resemble what we observe in a larger field of view. Nevertheless, this radial density profile may provide valuable insights into the selection function and broader structure of the cosmic environment.

The results of our studies are broadly compatible with two earlier studies of Hot DOG environments, and together show that Hot DOGs live in quite dense regions of the Universe. We conclude that Hot DOGs are an excellent tracer of protoclusters

# Table of Contents

# List of Figures

# List of Tables

# Chapter 1

# Introduction

Galaxies are the building blocks of the universe, and their formation and evolution is a complex process that has been widely explored using both theoretical models and observational studies. The hierarchical structure formation theory is a widely accepted explanation for how large-scale structures, such as galaxies and galaxy clusters, formed in the universe. According to this theory, structures form through a bottom-up process, where small density fluctuations in the early universe serve as the seeds for the formation of larger structures. Under the influence of gravity, regions with slightly higher density attracted more matter through gravitational collapse. As matter accumulated in these regions, they became denser and eventually led to the formation of bound objects such as proto-stars and gas clouds. As the proto-stars formed and gas clouds collapsed further, they eventually gave rise to the first galaxies. The galaxies themselves continued to grow through mergers with other galaxies and the accretion of gas and matter from their surroundings. This hierarchical process of merging and accretion led to the formation of larger and more massive structures like galaxy clusters. The hierarchical structure formation theory is supported by observations,

such as the distribution of galaxies in the universe and the cosmic microwave background radiation.

This chapter provides a concise overview of several key topics. In Section 1.1, we will explore the nature of Active Galactic Nuclei (AGNs), shedding light on their characteristics and classifications. Section 1.2, focuses on the growth and evolution of galaxies, highlighting the underlying physical processes and structures. We will provide a brief overview of extremely luminous obscured galaxy populations, examining their unique properties and their significance in understanding the universe, in Section 1.3. In Section 1.4, we will discuss the tracing of the cosmic environment, exploring how the distribution and properties of high redshift star-forming galaxies provide insights into the large-scale structure of the universe, the evolution of cosmic structures, and the characteristics of dark matter. Finally, in Section 1.5, we provide our motivation and aims to survey LBGs in the vicinity of three Hot DOGs to better characterize the richness and evolutionary state of their environment.

## 1.1 Active Galactic Nuclei

Active Galactic Nuclei (AGN) are incredibly luminous and energetic central regions of galaxies. They are powered by accretion of matter onto a supermassive black hole (SMBH) at the center of the galaxy. They play a crucial role in understanding galaxy evolution and the interaction between massive black holes and their host galaxies. AGN exhibit a wide range of observational characteristics, leading to the development of several classification schemes to categorize these objects based on their properties.

### 1.1.1 AGN Classification and AGN Unification Models

The study of AGN spans several decades, dating back to Seyfert (1943) whose groundbreaking research unveiled the presence of strong emission lines in the spectra of specific spiral galaxies. Seyfert (1943) classified two main types: Type 1, characterized by broad emission lines, and Type 2, with narrower lines. Although this work laid the foundation for AGN studies, the nature of these objects remained enigmatic. Expanding upon this initial breakthrough, Schmidt (1963) discovered the actual nature of the quasi-stellar radio source, known as a quasar, by demonstrating that the spectrum of the radio source 3C 273 was highly redshifted. This implication pointed to an enormous distance and a tremendous amount of energy being emitted from the object. After a few years, Schmidt (1968) introduced the distribution in space, as well as both the optical and radio luminosity functions of quasi-stellar radio sources. This contribution offered a better understanding of quasar populations, their evolution over cosmic time, and their role in the broader context of galaxy formation and cosmic evolution. This interpretation correctly identifies this source as a quasar, which is a type of AGN with extremely high luminosity and redshifted spectra. This discovery revolutionized our understanding of AGN.

After the discovery of quasars, Lynden-Bell and Rees (1971) proposed that the black-hole model of galactic nuclei be considered a crucial component of the broader unification framework. It posits that SMBHs at the centers of galaxies are responsible for the extreme energy outputs observed in AGN.

Building upon this, Antonucci (1993) introduced a groundbreaking

unification model for AGN classification, suggesting that the observed differences between Seyfert Type 1 and Type 2 galaxies result from orientation rather than intrinsic properties. According to this model, the same central engine is present in both types of galaxies, but Type 2 galaxies are observed edge-on, which obscures the broad-line region responsible for their spectra. This unified framework helped reconcile the diversity of AGN characteristics.

Furthermore, Urry and Padovani (1995) made a significant contribution that advanced our understanding of AGN studies by emphasizing the importance of multiwavelength observations. Their work further supported the unification model by demonstrating that the observed differences between AGN types were due to orientation effects rather than intrinsic variations. They highlighted the necessity of studying AGN across different wavelengths, from radio to gamma rays, to gain a comprehensive understanding of their complex structures and mechanisms.

Expanding on this unification model, Nenkova et al. (2008a,b) presented a significant advancement in AGN dusty torus study. Their study introduces a detailed framework regarding the observational implications of clumpiness in the dusty torus AGN. It explains how considering the geometry of the dusty torus and radiative transfer effects contributes to a broader range of observational characteristics within AGN studies. Specifically, the study focuses on incorporating the role of the dusty torus in shaping the observational properties of AGN from the perspective of the torus itself and its intricate interaction with the radiation emitted by the central engine. This approach offers a more realistic and comprehensive understanding of the diverse nature of AGN.

AGNs can be extremely powerful, with some being the most luminous objects in the universe. According to the unified model (Antonucci, 1993), AGNs are classified based on the line-of-sight obscuration towards the accretion disk. This central region is surrounded by a toroidal structure of dust and gas, which can lead to vastly different appearances when observed from different viewing angles. Depending on how much dust is found along the line of sight, AGNs can be classified into two main types (although intermediate types are also common in the literature). Type 1 AGNs are those in which we have a direct line of sight towards the central engine, while Type 2 AGNs correspond to those in which dusty clouds block our view of the accretion disk and the broad-line region. Canonically, Type 1 AGNs are considered to be viewed face-on, and Type 2 AGNs are considered to be viewed edge-on, although the specific relation between the observing angle and type depends on the detailed distribution of the dusty clouds.

Ramos Almeida and Ricci (2017) provides a comprehensive overview of the intricate structure and properties of the material surrounding accreting SMBHs in AGN. Their research focuses on nuclear obscuration in AGNs, drawing insights from infrared and X-ray investigations of local AGN. Ramos Almeida and Ricci (2017) revealed that from the infrared perspective, this obscuring material acts as a mediator between the broad- and narrow-line regions, often composed of both an equatorial disk/torus and a polar element. Conversely, observations in the X-ray domain indicate that the obscuration arises from multiple absorbers across various spatial scales, predominantly linked to the torus and the broad-line region. They outlined the principal AGN structures observed in both equatorial and polar directions, covering the range from the center to the scales

of the host galaxy. These structures include the SMBH, accretion disk and corona, broad-line region (BLR), torus, and narrow-line region (NLR), as shown in Figure 1.1, which presents a schematic of the gaseous and dusty structures within AGNs.
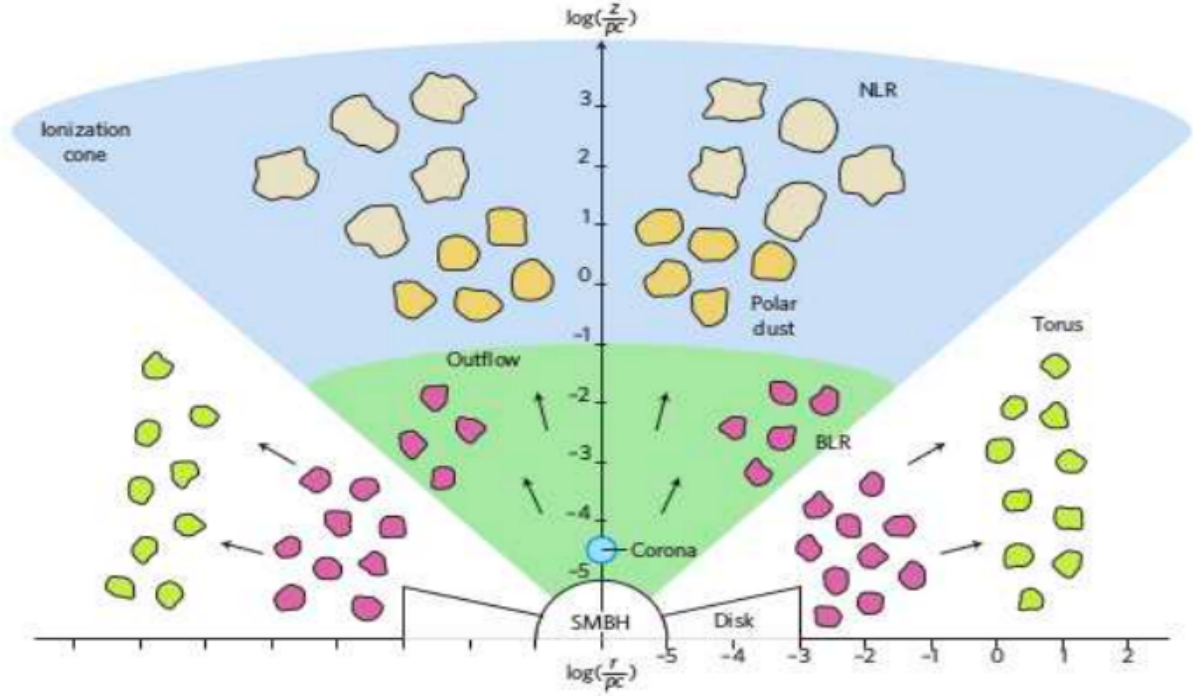


FIGURE 1.1: Adapted from Ramos Almeida and Ricci (2017), this is a physical model of an AGN, showing the broad scales of the key regions. The central structure of an AGN includes the compact accretion disk around the black hole, the accretion disk and corona, the BLR, the NLR, and the torus.

AGNs display a wide variety of spectral features due to the diverse physical conditions and geometries around the central black hole. Optical spectroscopy allows us to select and classify AGNs into two types based on the presence and characteristics of these features. The empirical model developed by Baldwin-Phillips-Terlevich (BPT; Baldwin et al., 1981) diagram is a widely used tool for classifying AGNs based on their emission line ratios. It involves the flux ratios of emission lines, such as $[OIII]\lambda5007/H\beta$ versus $[NII]\lambda6583/H\alpha$, or $[SII]\lambda6716, 6731/H\alpha$ or $[OI]\lambda6300/H\alpha$ (e.g., Baldwin et al., 1981, Kauffmann et al., 2003, Kewley et al., 2006, Schawinski et al., 2007,

Zewdie et al., 2020). The position of a point on the BPT diagram corresponds to the ionization mechanism responsible for the observed emission lines. The different regions on the diagram are associated with distinct types of ionization sources, such as star-forming regions, Seyfert galaxies, and Low-Ionization Nuclear Emission-line Regions (LINERs).

The Wide-field Infrared Survey Explorer (WISE) is a sky-mapping mission launched in 2009, which has made significant contributions to our understanding of the infrared universe (Wright et al., 2010). One of its notable missions is the identification of the most luminous and dusty galaxies in the process of formation, known as ultraluminous infrared galaxies (Eisenhardt et al., 2012). By analyzing the infrared colors of sources detected by WISE, Assef et al. (2013) were able to distinguish active galactic nuclei (AGNs) from other sources of infrared emission, such as star-forming galaxies and cool interstellar dust. This technique has proven to be highly effective in identifying a large population of AGNs across the sky. In line with this, a comprehensive WISE AGN catalog was presented in Assef et al. (2018).

Over the years, studies of AGNs have advanced considerably, driven by improvements in observational technology and theoretical models. Padovani et al. (2017) presented a more comprehensive classification of AGN (see the AGN classes in their Table 2). They provided observations of AGNs in different electromagnetic bands, which give us unique signatures that help us understand the properties of AGNs and their role in galaxy evolution.

## 1.2   Galaxy Growth and Evolution

The intricate interplay of galaxy mergers and interactions propels transformative processes that shape the evolution of galaxies across cosmic time (Toomre and Toomre, 1972). Gravitational forces that bring galaxies into proximity trigger tidal forces, gas collisions, and stellar interactions. These processes result in significant physical and structural features within the merged system, leading to morphological changes that contribute to the remarkable diversity of galaxy shapes observed throughout the universe.

Galaxy assembly involves the mergers and interactions between galaxies, which drive the growth of larger and more massive galaxies. This process of hierarchical merging of galaxies implies that the environment in which galaxies are born and live can play a fundamentally important role in their evolution. This is evident at low redshifts, where the morphology-density relation (Dressler, 1980) shows that early-type galaxies are more abundant in higher-density environments, while late-type galaxies are more commonly found in lower-density regions. This relation indicates that as we move to denser environments, such as the cores of galaxy clusters and groups, we tend to find more Elliptical and S0 galaxies, whereas star-forming spirals are more frequently found in the less-dense outskirts of clusters and groups.

The strong link between color and morphology provides indications of the star formation timescales and processes that drive morphological transformation. Further insight into these processes comes from the observation that this relation evolves with redshift. For instance, the cores of high-redshift galaxy clusters have a larger fraction of blue galaxies than the cores of low-redshift galaxy clusters

(Butcher and Oemler, 1984). Numerous processes associated with local density can quench star formation in spiral galaxies. In cluster environments, for example, ram pressure stripping or harassment can heat up and remove the cold gas a galaxy needs to maintain its star-formation activity. Some galaxies may also quench their star formation by depleting their cold gas, a supply that is cut off through starvation or strangulation (Larson et al., 1980, Bekki et al., 2002).

Numerical simulations have been used to explore starburst activities arising from gaseous inflows during comparable-mass disk galaxy mergers. Mihos and Hernquist (1996) reveal the pivotal role of internal galaxy structures compared to orbital geometry. Galaxies possessing dense central bulges, in this context, exhibit more pronounced inflows occurring later in the process. Conversely, interactions drive significant dissipation and gas inflow after the merger has taken place. These findings are consistent with insights from observations of ultraluminous infrared galaxies, as discussed by Mihos and Hernquist (1996).

Di Matteo et al. (2005) demonstrated a simulation of how galactic collisions trigger quasars and influence the growth of SMBHs. These simulations link black hole mass-velocity dispersion to gas inflows that fuel quasars, subsequently limiting star formation and black hole growth. Galactic mergers also profoundly impact the growth of SMBHs. During mergers, flowing gas and stars can fuel the central SMBHs, leading to the formation of AGN that releases substantial energy. This AGN activity influences gas dynamics and star formation, and it may even halt further gas inflow. This highlights the intricate relationship between SMBH growth, AGN activity, and broader galactic processes.

Hopkins et al. (2008) studied the connection between galaxy mergers, quasar activity, and the formation of elliptical galaxies within the framework of cosmological evolution. They identified correlations, patterns, or trends indicating that particular stages of galaxy mergers are linked to increased quasar activity. Additionally, their findings suggested that specific conditions are necessary for both processes to occur simultaneously.

Alexander and Hickox (2012) studied the driving mechanisms behind the growth of black holes. They presented schematic diagrams, as shown in Figure 1.2, to illustrate several significant mechanisms believed to initiate AGN activity. These mechanisms include the occurrence of major mergers involving gas-rich galaxies, gradual internal changes within galaxies, and secular evolution driven by interactions between smaller galaxies. Additionally, the concept of hot halo accretion is considered the primary mode of black hole growth for low-excitation radio-loud AGNs.

### 1.2.1 Galaxies at High Redshifts

Every massive galaxy seems to have a central SMBHs, which is a central black hole with a mass in excess of $\sim 10^6 \ M_\odot$, and accretion of gas onto this central SMBH can create a significant amount of radiative energy. An actively accreting SMBH is commonly referred to as an AGN. SMBHs grow the majority of their mass through AGN activity and mergers. Furthermore, there are indications that luminous AGN activity is linked to galaxy mergers (Treister et al., 2012), although the causality of such relation is still a matter of debate. However, what is clear is that AGN activity in merging
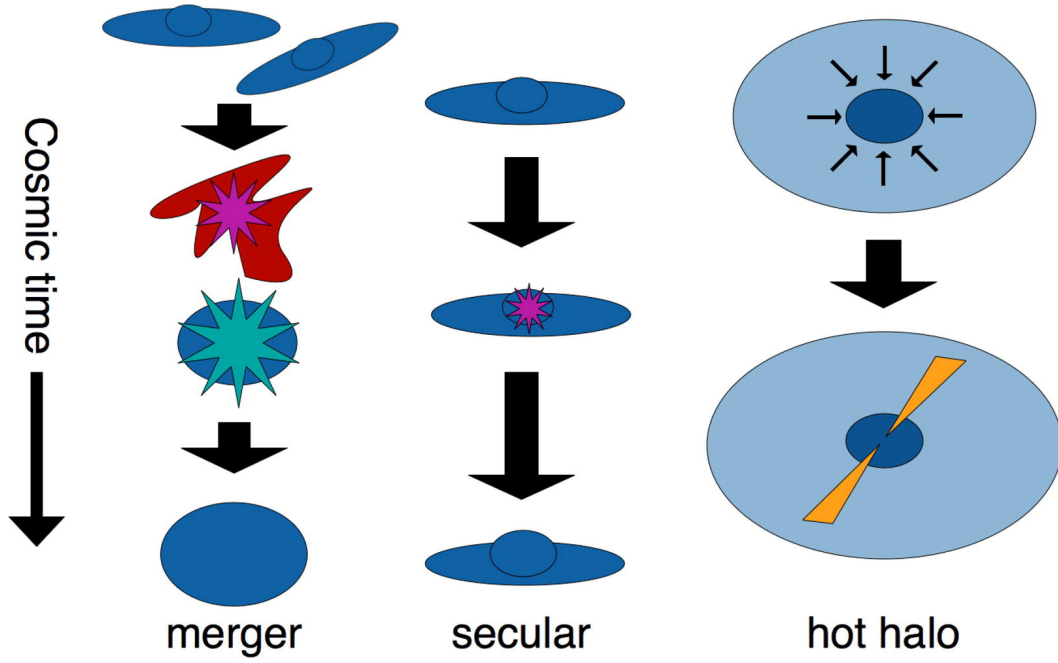
FIGURE 1.2: Adapted from Alexander and Hickox (2012), schematic diagrams illustrate the large-scale processes triggered by AGN activity: Major Mergers - when gas-rich galaxies merge, they trigger AGN activity on a large scale; Secular Evolution - this involves internal and external processes, where internal changes within a galaxy and interactions with other galaxies contribute to AGN activity; Hot Halo Accretion - serving as the primary mode of black hole growth for low-excitation radio-loud AGNs, it involves the accretion of material from their surroundings.

galaxies is obscured (Ricci et al., 2017), both by dust in the optical and UV wavelengths, as well as by atomic gas in the X-rays. Models (e.g., Hopkins et al., 2008, Croton et al., 2006) suggest that AGN activity plays an important role in quenching star-formation in massive galaxies through a process referred to as AGN feedback, on which the energy released from the AGN (either radiatively or mechanically through jets) heats and remove the cold gas reservoirs. According to some of these models (e.g., Hopkins et al., 2008), major mergers trigger intense episodes of star formation and obscured AGN activity. This obscured AGN activity grows in intensity to the point where it can generate enough feedback to quench star formation. The combination of major mergers and strong AGN feedback would then be responsible for the transition of blue-cloud spirals to red-sequence ellipticals.
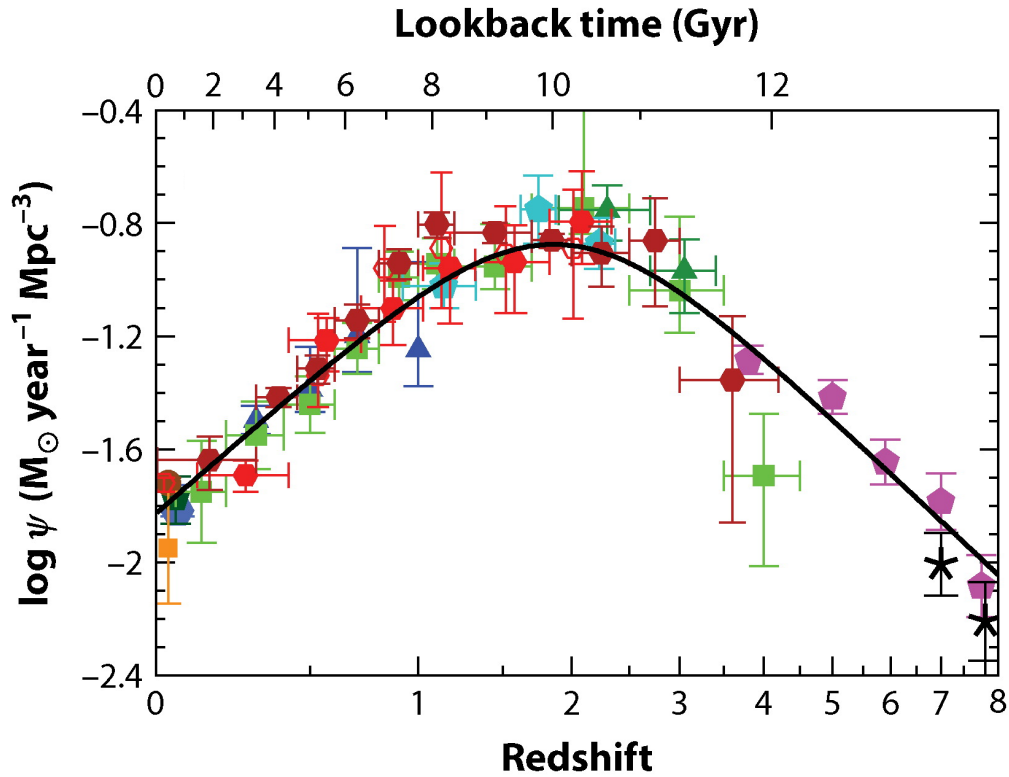
FIGURE 1.3: Adapted from Madau and Dickinson (2014), the history of cosmic star formation FUV and IR rest-frame measurements.

Madau and Dickinson (2014) investigated the evolution of the cosmic SFRD by combining FUV measurements from the Hubble Space Telescope (HST) and the Galaxy Evolution Explorer (GALEX). This study provided comprehensive insights into the evolution of cosmic star formation using FUV and IR rest-frame measurements. Through these measurements, the history of cosmic star formation has yielded profound insights into the evolution of galaxies and the Universe. By exploring the history of cosmic star formation, valuable insights emerge into the underlying physical processes that have shaped the universe as perceived today. It is worth noting that FUV emission mainly originates from young, massive stars, while IR emission traces reprocessed light from dust-obscured star formation. Figure 1.3 visually demonstrates that the SFRD reaches its peak at cosmic noon, indicating a vibrant era of star formation in the early

universe. Notably, FUV and IR rest-frame wavelengths provide two crucial observational windows for studying this cosmic history.

Vito et al. (2018) conducted a study focusing on the comparison between the evolution of AGN and galaxy density. They revealed a connection between the decline in high-luminosity AGN and the characteristics of the galaxy population. Furthermore, they posited that evolving parameters might be responsible for driving nuclear activity in lower-luminosity AGN. As shown in Figure 1.4, an interesting discovery from the study by Vito et al. (2018) is the comparison with the previously observed parallel evolution between black hole accretion rate density and star formation rate density, a trend consistently noted during cosmic noon.
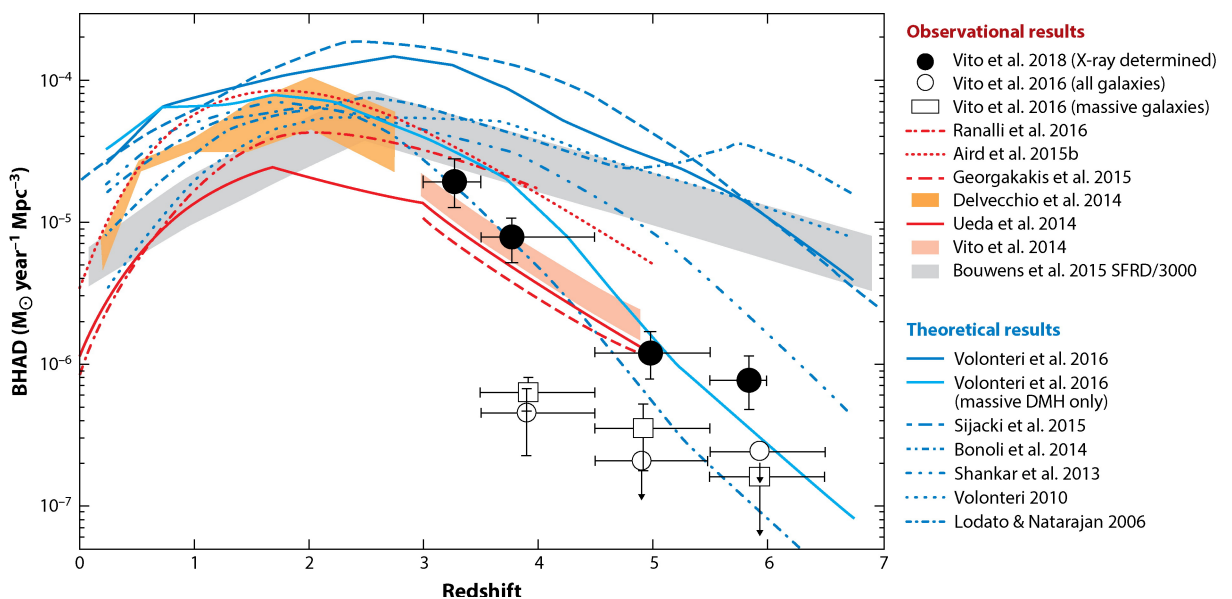


FIGURE 1.4: Adapted from Vito et al. (2018), illustrate the derivation of black hole accretion rate density from X-ray-detected AGN, comparing it with observational and theoretical results.

During cosmic noon, a crucial epoch, both cosmic SFRD and AGN activity peak, as depicted in Figure 1.3 and Figure 1.4, respectively. This convergence can be attributed to the increased occurrence of galactic mergers during this period. Mergers, prevalent at this cosmic epoch, play a dual role: they trigger intense bursts of star formation

due to enhanced gas inflows and gravitational interactions, while also facilitating the fueling of SMBHs. Consequently, this process drives AGN activity and contributes to the observed emissions from accreting matter.

## 1.3  Special type of Obscured AGN

Hot dust-obscured galaxies (Hot DOGs; Eisenhardt et al., 2012, Wu et al., 2012) are a rare population of hyper-luminous, heavily dust-obscured quasars identified through observations by WISE (Wright et al., 2010) mission. WISE, launched in December 2009, is a space telescope that conducted a comprehensive survey of the entire sky using four infrared bands, with $5\sigma$ point-source sensitivities of 0.08, 0.11, 1, and 6 mJy at 3.4, 4.6, 12, and 22 $\mu$m, respectively. These bands are referred to as W1, W2, W3, and W4 (Wright et al., 2010, Eisenhardt et al., 2012). The survey was conducted in a single coverage on the ecliptic, consisting of eight or more exposures at each sky location (Wright et al., 2010). Sensitivity improves further from the ecliptic due to denser exposure overlap and a lower zodiacal background. Due to their obscuration, these objects are selected to be strongly detected in W3 and W4 but are faint or not detected at all in W1 and W2. Hot DOGs have a bolometric luminosity of $10^{13}\mathrm{L}_\odot$ and even exceed $10^{14}\mathrm{L}_\odot$ (Tsai et al., 2015), are powered by accretion onto SMBHs buried under enormous amounts of gas and dust, making them close to Compton-thick in the Xrays (Stern et al., 2014, Assef et al., 2015, 2016, 2020, Piconcelli et al., 2015).

### 1.3.1    Selection of Hot Dust-Obscured Galaxies

The selection of Hot DOGs using the "W12 dropout" technique is a method specifically designed to identify these heavily obscured galaxies. The selection criteria for these "W1W2-dropouts" are as follows: Specifically, the quasars must have a fainter W1-band magnitude ($W1 > 17.4$) Vega mag and either:

$$W4 < 7.7, \text{ and } W2 - W4 > 8.2 \tag{1.1}$$

or

$$W3 < 10.6, \text{ and } W2 - W3 > 5.2 \tag{1.2}$$

Figure 1.5 shows the color-color distribution of the detected objects using WISE, illustrating various types (left-panel) and the W12-dropout (right-panel). The majority of the selected W12-dropouts are at $z > 1.6$ (Eisenhardt et al., 2012).
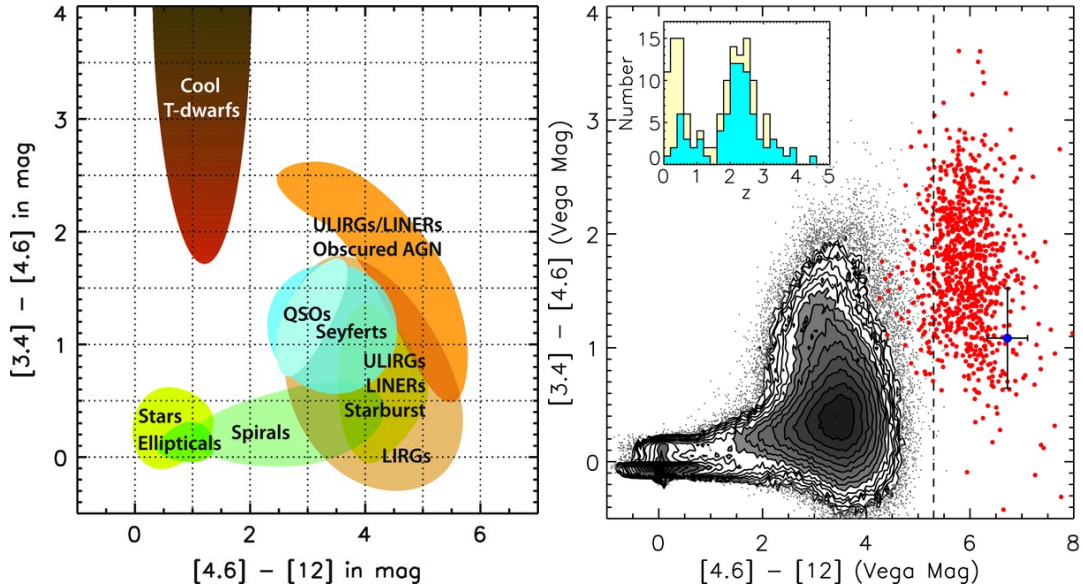


FIGURE 1.5: Left panel: shows the positions of various intriguing class objects in the color-color diagram, adapted from Wright et al. (2010). Right panel: Adapted from Eisenhardt et al. (2012), it displays detected sources with $< 0.3$ errors in all WISE bands (black points and gray regions), while the red dots represent W1W2-dropouts selected over the whole sky, excluding the Galactic plane and bulge.

### 1.3.2 Hot Dust-Obscured Galaxies Environment

Several observational techniques have been used to investigate the environments of Hot DOGs, shedding light on their nature and significance in our understanding of galaxy evolution. The environment of Hot DOGs has been probed through sub-mm observations. Jones et al. (2014, 2017) used sub-mm galaxies to assess the environments of these objects. They found evidence of an overdensity of sub-mm galaxies around a small sample of Hot DOGs using 850 $\mu$m observations with SCUBA-2 at JCMT. Sub-mm observations are particularly useful for identifying heavily dust-obscured regions within galaxies, providing crucial information about the distribution of dust and its impact on star formation and quasar activity. The intense star formation observed in Hot DOGs is believed to be triggered by major galaxy mergers (Díaz-Santos et al., 2016).

Assef et al. (2015) conducted a statistical analysis to study the field density in the vicinity of a large sample of Hot DOGs using deep Warm Spitzer/IRAC imaging, comparing it with two control samples: (1) random pointings in the Warm Spitzer UKIDSS Ultra Deep Survey (SpUDS) and (2) Galaxy Clusters Around Radio-loud AGN survey (CARLA; Wylezalek et al., 2013). They found that Hot DOGs have a similar density distribution to the CARLA sources (see Figure 1.6). However, they also discovered that Hot DOGs are significantly denser than field galaxies (Assef et al., 2015), suggesting that the environment of Hot DOGs is notably dense and akin to that of radio-loud AGNs. As shown in Figure 1.6, the density distribution of Hot DOGs significantly exceeds that observed in the random pointing, implying that the environment of Hot DOGs is significantly denser than that of field galaxies. The Hot DOGs exhibit
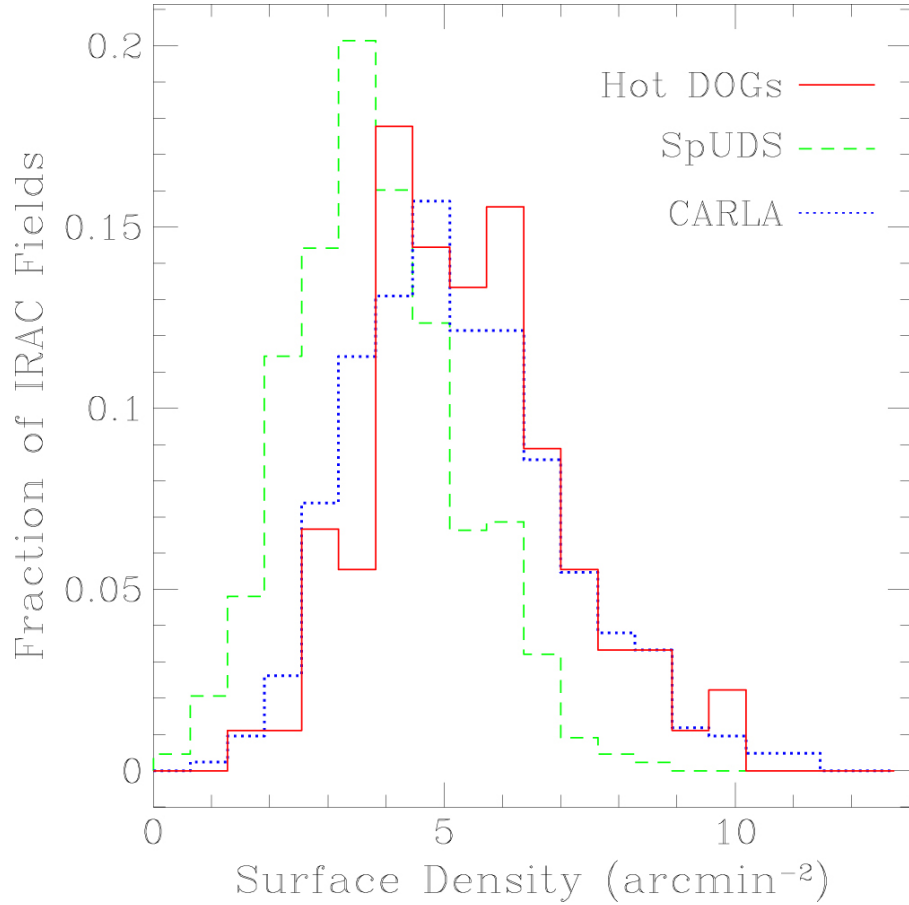
FIGURE 1.6: Adapted from Assef et al. (2015), the fraction of Hot DOGs with IRAC observations with a given number density (solid red). The distribution for all objects in the CARLA survey (dotted blue) and for a sample of randomly selected positions in the SpUDS survey (dashed green).

a strong agreement with the CARLA sources, indicating that Hot DOGs inhabit environments similar to those of radio-loud AGNs.

Deep Atacama Large Millimeter/submillimeter Array (ALMA) observations of W2246-0526, as presented by Díaz-Santos et al. (2016, 2018), have revealed three spectroscopically confirmed companion galaxies with disturbed morphologies and three sources with companions within ∼30 kpc. The presence of these three companions, and the detection of dust emission streams, suggest that W2246-0526 is in the process of accreting its neighbors and resides at the center of a proto-cluster.

Recently, Ginolfi et al. (2022) used MUSE/VLT observations of W0410–0913 and identified 24 Ly$\alpha$-emitting galaxies around the Hot DOG within a 0.4 Mpc radius. They reported an overdensity of $\delta = 14^{+16}_{-8}$ of LAEs around W0410–0913.

Additionally, Luo et al. (2022) conducted a study on the environment of the Hot DOG W1835+4355 at a redshift of $z = 2.3$. They employed the wide-field infrared camera on the Palomar 200-inch telescope and identified a significant excess in the number density of distant red galaxies (DRGs) in the field containing W1835+4355. This overdensity is twice that of the blank field data. Multiwavelength observations of Hot DOGs have statistically shown that these objects are likely to live in dense environments (Assef et al., 2015, Jones et al., 2014, 2017, Finnerty et al., 2020), and could be in a transition phase from starburst galaxies to UV-bright quasars. Notably, however, the number density of Hot DOGs is similar to that of equally luminous type 1 AGN at $2 < z < 4$ (Assef et al., 2015). All of these studies collectively suggest that Hot DOGs can effectively serve as tracers for dense regions at high redshift.

## 1.4 Tracing of Environment

AGN can be so luminous as to be easily identifiable at a very high redshift. Current observational studies have found luminous AGN activity already at the epoch of reionization, implying that very massive SMBHs already existed only a few hundred million years after the Big Bang (e.g., Fan et al., 2023). Mergers and high gas accretion rates, both associated with high-density regions, could be

driving this very rapid growth, but the attempts to study the environments of these objects based on searches for Lyman Break Galaxies (LBGs; Morselli et al., 2014, Husband et al., 2013, Utsumi et al., 2010, Kashikawa et al., 2007, Zheng et al., 2006, Stiavelli et al., 2005, García-Vergara et al., 2017) and Lyman Alpha Emitters (LAEs; e.g., Kashikawa et al., 2007, García-Vergara et al., 2019). However, some studies found no significant excess of galaxies in high redshift quasar fields (e.g., Bañados et al., 2013, Simpson et al., 2014, Mazzucchelli et al., 2017), and other studies finding a mix of overdensities and under-densities in the vicinity of quasars at high redshift (Stiavelli et al., 2005, Kim et al., 2009) have produced a wide variety of results, so the answer is not yet clear. Recently, multi-wavelength studies have found evidence of overdensities around high redshift quasars with VLT/FORS observations of the LBGs and LAEs are strongly clustered around quasars at $z \sim 4$ García-Vergara et al. (2017, 2019) and ALMA observations of gas-rich companions around few quasars at $z \sim 6$ (Decarli et al., 2018) and $z \sim 5$ (Nguyen et al., 2020, Trakhtenbrot et al., 2017). Furthermore, studies of radio-loud quasars at $z \sim 2$ have found them to be good tracers of protoclusters (Wylezalek et al., 2013, Noirot et al., 2016).

### 1.4.1 Lyman Break galaxies

LBGs are highly star-forming galaxies whose spectral energy distributions (SEDs) have a strong break in their ultraviolet SEDs due to either the Lyman break or intergalactic Ly$\alpha$ absorption. LBGs are distant galaxies that are detected using a technique called the Lyman break method. This method relies on the characteristic absorption of ultraviolet light by neutral hydrogen in galaxies, which causes a drop

(break) in the observed spectrum at a specific wavelength known as the Lyman limit. Traditionally, two broad bands are commonly used to identify the Lyman break, one at $\lambda < 912(1+z)$ Å and the other at $\lambda > 912(1+z)$ Å. LBGs are then identified as having a very red color between these filters. In order to minimize contamination from low redshift quiescent galaxies or dusty star-forming galaxies, a third band redwards of the break is added, requiring a flat color between the two reddest bands (Steidel et al., 1995). This identification technique has been widely used in the literature over the past couple of decades with only minor changes. Importantly, however, Ouchi et al. (2004) showed that at $z > 3$, the most notable discontinuity in the SED is caused by intergalactic Lyman alpha absorption rather than by the Lyman break, altering the selection of photometric bands accordingly. LBGs have young ongoing star-forming populations that can be found at high redshift ($2 < z < 5$; Giavalisco, 2002) using ground-based instrumentation. In the last couple of decades, several overdense environments have already been identified through the use of LBGs around quasars and radio galaxies at $z > 2$ (Morselli et al., 2014, Husband et al., 2013, Utsumi et al., 2010, Kashikawa et al., 2007, Zheng et al., 2006, Stiavelli et al., 2005, García-Vergara et al., 2017).

Figure 1.7 shows a composite spectrum of a Lyman Break Galaxy from Shapley et al. (2003), shifted to each redshift, while assuming the mean IGM optical depth at each redshift. The filter curves are from HSC, which we used for the optimization of the selection function.
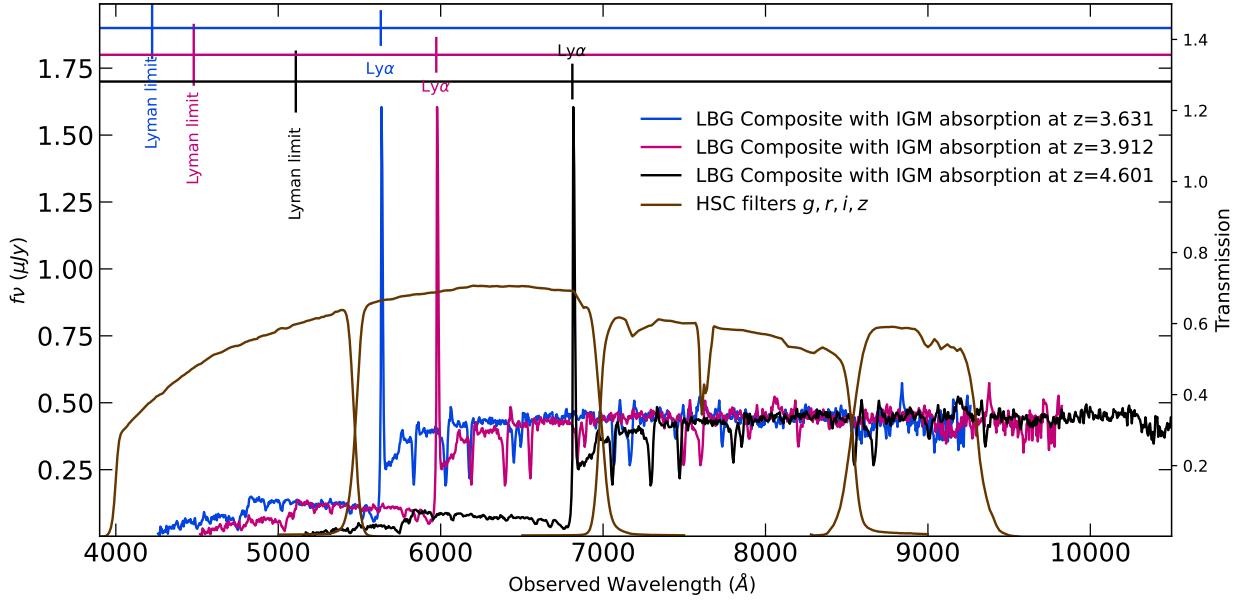
FIGURE 1.7: Composite LBG spectrum of Shapley et al. (2003) is shown with IGM absorption at z = 3 and shifted to three redshifts: $z = 3.631$ (blue solid line), $z = 3.912$ (magenta solid line), and $z = 4.601$ (black solid line), along with the IGM absorption correction based on their respective redshifts. For further details, please refer to Section **??**. Overlayed are the $g$-, $r$-, $i$-, and $z$-bands gray solid lines represent the HSC filter curves are used in the optimization of the selection function.

## 1.5 Objectives and Outline of the Thesis

Observational studies have indicated that both massive galaxies and high-redshift quasars tend to reside in overdense regions of the Universe. However, some studies indicate underdensity (e.g., Bañados et al., 2013, Simpson et al., 2014, Mazzucchelli et al., 2017), leading to ongoing debates about the overdensity around luminous quasars. Statistical studies have suggested that Hot DOGs inhabit dense environments in shallow observations (e.g., Assef et al., 2015), while deep ALMA observations within ∼30 kpc radius reveal local overdensity (Díaz-Santos et al., 2018). Hot DOGs exhibit intense star formation activity and are in a transition phase from starbursts to UV quasars. However, there are currently no larger field studies targeting Hot DOGs or addressing their environments on larger scales (Mpc), which is essential for understanding galaxy formation and

evolution, and the cosmic structures of the early universe. How galaxies form and evolve across cosmic time remains one of the main open questions in extragalactic astronomy. To answer this question, we must understand the morphological transformation of galaxies from late-types (spiral and irregular) to early-types (elliptical and lenticular). This involves studying various properties, corresponding timescales, the role of AGNs, mergers and interactions, and the environment of early- and late-type galaxies.

This thesis focuses on two main objectives:

(i) Understanding the properties of galaxies with a faster inside-out assembly and their possible role in the morphological transformation of galaxies. We used spectroscopic and photometric data from the Sloan Digital Sky Survey (SDSS) Data Release 8 (DR8) and selected galaxies with suggested stellar masses: $\log M*/M_\odot = 10.73 - 11.03$ at $z < 0.1$. We studied some of the most important properties of galaxies, such as SFRs, sSFRs, spectral properties, morphologies, and nuclear activity.

(ii) To survey LBGs in the vicinity of three Hot DOGs to better characterize the richness and evolutionary state of their environment. In the second part of this work, we focus on one Hot DOG as a pilot study, where we modified two photometric selection criteria and selected LBGs around W2246-0526. Then, we compared the number density in a blank field. For the second part of this work, we extended our study by adding more Hot DOGs, optimizing the selection function using the COSMOS field with HSC filters for all three Hot DOGs, and comparing the number density in each field.

This thesis is organized as follows: Chapter 1 introduces the main scientific topic related to this work, summarizes the previous studies, and explains our motivation.

In Chapter 2 , we present our study of a sample of 48,127 galaxies selected from the SDSS MPA-JHU catalogue with $\log M*/M_\odot = 10.73 - 11.03$ and $z < 0.1$. We examined the morphological properties of our galaxies using Galaxy Zoo classifications and their spectroscopic properties based on their BPT diagram classifications. We found that the majority of Inside-Out Assembled Galaxy (IOAG) candidates are classified as AGNs (40%) and composites (40%), suggesting that 80 percent of IOAG candidates are not purely star-forming galaxies. Most BPT-classified star-forming IOAG candidates exhibit spiral morphologies and fall within the main sequence, while Seyfert 2 and composites predominantly display spiral morphologies but exhibit quiescent star formation rates (SFRs). Those classified as AGN consistently show lower SFRs than star-forming galaxies, suggesting AGN activity may be related to this quenching. This study has been published as Zewdie et al. (2020).

In Chapter 3 , we present our study of the environment of the most luminous known Hot DOG, W2246–0526, at $z = 4.601$ using deep GMOS-S imaging in r, i, and z bands. We found an overdensity of LBGs around W224-0526, 6 times greater than in a blank field, leading to the conclusion that W224-0526 live in a dense region at a time when the Universe was 1.3 Gyr old. This study has been published as Zewdie et al. (2023).

In Chapter 4 , we report the reanalysis of W2246-0526 using our optimized selection function and extend it to two more Hot DOGs

environments. It explains in detail how we defined the optimized selection function and estimated the overdensity, considering the possible contamination around three Hot DOGs. It also describes the spatial distribution of the selected LBGs around them and other technical aspects of the entire analysis. The main findings of this work will be reported in Zewdie et al., (2023b, in prep.).

Finally, in Chapter 5 , we summarize the main findings of this thesis and discuss important conclusions and outlook of this work.

# Chapter 2

# AGN and star formation properties of inside-out assembled galaxy candidates $z < 0.1$

We study a sample of 48127 galaxies selected from the SDSS MPA-JHU catalog, with $\log M_\star/M_\odot = 10.73 - 11.03$ and $z < 0.1$. Local galaxies in this stellar mass range have been shown to have systematically shorter assembly times within their inner regions ($< 0.5\ R_{50}$) when compared to that of the galaxy as a whole, contrary to lower or higher mass galaxies which show consistent assembly times at all radii. Hence, we refer to these galaxies as Inside-Out Assembled Galaxy (IOAG) candidates. We find that the majority of IOAG candidates with well-detected emission lines are classified as either AGN (40%) or composite (40%) in the BPT diagram. We also find that the majority of our sources are located below the main sequence of star formation and within the green valley or red sequence. Most BPT-classified star-forming IOAG candidates have spiral morphologies and are in the main sequence, whereas Seyfert 2 and composites

have mostly spiral morphologies but quiescent star formation rates (SFRs). We argue that a high fraction of IOAG candidates seem to be in the process of quenching, moving from the blue cloud to the red sequence. Those classified as AGN have systematically lower SFRs than star-forming galaxies suggesting that AGN activity may be related to this quenching. However, the spiral morphology of these galaxies remains in place, suggesting that the central star formation is suppressed before the morphological transformation occurs.

## 2.1 Introduction

How galaxies form and evolve through cosmic time is one of the major open questions in extragalactic astronomy and modern cosmology. In particular, we need to understand what role do galaxy mergers, AGN activity, and star-formation feedback play in driving the observed morphological evolution and the quenching of star formation in massive galaxies.

Over the last few decades, a number of important empirical correlations of galaxy parameters have been discovered. This includes the color-stellar mass relation, in which galaxies show a bi-modal distribution (e.g., Pović et al. 2013; Schawinski et al. 2014; Mahoro et al. 2017, Nogueira-Cavalcante et al. 2018). On one hand, late-type galaxies populate a region called the blue cloud, found at, as the name says, blue UV/optical colors and stellar masses typically below $\log M_\star = 11 \, M_\odot$. On the other hand, early-type galaxies form a tight relation between their red UV/optical colors and their stellar masses, usually called the red sequence. Between the blue cloud and red sequence there is an under-occupied space known as the "green

valley", which includes a mixed population of galaxies (e.g., Brinchmann et al. 2004; Whitaker et al. 2012; Guo et al. 2013; Schawinski et al. 2014; Salim et al. 2015; Mahoro et al. 2017, 2019), most notably, post-starbursts galaxies have strong Balmer absorption lines and the lack of emission lines (E+A galaxies, e.g., Dressler and Gunn 1983; Zabludoff et al. 1996; Matsubayashi et al. 2011). This bi-modality has been observed at both low and higher redshifts, up to at least $z \sim 2$ (e.g., Ilbert et al. 2010; Schawinski et al. 2014; Mahoro et al. 2017).

A tight relation between the star formation rates and stellar masses of typical star-forming galaxies has also been identified (e.g., Brinchmann et al. 2004; Noeske et al. 2007, Elbaz et al. 2007, Daddi et al. 2007; Karim et al. 2011; Whitaker et al. 2012, 2014; Schreiber et al. 2015; Leslie et al. 2016; Pović et al. 2016), usually referred to as the "main-sequence" (MS) of star-forming galaxies. Galaxies above this sequence (i.e., with higher SFRs for their stellar mass) are typically called starbursts and those below (i.e., with lower SFRs for their stellar mass) are usually called passive or quiescent galaxies (e.g., Gonçalves et al. 2012; Moustakas et al. 2013; Leslie et al. 2016). Galaxies that have halted their star-formation activity are usually called quenched galaxies. These galaxies can be broadly associated with those falling within the range of "red passive galaxies" or galaxies lying below the MS of star formation ($< 0.3$ dex MS). These relations suggest that the stellar mass is a fundamental parameter in the evolution of galaxies and that galaxies with different stellar masses may have very different formation and evolution histories. The evolution of the so-called galaxy size - mass relation has been taken as evidence for inside-out growth (e.g., van der Wel et al. 2014; Mowla et al. 2019): at a fixed stellar mass, galaxies at high redshift seem

to have been more compact than in the local universe. In addition, recent observations based on integral field spectroscopy and using the fossil record method (e.g., Pérez et al. 2013; Pan et al. 2015; Ibarra-Medel et al. 2016; García-Benito et al. 2017; Liu et al. 2018; Sánchez et al. 2018; Wang et al. 2018), have helped to characterize the mass assembly modes and star formation histories of galaxies as a function of radius. Evidence for segregated growth between the central and outer regions of massive galaxies (both on and off the main sequence) has been found at high redshift (e.g., Ibarra-Medel et al. 2016; Morselli et al. 2016; Nelson et al. 2016; Belfiore et al. 2018; Tacchella et al. 2018) and as well as in simulations (e.g., Aumer et al. 2014; Avila-Reese et al. 2018). Pérez et al. (2013) used the integral field spectroscopic data from the Calar-Alto Legacy Integral Field Area (CALIFA) survey to study the growth rates of a sample of 105 galaxies in a range of stellar masses ($\log M_\star = 9.58 - 11.26$ $M_\odot$) within different regions of the galaxies (nucleus, inner $0.5R_{50}$ and $R_{50}$[1], and outer region $> R_{50}$). Pérez et al. (2013) found that in the stellar mass range, $\log M_\star = 10.73 - 11.03$ $M_\odot$ the inner regions of galaxies reached 80% of their final stellar mass twice as fast as in the outskirts. They suggested different mechanisms to explain this growth, through the accretion of halo or intergalactic gas clouds, or through interactions and mergers with smaller or similar mass galaxies (see Pérez et al. 2013). The authors suggested that perhaps more massive galaxies, that show inside-out growth, grow through minor and major mergers while in lower mass galaxies, where outside-in growth was observed, secular evolution could be the dominant mechanism. For the rest of this study, we will refer to the galaxies in this

---

[1] $R_{50}$ is the circular half-light radius in $5635 \pm 40$ Å (Pérez et al., 2013).

stellar mass range as "Inside-Out Assembled Galaxy" (IOAG) candidates. In this work, we suggest that these galaxies could play an important role in understanding their morphological transformation from late- to early-types.

Other studies suggest similar mass ranges of $\log M_\star = 10.6 - 10.7$ M$_\odot$ to be important in galaxy evolution, e.g., in the stellar-to-halo mass relation and accumulated stellar growth (e.g., Mandelbaum et al. 2006; Conroy and Wechsler 2009; Moster et al. 2010; Behroozi et al. 2010; Guo et al. 2010; More et al. 2011; Leauthaud et al. 2012), in simulations when studying the shape of stellar-to-halo mass relation and supernova (SN) and AGN feedback mechanisms (Shankar et al., 2006), or when analyzing low-ionization nuclear emission-line regions (LINERs) with high SFRs (Pović et al., 2016).

In this work, we aim to characterize the physical properties of IOAG candidates and to understand better the nature of inside-out growth and its relation with AGN activity. This work is organized as follows: In Section 2.2, we present the data, catalogs, and samples used throughout this work. In Section 2.3, we analyze the spectral classification of galaxies using optical emission lines, their morphological classification, SFR distributions, and their location in the SFR-stellar mass diagram as well as in the color-stellar mass diagram. Our main results are discussed in Section 2.4, while our summary and conclusions are described in Section 2.5. Throughout this work, we assume a standard $\Lambda$ CDM cosmology with $H_0 = 70$ km s$^{-1}$ pc$^{-1}$, $\Omega_\Lambda = 0.7$ and $\Omega_{\mathrm{M}} = 0.3$, and we present all magnitudes in the AB system and the WISE Vega-system magnitudes.

## 2.2   Data and sample selection

### 2.2.1   SDSS

In this work, we use data from the Sloan Digital Sky Survey (SDSS), Data Release (DR8; Aihara et al. 2011). The SDSS DR8 includes imaging in the *'u'*, *'g'*, *'r'*, *'i'* and *'z'* photometric bands of 14,555 deg$^2$ throughout the sky, with roughly 5200 deg$^2$ in the southern Galactic cap and the rest in the northern hemisphere (York et al. 2000; Aihara et al. 2011).

We use SDSS DR8 instead of a more recent Data Release due to the availability of estimates for a number of physical parameters through the MPA-JHU catalogue[2]. Specifically, we use the emission line intensities, stellar masses, and SFRs provided through this catalog. Stellar masses were calculated by Kauffmann et al. (2003) from the SDSS broad-band photometry and using a Bayesian Spectral Energy Distribution (SED) fitting methodology. We chose the stellar mass estimate corresponding to the median of the SED fit probability distribution function. The SFRs are calculated using a number of emission lines and the methods developed by Brinchmann et al. (2004). For AGNs and galaxies with weak emission lines, the SFRs are computed using the correlation with Dn 4000 index (Kauffmann et al. 2003; Brinchmann et al. 2004) obtained through fiber aperture measurements and corrections based on broadband photometry (Salim et al., 2007).

Pérez et al. (2013) results show the direct relation of relative assembly rate with stellar mass and suggest the highest differences in the proposed stellar-mass range of $\log M* = 10.73 - 11.03\ M_\odot$, where

---

[2]http://www.sdss3.org/dr8/spectro/galspec.php
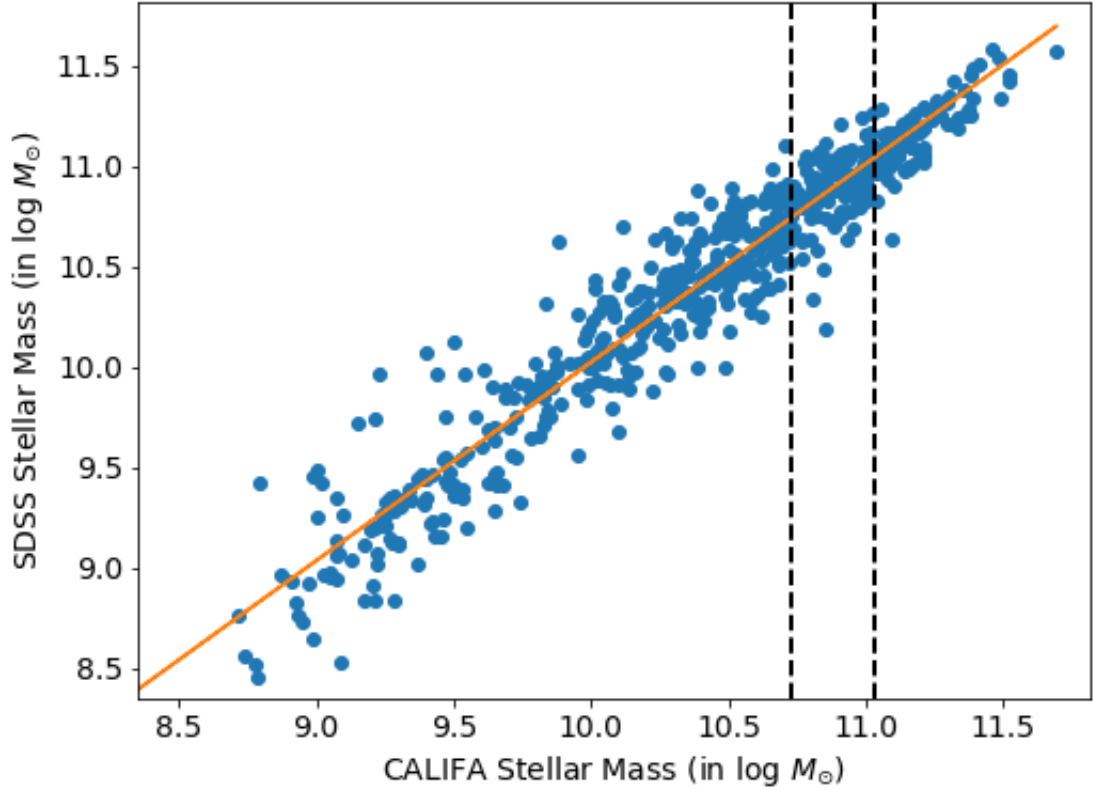
FIGURE 2.1: Comparison between the stellar masses measured in the CALIFA survey (Pérez et al., 2013) and the SDSS MPA-JHU estimates (Brinchmann et al., 2004) for a sample of 106 overlapping sources. The red solid line shows the 1-to-1 relation and the vertical dashed (black) lines the mass range of this study, based on the work of Pérez et al. (2013). Given the low scatter between these estimates and the absence of obvious systematic offsets, the galaxy stellar masses used in our work can thus be validated.

the growth of the inner part of the galaxy is twice as fast as that of the outer region. We noticed that a narrower stellar mass range of $\log \log M* = 10.73 - 10.93$ $M_\odot$ with the relative assembly rate of $\sim 2.37$ could also work, however, our selection of a bit larger stellar mass range was motivated by having a significantly larger sample of galaxies to perform all statistical analysis. We tested all statistics for the smaller-mass range as well, without finding any significant differences (not larger than 5-6%), confirming that our results will remain consistent with the final selected range of stellar mass.

As mentioned earlier, this research is motivated by the results obtained by Pérez et al. (2013). To select IOAG candidates, we thus selected sources with stellar masses in the range $10.73 - 11.03$ $M_\odot$. The stellar mass range defined by Pérez et al. (2013) was based on CALIFA data and used a different methodology than those used in the SDSS MPA-JHU stellar mass estimates. To check for possible biases in the stellar mass selection, we compare in Figure 2.1 the Pérez et al. (2013) stellar mass estimates with the MPA-JHU estimates for a sample of galaxies in the CALIFA survey. Both estimates are found to be in good agreement, with a scatter of $\sim 0.1$ dex, thus validating the SDSS stellar mass measurements for this study and the selected mass range for the IOAG candidates.

The photometric and spectroscopic SDSS galaxy catalogs were cross-matched using a radius of $2''$ as the best compromise between the number of lost matches and possible miss-matched sources. We further restrict the sample to the IOAG candidates' stellar mass range $10.73 - 11.03$ $M_\odot$ and to $z < 0.1$ leading to a final sample of 48127 galaxies. The upper limit in redshift was selected following Kewley et al. (2006) to avoid completeness issues with the spectroscopic classification. The selected redshift range is also the proper one for our study when dealing with morphology (see Section 2.2.4), knowing that the classification becomes challenging at higher redshifts, especially for imaging data from a shallow survey as SDSS (Pović et al., 2015).

### 2.2.2 Spectral classification

We classified galaxies spectroscopically using the "Baldwin, Phillips & Terlevich" (BPT) diagram (Baldwin et al., 1981). This classification is based on nebular emission-line ratios that are used to differentiate their ionizing source. To provide a clean BPT spectral classification and following previous studies, we applied a further restriction to our catalog, by requiring that the signal-to-noise ratio (S/N) is above 3.0 for each of the emission lines used (e.g., Kewley et al. 2006, 2001; Kauffmann et al. 2004; Brinchmann et al. 2004). This results in samples of 24561, 18478, 11006 galaxies, respectively, for the [OIII]/H$\beta$ versus [NII]/H$\alpha$ (BPT-NII), [OIII]/H$\beta$ versus [SII]/H$\alpha$ (BPT-SII), and [OIII]/H$\beta$ versus [OI]/H$\alpha$ (BPT-OI) diagrams. Based on these line ratios, sources are classified as either star-forming, AGN (Seyfert 2 or LINER) or composite. Given the significantly larger number of sources in the BPT-NII diagram, we decided to focus on this classification for the rest of this study.

As the BPT classification is based on narrow-line ratios, we removed the Type 1 AGNs (QSO) from the sample using the spectroscopic classification from the SDSS DR8. We also removed galaxies without SFR estimation available in the MPA-JHU catalog, yielding a total number of 23816 galaxies contained in the BPT-NII diagram. We do not add the type 1 AGN back to our sample even though their AGN nature is secure because the accretion disk emission may bias their stellar mass estimates.

Figure 2.2 shows the BPT-NII diagram for our galaxy sample. Galaxies found below the dashed line (Kauffmann et al., 2003) are star-forming, between dashed and solid line (Kewley et al., 2006, 2001) are composite, and above the solid line are AGN. Using results of
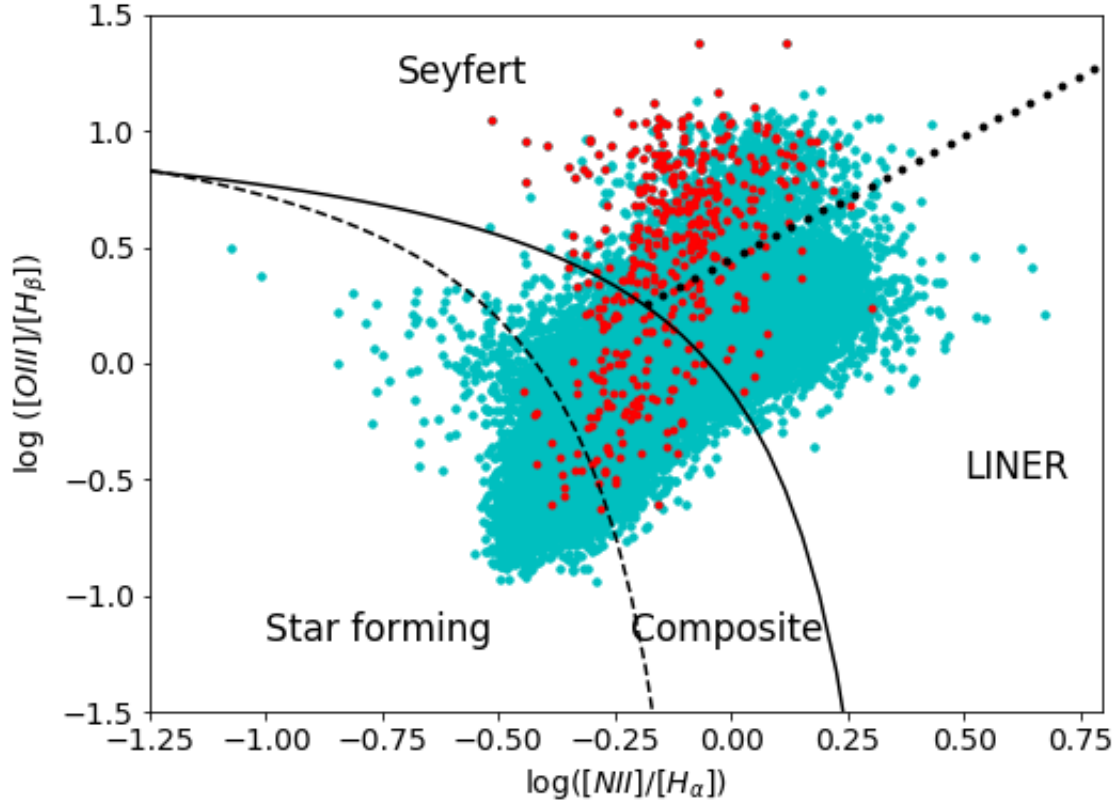
FIGURE 2.2: The $[OIII]/H_\beta$ versus $[NII]/H_\alpha$ BPT diagnostic diagram for the SDSS galaxies in our sample. The sample has been restricted to galaxies with line emission detected at the S/N $\geq$ 3 level. The dashed line shows the (Kauffmann et al., 2003) empirical division between star-forming and starburst/AGNs composite galaxies. The solid line represents the (Kewley et al., 2006) division between star-forming galaxies and those with dominant AGNs contribution (extreme starburst limit). The dotted line shows the separation between Seyfert 2 and LINER (Schawinski et al., 2007). The cyan symbols represent the location of the selected SDSS galaxies in the stellar mass range occupied by inside-out assembled galaxies. The red symbols represent those galaxies that are WISE-selected AGN. As expected, the locus of WISE AGNs coincides with the Seyfert 2 AGNs optical classification.

(Schawinski et al., 2007), AGN is further separated between Seyfert 2 (above the dotted line) and LINERs (below). Table 2.1 shows the number of galaxies in each classification. We find that the majority (80%) of the galaxies in our sample show signatures of AGN activity (Composite, Seyfert 2, or LINER).

TABLE 2.1: The statistical distribution of galaxies ($\log M_\star = 10.73 - 11.03$ M$_\odot$) based on morphological and spectroscopic classification

| Sample | | Number of sources | SFR-stellar mass | | | Colour-stellar mass | | |
|---|---|---|---|---|---|---|---|---|
| | | | MS | Starburst | Quiescent | Blue cloud | Green valley | RS |
| Galaxy Zoo | All | 44092 | 12% | 1% | 87% | 14% | 19% | 67% |
| | Elliptical | 5322 | 1% | 0% | 99% | 2% | 10% | 88% |
| | Spiral | 16338 | 22% | 1% | 77% | 26% | 28% | 46% |
| | Uncertain | 22432 | 7% | 1% | 92% | 8% | 14% | 78% |
| BPT-NII | All | 23816 | 21% | 3% | 76% | 24% | 27% | 49% |
| | star-forming | 4733 | 61% | 11% | 28% | 61% | 26% | 13% |
| | Composite | 9458 | 17% | 0% | 83% | 22% | 33% | 45% |
| | LINER | 7893 | 2% | 0% | 98% | 4% | 20% | 76% |
| | Seyfert 2 | 1732 | 18% | 0% | 82% | 25% | 33% | 42% |

### 2.2.3 WISE AGN

NASA's Wide-field Infrared Survey Explorer (WISE; Wright et al. 2010) satellite mapped the whole sky in four mid-infrared (MIR) bands centered at $3.4\mu m$ (W1), $4.6\mu m$ (W2), $12\mu m$ (W3) and $22\mu m$ (W4). We used the AllWISE Data Release[3] to check the existence of IR obscured AGN activity in our sources, and validate our optical AGN spectroscopic classification (see Section 2.2.2). We carried out
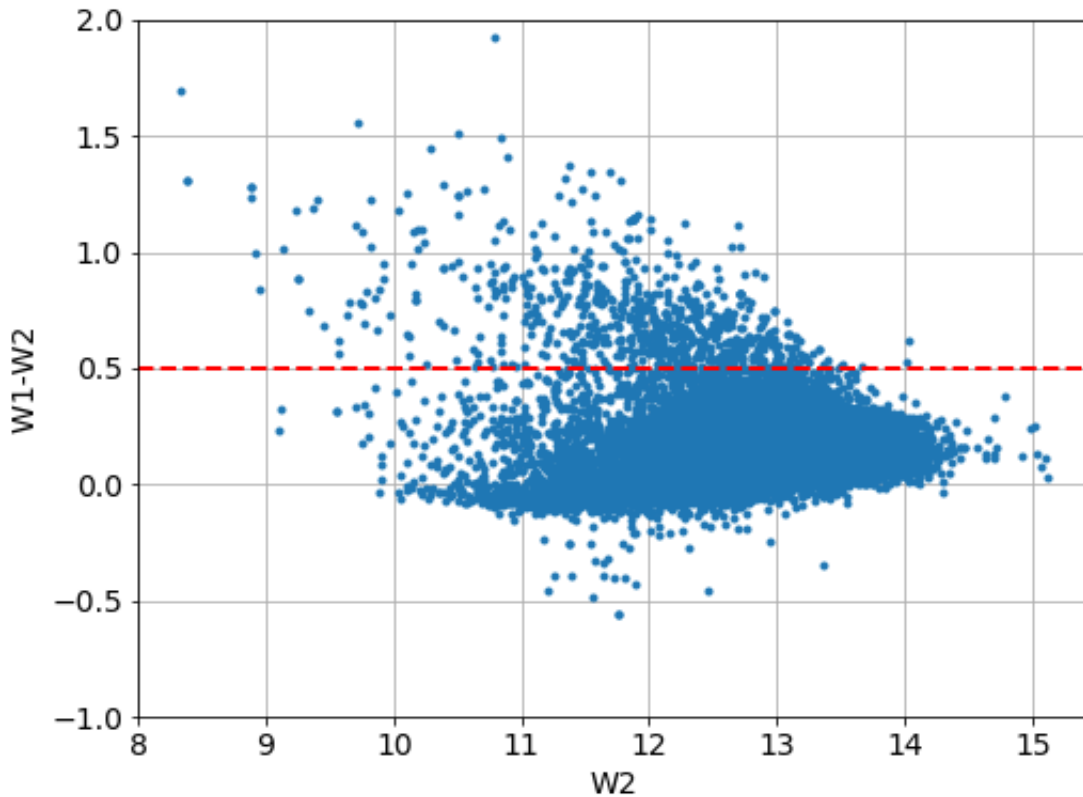


FIGURE 2.3: (W1-W2) versus W2 color-magnitude diagram for the mass-selected SDSS sources with an IR counterpart in the WISE catalog. The adopted color cut to select AGN sources is shown by the red solid line (Assef et al., 2018).

the spectroscopic classification of galaxies, using the BPT diagram, as described in Section 2.2.2. We then cross-correlated the 24561 galaxies with enough $S/N > 3$ in their emission lines to be classified

---

[3]http://wise2.ipac.caltech.edu/docs/release/allwise/

in the BPT-NII diagram (See Section 2.2.2 for details) with the WISE source catalog, by searching for positional matches within $2''$. We find that 24383 sources (99.3%) have a WISE IR counterpart. Figure 2.3 shows the (W1-W2) versus W2 color-magnitude diagram for the selected sources. We classified sources with W1-W2 > 0.5 as AGN following Figure 1 of Assef et al. (2013) and considering the bright W2 magnitudes of our objects. We find that out of the 24383 sources with WISE and SDSS matches, 740 are classified as AGNs using this simple color selection, 316 of which are spectroscopically classified as Type 1 AGN (QSO). While more strict color cuts at $(W1-W2) = 0.6$ or 0.7 can provide cleaner AGN samples, the selected cut provides a sample with $\sim 90\%$ reliability according to Assef et al. (2018).

When applying the BPT classification to the sample of sources identified as AGN through their WISE IR colors, we find that most of them (63%) are indeed classified as Seyfert 2 and composite (25%), with a smaller fraction classified as LINER (9%) and star-forming (3%) objects. We also find that WISE-selected AGN has significantly larger median SFRs compared to the optically selected AGN. For the WISE-selected AGN, we find a median log $\mathrm{SFR}/[\mathrm{M_\odot yr^{-1}}]$ of 0.35 (consistent with the results of Ellison et al. 2016), while for Seyfert 2 galaxies and LINERs we find -0.24 and -1.14, respectively.

### 2.2.4 Morphological Classification

We use the visual morphological classification of galaxies from the Galaxy Zoo[4] citizen science project (Lintott et al., 2008, 2011). This catalog provides a morphological classification for all galaxies in the SDSS DR7 spectroscopic sample and is based on a vote fraction

---

[4]https://data.galaxyzoo.org/

threshold of 0.8. Galaxies with lower vote thresholds are typically more difficult to classify visually as they tend to have low brightness, low stellar masses, and/or due to the presence of nearby objects (including foreground and background sources) (Lintott et al. 2011; Bamford et al. 2009). After cross-matching our sample with the Galaxy Zoo catalog, we find 44092 IOAG candidates (out of 48127 sources), where 12% are classified as ellipticals, 37% as spirals, and 51% are uncertain. All statistics are shown in Table 2.1.

## 2.3 Analysis and Results

### 2.3.1 Comparison of morphological and spectroscopic classifications

Figure 2.4 shows the distribution of SFR of different spectroscopic and morphological types. As can be seen, galaxies classified as LIN-ERs appear to have low SFRs, and objects spectroscopically classified as star-forming galaxies show high SFRs, as expected. Objects classified as Seyfert 2 or composite galaxies have similar bi-modal distributions to those objects morphologically classified as spirals, with a peak at $\log(\text{SFR}) \sim 0$, and a second one at $\log(\text{SFR}) \sim -1.5$. Note that the distribution of SFRs for the star-forming galaxies extends to higher values compared to that of composite and Seyfert 2.

The right panel of Figure 2.4 also shows that most objects classified as ellipticals are located in the low SFR regime, as expected. The distribution is relatively narrow and peaks at $\log \text{SFR}(\text{M}_\odot \text{yr}^{-1}) \sim -1.6$. Similar SFR values are found for the galaxies with 'uncertain' classification. This likely implies that these objects are either faint ellipticals or S0 galaxies with almost negligible star formation activity.
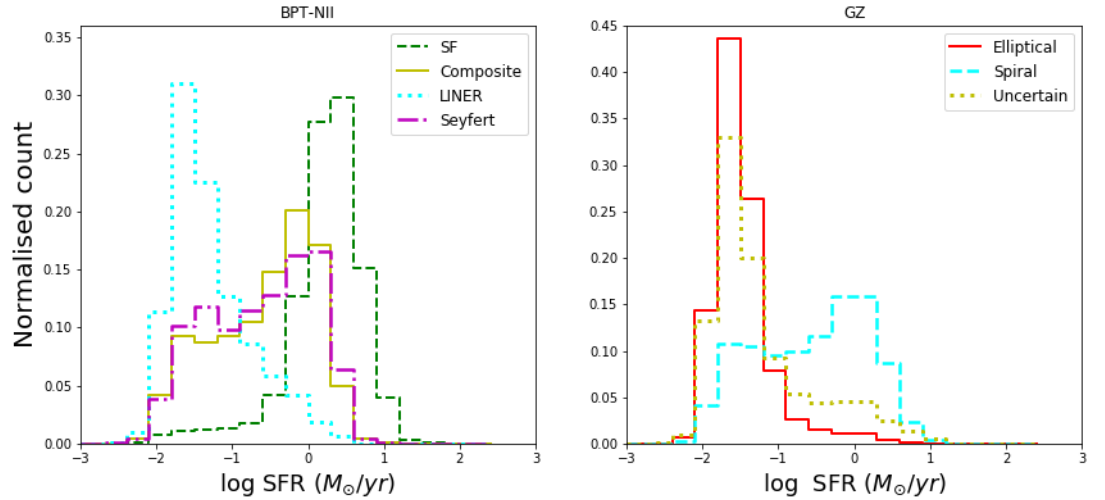
FIGURE 2.4: Distribution of SFR based on the BPT-NII emission-line classification (left-side). The spectroscopic classified galaxies correspond to SF (green dot lines), composite (yellow dot-dashed lines), LINER (cyan dashed lines), and Seyfert 2 (violet solid line). Distribution of SFR based on the Galaxy Zoo classification (right panel). Elliptical, spiral, and uncertain classes are marked with red (solid lines), cyam (dashed lines), and yellow (dot lines), respectively.

Spiral galaxies are instead found to have a bi-modal distribution, with the bulk of the sources showing relatively high SFRs, namely $\log(\text{SFR}) \gtrsim 0$, and the second group of sources with low SFRs peaking at $\log(\text{SFR}) \sim -1.5$, similar to elliptical and uncertain galaxies, and with no gap between peaks.

With respect to the spectroscopic classification, we find that 64% (2802) of the star-forming galaxies are classified as spirals and only 3% (115) as ellipticals. The remaining 33% (1443) are classified as 'uncertain' by Galaxy Zoo. In the case of the composite class, we find that 56% (4939) are spirals and 8% (668) ellipticals, whereas, for LINERs, we find that 35% (2573) of them are classified as spirals and 14% (1058) as ellipticals. Finally, we find that for Seyfert 2 galaxies, 53% (857) are spirals and 5% (81) are ellipticals. In the case of LINERs, the lower number of spirals compared to the other spectroscopic classes tends to agree with previous studies that find

that they are mainly hosted by early-type galaxies (Ho, 2008, and references therein).

### 2.3.2 Relation to the star-forming main sequence
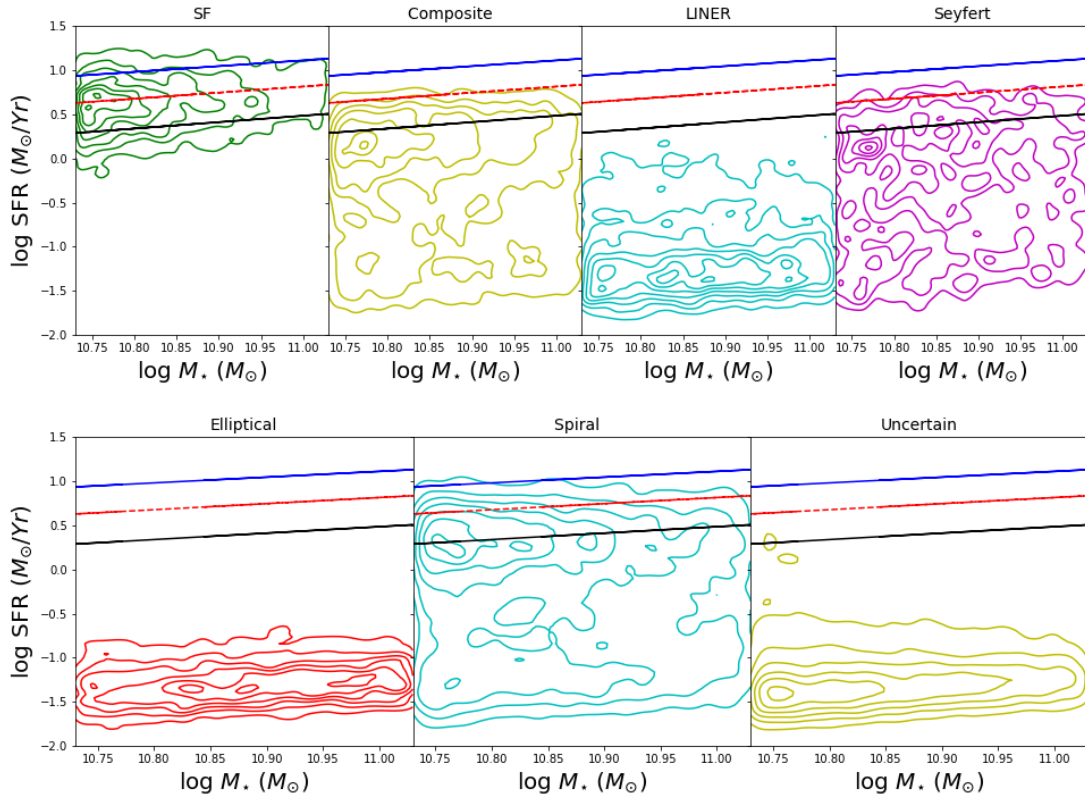


FIGURE 2.5: SFR as a function of stellar mass for the IOAG candidates in each spectral class (top panels) and for the morphological classification (bottom panels). A red dashed line in each panel represents the local main sequence of star formation from Whitaker et al. (2012). The blue and black solid lines indicate the typical scatter around the MS of 0.3 dex.

Figure 2.5 shows the SFR versus stellar mass diagram for the sample of IOAG candidates separated both by spectroscopic and morphological class, compared to the main sequence of star formation at $z = 0$ (Whitaker et al., 2014). Since, by construction, our sample covers a relatively small stellar mass range, these diagrams show similar distributions as those shown in Figure 2.4. The main sequence (MS) in this short stellar mass range appears relatively flat, and galaxies with $\log(\text{SFR}) \lesssim 0.4$ will be located below the lower

boundary of the MS. For the width of MS, we used $\pm$ 0.3 dex (black and blue color lines in all Figures below), found in different works to be the proper $1\sigma$ boundaries (Pović et al., 2016, and references therein). Galaxies spectroscopically classified as star-forming are typically consistent with the MS (61%), with only 11% (28%) being located above (below) the MS. Galaxies spectroscopically classified as composite, LINER, or Seyfert 2 have lower SFRs, with only 17%, 2%, and 18%, respectively, being within the bounds of the MS and all the rest below. For the morphological classification, we found that all the ellipticals lie well below the MS, whereas the spiral class shows a bi-modality (already seen in the SFR histograms) with most of them located on the MS and the second cluster of sources well below the MS. Spirals below the MS are likely due to a combination of dust reddening and misclassified S0 galaxies. Yet it is possible that some objects are indeed spiral galaxies effectively in the process of quenching their star-formation (e.g., Masters et al. 2010; Hao et al. 2019; Mahajan et al. 2020).

To visualize more clearly the number of sources of each class above, in, or below the MS, we compute the specific SFR (sSFR = SFR/$M_*$), normalized by the sSFR of the MS at $z = 0$ at a given stellar mass. This normalized sSFR ($\delta_{\mathrm{MS}}$ = sSFR/sSFR$_{\mathrm{MS}}(M_*)$) represents the distance of a given galaxy (with stellar mass $M_*$ and redshift $z$) to the MS, and thus values $\log(\delta_{\mathrm{MS}}) > 0.3$ or $< 0.3$ will be associated to starbursts or quiescent galaxies, respectively.

We found that from the spectroscopic (morphological) samples of IOAG candidates considered, 76% (87%) and 21% (12%) are located below and on the MS, respectively, with only 3% (1%) of the sources being in the starburst regime.
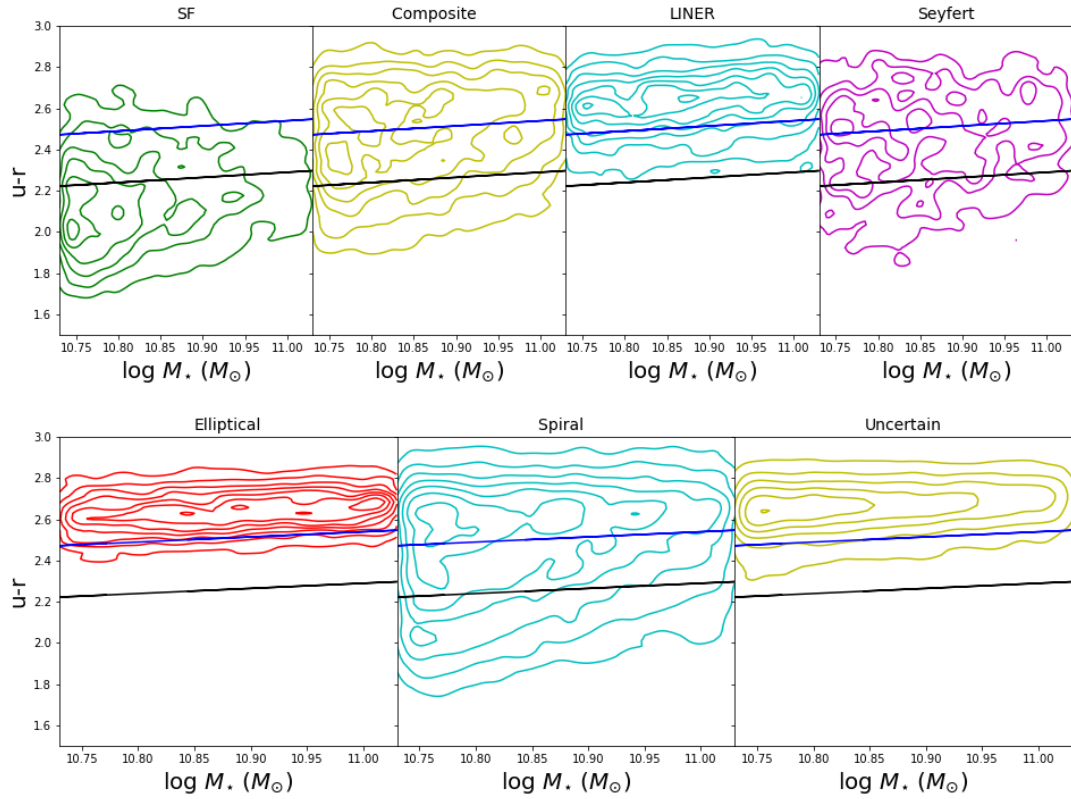
FIGURE 2.6: Distribution of IOAG candidates in the rest-frame $u - r$ dust-corrected color-mass diagram for the spectroscopic (top) and morphological (bottom) classes. The area between the blue and black lines delineates the region occupied by galaxies in the green valley, according to the prescriptions from Schawinski et al. (2014). Red sequence and blue cloud galaxies are located above and below the blue and black solid lines, respectively.

### 2.3.3 Color - stellar mass diagram

In this section, we study the distribution of the rest-frame $u - r$ color associated with the spectroscopic and morphological classification of the IOAG candidates. We follow Schawinski et al. (2014) work and correct the observed optical fluxes for dust reddening using the OSSY Database catalogue[5] and the Cardelli et al. (1989) extinction law.

Figure 2.6 shows the rest-frame dust-corrected color-stellar mass diagram for the IOAG candidates split by BPT spectroscopic (top panels) and morphological (bottom panel) class. The solid lines illustrate the location of the "green valley", from Schawinski et al.

---

[5]http://gem.yonsei.ac.kr/ ksoh/wordpress/

(2014), in the selected stellar mass range using extinction corrected colors (see their Fig. 3). Galaxies located between, below, and above these lines are considered to be in the "green valley", "blue cloud" and "red-sequence", respectively.

For star-forming galaxies, we find that 61%, 26%, and 13% of sources are located in the blue cloud, green valley, and red sequence, respectively. Composite galaxies are found to be mostly in the red sequence (45%), with a significant population located in the green valley (34%). Similarly, 76% and 20% of LINERs are located in the red sequence and green valley, respectively, whereas Seyfert 2 galaxies are found to be relatively uniformly distributed with 42%, 33%, and 25% in the red-sequence, green valley, and blue cloud, respectively.

For the morphological classification, we found that elliptical galaxies are mostly (88%) located in the red sequence, as expected, and in the green valley (10%). For spiral galaxies, 46% and 28% are located in the red sequence and green valley respectively. Finally, the uncertain galaxies are mainly located in the red sequence (78%) and the green valley (14%).

### 2.3.4   WISE color-color diagram

The WISE color-color diagram classifies astronomical objects according to their W1-W2 and W2-W3 colors (see Wright et al. 2010). Alatalo et al. (2014) noticed a significant bi-modality in the W2-W3 color of galaxies that effectively separates early- and late-type objects. They refer to the color gap between these populations as the Infrared Transition Zone (IRTZ). Remarkably, galaxies within the

IRTZ are not necessarily within the optical green valley, since optically selected green valley objects tend to fall closer to star-forming galaxies in the WISE color-color diagram (Alatalo et al., 2014). Figure 2.7 shows the WISE color-color distribution of our sources. We find that 96% of the star-forming galaxies are located in the red region (i.e., redwards of the IRTZ), and the remaining 4% are within the IRTZ. We also find that 68% of composite galaxies lie in the red region, 28% within the IRTZ, and 4% in the blue region (i.e., bluewards of the IRTZ). Regarding LINERs, 73% fall within the IRTZ, 20% in the red region, and 7% in the blue region. Similarly, we find that 70% of Seyfert 2 galaxies are located in the red region and 28% in the IRTZ. In terms of the morphological classification, we find that 64% and 33% of the elliptical galaxies are located in the IRTZ and in the blue region, respectively, and 66% and 32% of the spiral galaxies are located in the red region and in the IRTZ, respectively. We also find that 69% and 21% of the uncertain classified galaxies are located in the IRTZ and in the red region, respectively.

### 2.3.5 Dn4000 distribution

Previous studies have shown a clear connection between the star formation history of galaxies and the stellar absorption line indices, such as Dn4000 break and $H_\delta$ (Kauffmann et al., 2003). These two indices have been used as indicators of the age of the stellar populations in galaxies. In addition, Dn4000 has been used as an indicator of SFR (Brinchmann et al. 2004; Salim et al. 2007). In this section, we study the distribution of the Dn4000 index. Figure 2.8 shows the distribution of Dn4000 in our sample in relation to both, spectroscopic (left) and morphological (right) classifications. Distributions are consistent with results obtained in Figure 2.4, as expected,
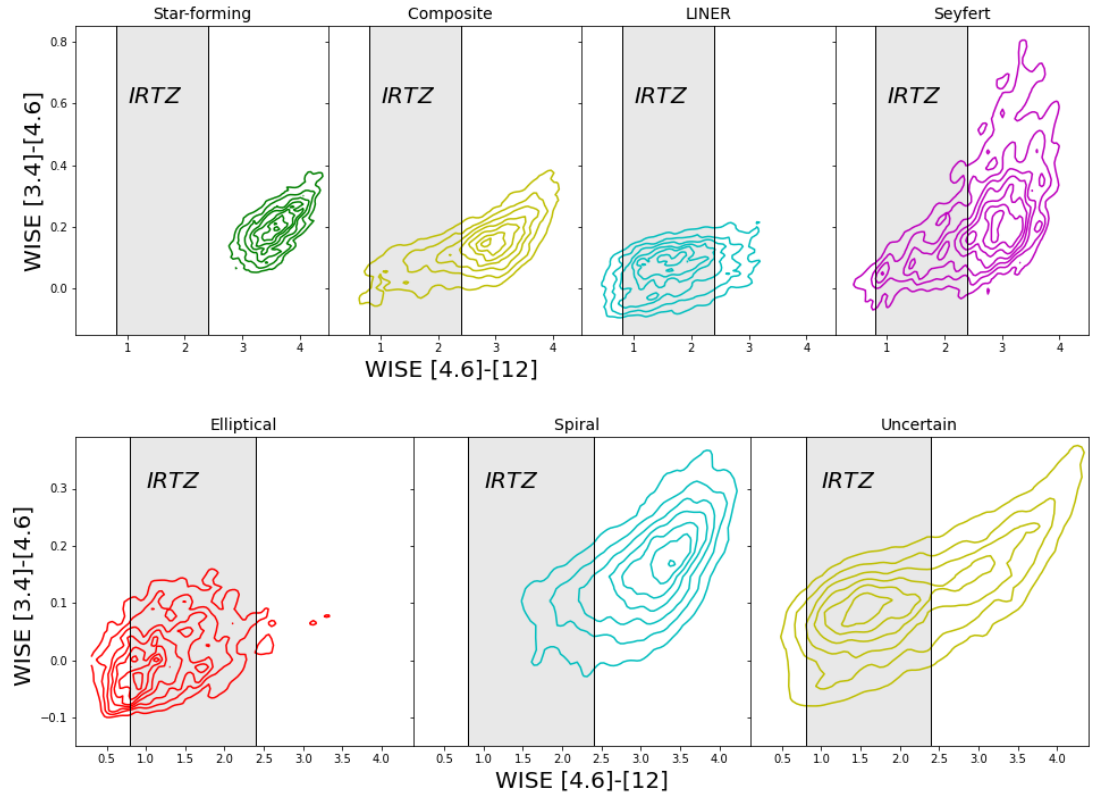
FIGURE 2.7: The WISE color-color ($[4.6]-[12]$ vs. $[3.4]-[4.6]$) diagram of spectroscopic (top) and morphological (bottom) classes. The WISE W2-W3 color in the range 0.8 - 2.4 is described as an infrared transition zone (IRTZ, Alatalo et al. 2014).

since the MPA-JHU SFRs have been measured using the Dn4000 index (Brinchmann et al. 2004). Li et al. (2015) used Dn4000 to differentiate between galaxies that are centrally star-forming (with Dn4000 < 1.6) or centrally quiescent (with Dn4000 > 1.6). We find more galaxies to be centrally quiescent in both the spectroscopic (62%) and morphological (72%) samples. According to this criterion, star-forming galaxies are more likely to be classified as centrally star-forming (87%), while composites (61%), Seyfert 2 (58%), and LINERs (95%) are more commonly classified as centrally quiescent. Ellipticals (97%), spirals (62%), and uncertain (86%) galaxies in our sample are all found to have predominantly centrally quiescent star-formation activity.
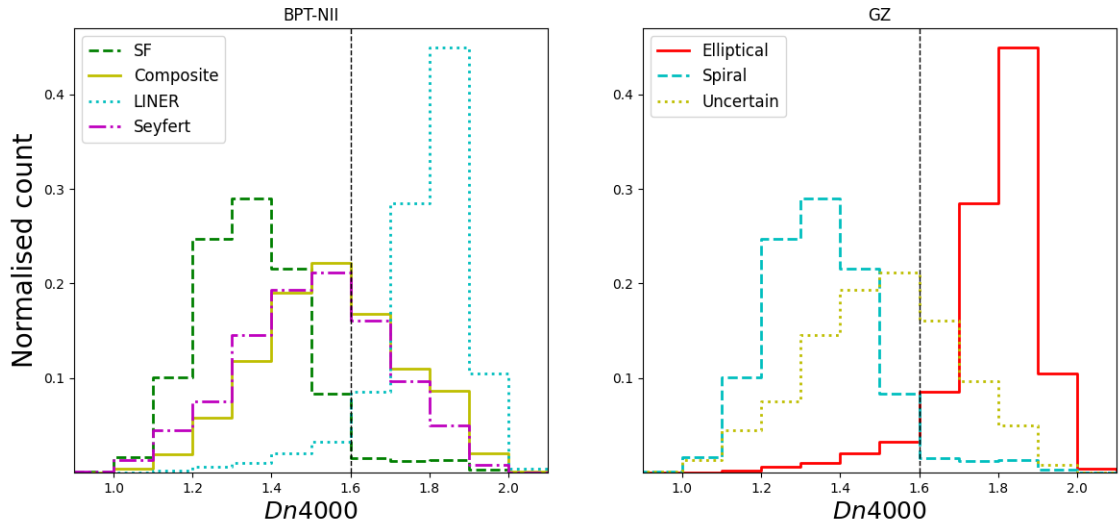
FIGURE 2.8: Distribution of Dn4000 index for the spectroscopic (left) and morphological (right) classes. The black vertical dashed line shows results of Li et al. (2015) for separating those galaxies that are centrally star-forming (Dn4000 < 1.6) are centrally quiescent (Dn4000 > 1.6).

### 2.3.6 UV colour distribution

We use the GALEX GR6+7 (Bianchi et al., 2017) AIS to study the NUV‑r color distribution of our sample. We find counterparts for 67% of the spectroscopically and 54% of the morphologically classified sources. The reason for this is (1) the difference in depths between SDSS and GALEX, and (2) a large fraction of our sources do not have active star formation or have older stellar populations. Figure 2.9 shows the normalized NUV‑r color distribution for our sample split by classification. The left panel shows that star-forming galaxies have a broader distribution of colors ($NUV - r \sim 3 - 6$ mag), while composite galaxies have a narrower distribution peaked at NUV‑r $\sim 2.7$ mag. LINERS and Seyfert 2 galaxies have similar distributions, peaked at $NUV - r \sim 3.3$ mag. The right panel of Figure 2.9 shows the galaxies split by their morphological classification. Elliptical and uncertain galaxies show similar distributions
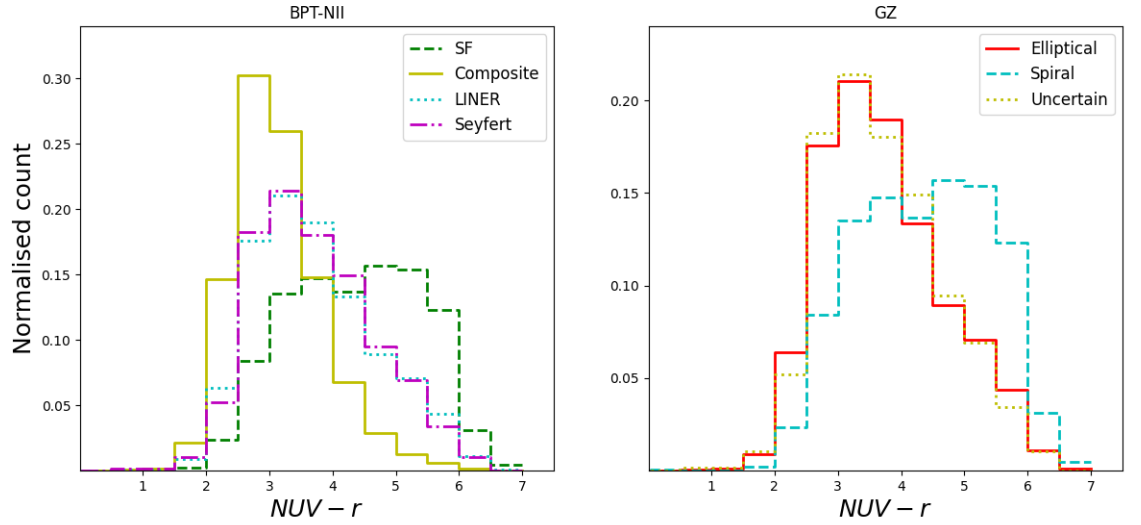
FIGURE 2.9: Distribution of NUV-r for of BPT-NII emission-line classification (left-side) and Galaxy Zoo morphological classification (right panel).

with peaks at $NUV - r \sim 3.3$ mag, whereas spiral galaxies have broader distribution spanning NUV-r $\sim 3 - 6$ mag.

## 2.4 Discussion

Observations and simulations suggest that massive galaxies are dominated by spheroidal components and have predominantly old stellar populations, particularly in their central regions (e.g., De Lucia and Borgani 2012; Ibarra-Medel et al. 2016; James and Percival 2016; Morselli et al. 2016; Nelson et al. 2016; Belfiore et al. 2018; Avila-Reese et al. 2018; Tacchella et al. 2018). Pérez et al. (2013) studied the assembly history of galaxies for different spatial regions (nucleus, inner $0.5R_{50} - R_{50}$, and outer region $> R_{50}$). They find that for the stellar mass range we study here, the great majority of the stars, amounting to 80% of the stellar mass, at the central region ($< 0.5R_{50}$) were assembled a long time ago ($\sim7.1$ Gyr) indicating that low SFRs were in place through the rest of their lifetime, and thus quenching of the star-forming activity must have occurred. The

remaining 20% of the stellar mass would have formed at low SFR and assembled in the past $\sim 2-3$ Gyr. In these massive galaxies, the mean stellar age in the central region is greater than in the outer regions, as discussed earlier (see Section 2.1), indicating that the bulk of the star-formation activity in the central regions was quenched at earlier times.

In this work, we have analyzed the spectroscopic and morphological properties of a sample of SDSS galaxies selected to be in the stellar mass range typical of IOAG candidates (Pérez et al., 2013).

We have spectroscopically classified IOAG candidates using the BPT-NII diagram and found that 20% of them are classified as SF, 40% as composite, 33% as LINERs, and 7% as Seyfert 2. These fractions are different from those obtained by Leslie et al. (2016) using the same data MPA-JHU catalog, but for the entire SDSS sample. For selecting their sample, these authors used S/N criteria of H$\alpha$ line > 3 and three different BPT diagrams, although only 17% of the Leslie et al. (2016) sample is ambiguous galaxies (i.e., do not fall into the same class in all 3 BPT diagrams). They found for the same redshift range that 60.4% of galaxies are SF, 12.2% composite, 6.5% LINER, and 4.1% Seyfert 2. However, regarding the distribution of different spectroscopic types around the MS, we find similar results to Leslie et al. (2016), where the SF galaxies are mainly located on the MS, composites, and Seyferts 2 on and below the MS, and LINERs well below the MS. They also suggested that this sequence supports an evolutionary pathway for galaxies in which star formation quenching by AGN plays a key role. In our study, we found that IOAG candidates with the possible presence of AGN activity were significantly below the MS. Specifically, we found that 83%, 82%, and 98% of those classified as composite, Seyfert 2 and LINERs, respectively,

were below the MS. We note that out of those galaxies selected as LINERs, up to 79% could be photoionized by post-AGB stars instead of AGN activity if we use the EW < 3 Å criterion proposed by Cid Fernandes et al. (2011) to identify them. If this was to be the case, however, it would not alter the main conclusions of our study.

Additionally, we found that although a higher fraction of IOAG candidates are spiral galaxies, those that hosted LINERs are most likely ellipticals compared to the other spectral classes, while those classified as Seyfert 2 galaxies were primarily spirals. While the fact that large fractions of IOAG candidates had unclassified Galaxy Zoo morphologies makes these results difficult to interpret, our analysis suggests that IOAG candidates classified as Seyfert 2 are still spiral galaxies, just as those classified as SF, but have quenched SFRs, comparable to those hosting LINERs. This, combined with the fact that AGN activity is more prevalent in IOAG candidates than in galaxies at other stellar masses (as per the comparison above with Leslie et al. 2016), suggests that these galaxies could be important to study for improving our understanding of galaxy evolution.

We have also investigated the distribution of ellipticals and spirals in relation to the green valley. We can compare our findings, with the results obtained by Schawinski et al. (2014) using the entire SDSS sample at $z < 0.1$. For the same redshift range, we found that galaxies classified as ellipticals in Galaxy Zoo are 88% in the red sequence, 10% in the green valley, and 2% in the blue cloud. Schawinski et al. (2014, see their Table 1), found a slightly bluer distribution for elliptical galaxies, with 82.5%, 12.4%, and 5.2% being in the red sequence, green valley, and blue cloud, respectively. For spirals in our work, we find that 46% are in the red sequence, 28% in the green valley, and 26% in the blue cloud, in contrast to Schawinski

et al. (2014) who found 74.1%, 18.9%, and 7.0%, respectively. This result suggests that IOAG candidates are mainly based in the red sequence and the green valley, with a significant fraction being spirals with quenched star formations.

These results are in line with those obtained in Section 2.3.4 when studying WISE color as a significant number of galaxies are located within the IRTZ (64% of ellipticals, 32% of spirals, and 69% of galaxies that remain unclassified morphologically). As concluded by Alatalo et al. (2014), galaxies laying in the IRTZ are mainly in their late stages of transitioning across the optical green valley, shedding the last of their remnant interstellar media. This again is in line with the analysis of Dn4000 break in Section 2.3.5, where we found that most of the galaxies in our sample have centrally quiescent star-formations (62% and 72% of all galaxies classified spectroscopically and morphologically, respectively).

Our results are in excellent agreement with the recent study by Mc-Partland et al. (2018). They found that the fraction of galaxies hosting AGN activity (composite, LINERs, and Seyfert 2) increases towards the most massive end, making up to 60% of galaxies with $\log M_\star > 10.5\ M_\odot$. We find that 80% of IOAG candidates with a spectral classification host AGN activity. As explained above, we find consistent evidence that AGN host galaxies are located below the MS and present redder colors, yet they are more likely to have spiral morphologies. This could imply that AGN activity in IOAG candidates is associated with galaxies that have recently shut down star-formation activity but are still in the process of transforming their morphologies from spirals to ellipticals.

## 2.5  Conclusions

We have presented a study of galaxies with stellar masses in the range ($\log M_\star = 10.73 - 11.03 M_\odot$) and $z < 0.1$ selected from the SDSS DR8. We use stellar masses and SFRs from the MPA-JHU catalog, together with morphological classification from Galaxy Zoo. Local galaxies in this stellar mass range were identified by Pérez et al. (2013) as having assembly times in their inner regions ($R_{50} < 0.5$) two times shorter than in their outskirts ($R_{50} > 0.5$). We refer to these galaxies as Inside-Out Assembled Galaxies or IOAG candidates. We studied the morphological properties of our galaxies by using the Galaxy Zoo classifications, as well as their spectroscopic properties based on their BPT-[NII] diagram classifications. We find that:

- Using strong enough emission lines with S/N > 3, 20% of IOAG candidates are classified as star-forming galaxies, 40% as composites, 33% as LINERs, and 7% as Seyfert 2. This suggests that 80% of IOAG candidates are not pure star-forming as has been seen previously for the entire SDSS population at $z < 0.1$.

- IOAG candidates classified as star-forming galaxies have spiral morphologies and are located in the MS of star formation as expected, whereas Seyfert 2 and composites have spiral morphologies, but quiescent SFRs, which may point to the idea that the AGN could be related to their SFR quenching and evolution. In addition, taking into account the high fraction of galaxies with AGN, it might be that AGN activity has an important role in quenching SF in IOAG candidates.

- We find that IOAG candidates classified as LINERs show the lowest SFRs (median log SFR/$[M_\odot yr^{-1}]$ of -1.14) and that those with a morphological classification are more commonly spirals (35%) than ellipticals (14%).

- Most of IOAG candidates are spirals rather than ellipticals in the Galaxy Zoo classification scheme, independently of their spectroscopic type (therefore including LINERs). Since they are mainly located in the green valley and the red sequence on the rest-frame color-stellar mass diagram, with a significant fraction being inside the infrared transitional zone using WISE colors, we expect these spirals to be the early-type ones.

Our findings suggest that a high fraction of IOAG candidates are transition galaxies. AGN in this stellar mass range has systematically lower star-formation rates than star-forming galaxies, suggesting AGN activity may be related to this quenching. Galaxies at the stellar mass range of $\log M_\star = 10.73 - 11.03 \ M_\odot$ are moving from star-forming to quiescent, and from the blue cloud to the red sequence and/or to recently quenched galaxies.

# Chapter 3

# An Overdensity of Lyman Break Galaxies Around Hot Dust Obscured Galaxy WISE J224607.56–052634.9

We report the identification of Lyman break galaxy (LBG) candidates around the most luminous hot dust-Obscured galaxy (Hot DOG) known, WISE J224607.56−052634.9 (W2246−0526) at $z =$ 4.601, using deep $r$-, $i$-, and $z$-band imaging from the Gemini Multi-Object Spectrograph South (GMOS-S). We used the surface density of LBGs to probe the megaparsec-scale environment of W2246−0526 to characterize its richness and evolutionary state. We identified LBG candidates in the vicinity of W2246−0526 using the selection criteria developed in the Subaru Deep Field and in the Subaru XMM-Newton Deep Field, slightly modified to account for the difference between the filters used, and we find 37 and 55 LBG candidates, respectively. Matching to the $z$-band depths of those studies, this corresponds to $\delta = 5.8^{+2.4}_{-1.9}$ times the surface density of LBGs expected in the field. Interestingly, the Hot DOG itself, as well as

a confirmed neighbor, do not satisfy either LBG selection criteria, suggesting we may be missing a large number of companion galaxies. Our analysis shows that we have most likely only found those with a higher than average intergalactic medium (IGM) optical depth or moderately high dust obscuration. The number density of LBG candidates is not concentrated around W2246−0526, suggesting an early evolutionary stage for the proto-cluster, that the Hot DOG may not be the most massive galaxy, or that the Hot DOG may be affecting the IGM transparency in its vicinity. The overdensity around W2246−0526 is comparable to overdensities found around other Hot DOGs and is somewhat higher than what is typically found for radio galaxies and luminous quasars at a similar redshift.

## 3.1   Introduction

Active galactic nuclei (AGNs) are some of the most luminous non-transient objects in the Universe. Observational studies have found luminous AGN activity already at the epoch of reionization ($z > 5.5$; see **?**, for a recent review), implying that very massive supermassive black holes (SMBHs) existed only a few hundred million years after the Big Bang (e.g., Mazzucchelli et al., 2017, Yang et al., 2021, Farina et al., 2022). There is strong evidence that luminous AGN activity is linked to galaxy mergers (Treister et al., 2012), although the causality of this relation is still a matter of debate. Numerical simulations strongly suggest that in the early Universe, the most massive SMBHs reside in the densest regions, which are built up from the accretion and merger of massive dark matter halo seeds, and surrounded by a large number of fainter galaxies (Springel et al., 2005, Volonteri and Rees, 2006, Costa et al., 2014, Habouzit et al., 2019). Mergers

and high gas accretion rates, which are both associated with high-density regions, could be driving this very rapid growth, but the attempts to study the environments of these objects based on searches for Lyman-Break Galaxies (LBGs; e.g., Morselli et al., 2014, Husband et al., 2013, Utsumi et al., 2010, Kashikawa et al., 2007, Zheng et al., 2006, García-Vergara et al., 2017, Steidel et al., 2003) and Lyman Alpha Emitters (LAEs; e.g., Kashikawa et al., 2007, García-Vergara et al., 2019) have produced a wide variety of results. This is particularly the case for $z \gtrsim 5$ luminous quasars (e.g., Morselli et al., 2014, Kim et al., 2009). Recently, multiwavelength observational studies with the Very Large Telescope (VLT) and the Atacama Large Millimeter Array (ALMA), have found evidence for a strong clustering of LBGs, LAEs, and CO emitters around quasars at $z \sim 4$ (García-Vergara et al., 2017, 2019, 2022). While searches with ALMA for [CII]158 $\mu$m line emitting companions around a few quasars at $z \sim 6$ (Decarli et al., 2018) and $z \sim 5$ (Nguyen et al., 2020, Trakhtenbrot et al., 2017) have been successful, other studies that focused solely on continuum emitters amd submilimeter galaxies (SMGs) were not (e.g., Champagne et al., 2018, Meyer et al., 2022). These findings are supported by observations of a large number of star-forming galaxies highly clustered around quasars at $z \sim 6$ (e.g., Utsumi et al., 2010, Decarli et al., 2017, Mignoli et al., 2020). Studies of radio-loud AGN at $z \sim 2$ have found them to be good tracers of protoclusters (Wylezalek et al., 2013, Noirot et al., 2016, Magliocchetti et al., 2017, Retana-Montenegro and Röttgering, 2017). At high redshift ($z \sim 5 - 6$), a variety of results have been reported, with some authors finding these quasars trace overdensities (Zheng et al., 2006, Ajiki et al., 2006, Venemans et al., 2007, Bosman et al., 2020). However, some studies found no significant excess of galaxies

in high redshift quasar fields (e.g., Bañados et al., 2013, Simpson et al., 2014, Mazzucchelli et al., 2017), and other studies finding a mix of overdensities and under-densities in the vicinity of quasars at high redshift (Stiavelli et al., 2005, Kim et al., 2009).

Hot dust-obscured galaxies (Hot DOGs, Eisenhardt et al., 2012, Wu et al., 2012) are a population of hyperluminous, obscured quasars, which were identified using the Wide-field Infrared Survey Explorer (WISE; Wright et al., 2010). Due to their high dust obscuration, these objects are detected by WISE at 12 and $22\mu$m and are undetected or faint in the more sensitive 3.4 and $4.6\mu$m bands. The extreme bolometric luminosities of Hot DOGs, $L_{\rm bol} > 10^{13}L_\odot$ (10% of which exceed $10^{14}L_\odot$, Tsai et al. 2015), are powered by accretion onto SMBHs buried under enormous amounts of gas and dust, making them close to Compton-thick in the X-rays (Stern et al., 2014, Assef et al., 2015, 2016, 2020, Piconcelli et al., 2015). The obscuring material absorbs ultraviolet (UV) and optical light, reemitting it as infrared light. Hot DOGs exert significant feedback into their host galaxies by driving massive ionized gas outflows (Díaz-Santos et al., 2016, Finnerty et al., 2020, Jun et al., 2020). Together, these studies suggest that Hot DOGs may be probing a critical stage in the evolution of their host galaxies, in which quasar feedback is starting to shut down star formation by ejecting significant amounts of cold gas and transitioning into a UV-bright traditional quasar (e.g., see Assef et al., 2020, Tsai et al., 2018, Wu et al., 2018). Notably, Assef et al. (2015) found that the number density of Hot DOGs is similar to that of equally luminous type 1 AGN at $2 < z < 4$, with an effective number surface density of 1 per $31 \pm 4$ deg$^2$.

Multiwavelength observations of Hot DOGs have statistically shown that these objects are likely to live in dense environments (Assef

et al., 2015, Jones et al., 2014, Penney et al., 2019). More recently, Luo et al. (2022) found an overdensity of distant red galaxies (DRGs) around a Hot DOG at $z = 2.3$, while Ginolfi et al. (2022) revealed an overdensity of LAEs in the environment of a $z = 3.6$ Hot DOG with VLT/MUSE observations. All of this evidence suggests that Hot DOGs exist in overdense regions of the Universe, where significant gas accretion can be maintained and mergers could lead to large-scale obscuration. Furthermore, Díaz-Santos et al. (2018) found that WISE J224607.56−052634.9 (hereafter, W2246−0526), the most luminous Hot DOG known with $L_{\mathrm{Bol}} = 3.6 \times 10^{14} L_{\odot}$ (Tsai et al., 2015) and at redshift $z = 4.601$ (Díaz-Santos et al., 2016), is found at the center of a multiple merger system (Díaz-Santos et al., 2018). Using deep ALMA observations, Díaz-Santos et al. (2016, 2018) revealed three spectroscopically confirmed companion galaxies with disturbed morphologies and four sources as potential companions within ∼30 kpc. They found that W2246-0546 lives in a dense local environment and speculate that it may become the brightest cluster galaxy (BCG) of a galaxy cluster at redshift 0. Díaz-Santos et al. (2016) show that this object is likely in a key stage of its evolution, experiencing isotropic outflows of atomic gas. However, the evidence of overdense environments so far has come through deep ALMA observations encompassing a spatial scale of only ∼30 kpc. There have not yet been detailed studies of the environments of this object on larger scales (>30 kpc), which is relevant to assess its megaparsec-scale environment. Further characterizing the environments of Hot DOGs, such as W2246−0526, is critical to understand how galaxies evolve over cosmic time and the physical processes driving their evolution.

The Lyman break identification technique (e.g., Giavalisco, 2002,

Steidel et al., 1996, 1999) is commonly used to select star-forming galaxies at $z > 2$. Star-forming galaxies at high redshift selected with this method are known as LBGs. The technique uses broadband photometry, typically with three bands that bracket the Lyman break to identify sources that are faint in the bluest band due to redshifted hydrogen absorption but have the flat continuous UV emission typical of star-forming galaxies in the two redder bands. As the Lyman alpha forest opacity increases with redshift at $z > 4$, a large number of LBGs have been identified using the combination of Lyman break and Lyman alpha absorption (Ouchi et al. 2004, hereafter O04; Yoshida et al. 2006, hereafter Y06).

In this work, we probe the environment within 1.4 Mpc of W2246−0526 by studying the surface density of nearby LBGs. Specifically, we study LBG candidates at redshift $z \sim 4.601$ selected as $r$-band dropouts in deep Gemini Multi-Object Spectrographs South (GMOS-S) imaging using the selection functions of O04 and Y06, modified to fit our specific set of filters. The work is organized as follows. In Section 3.2, we describe the observations from GMOS-S, the data reduction, and the photometric measurements. In Section 3.3, we discuss modifications to the color selection function of O04 and Y06 to accommodate the GMOS-S filters used. We also study the color and space distribution of the LBG candidates as well as their luminosity function. In Section 3.4, we compare our results with other Hot DOG and quasar environments in the literature. We present our conclusions in Section 3.5. Throughout this work, all the magnitudes are in the AB system. We assume a flat $\Lambda$CDM cosmology with $H_0 = 70 \ \mathrm{km \ s^{-1} \ Mpc^{-1}}$ and $\Omega_M = 0.3$. At a redshift of z = 4.601, W2246−0526 is observed at 1.3 billion years after the Big Bang, and an observed spatial scale of $1''$ is equal to 6.5 kpc.

## 3.2 Observations

We obtained GMOS-S deep imaging in the $r$-band on the nights of UT2017-09-16 and UT2017-09-23, in the $i$-band on the nights of UT2017-09-16 and UT2017-09-27, and in the $z$-band on the night of UT2017-09-23, (program ID: 102 207-33Q, P.I: R. J. Assef). During our observations, the average seeing conditions in the $r$-, $i$-, and $z$-bands were $0.52''$, $0.61''$, and $0.58''$, respectively. The observations were taken with an average airmass of 1.1 for the $r$-band, 1.3 for the $i$-band, and 1.2 for the $z$-band. All images were obtained with a pixel scale of $0.16''$ $\mathrm{pix}^{-1}$. We obtained 25 and 24 images with exposure times of 300 seconds each in the $r$- and $i$-bands, respectively, and 62 in the $z$-band with an exposure of 100 seconds to avoid the sky emission becoming nonlinear. The observations are summarized in Table 3.1. The field of view of the instrument is 5.5 arcmin $\times$ 5.5 arcmin and observations were obtained by dithering with a grid of 4 by 3 with 6 arcsec intervals for the $r$- and $i$-bands, and a grid of 6 by 5 for the $z$-band.

### 3.2.1 Data reduction

We reduced the GMOS-S data using the Gemini package in `IRAF` V2.16 through the Python `PyRAF`[1] interface. We use the GMOS package to bias-correct, and flatfield the images. We combined the images using the Gemini imcoadd task. We find, however, that the extended glow of two heavily saturated bright stars ($r < 20$ mag) in the field results in a very uneven background in the final image obtained using this task, so we have instead decided to subtract the extended glow of these stars from each frame before combining

---

[1] https://iraf-community.github.io/pyraf.html

TABLE 3.1: Information on the GMOS-S observations used in this work

| Band | Exposure Time | Mean Seeing | Mean Airmass | UT Dates | Depth of the Stack Image 5 $\sigma$ /3 $\sigma$ /1 $\sigma$ |
|------|---------------|-------------|--------------|----------|------------------------------------------------------------|
| r | 25 × 300s | 0.52″ | 1.1 | 2017-09-16/23 | 27.29/27.84/29.00 |
| i | 24 × 300s | 0.61″ | 1.3 | 2017-09-16/27 | 26.58/27.16/28.34 |
| z | 62 × 100s | 0.58 ″ | 1.2 | 2017-09-23 | 26.02/26.57/27.77 |
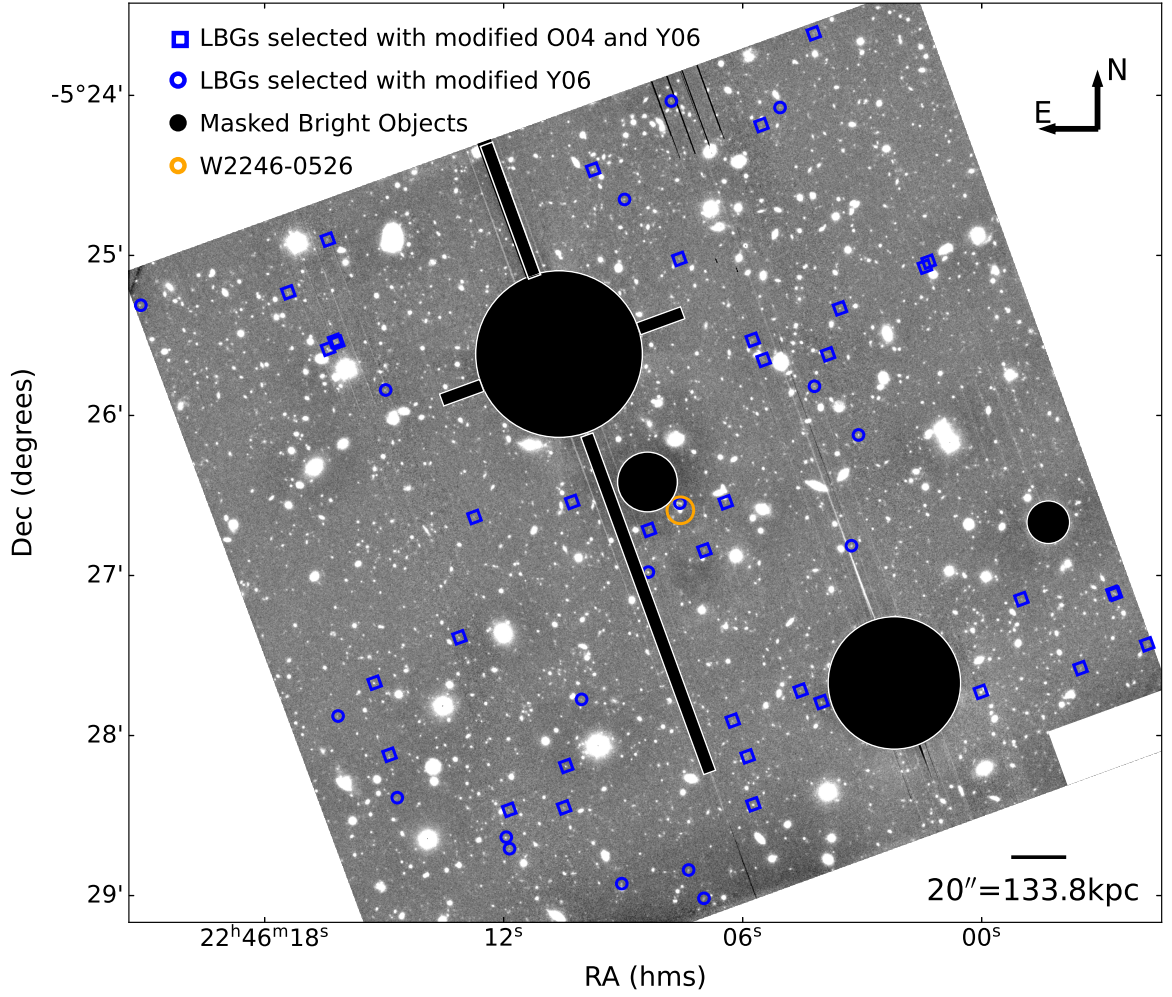
FIGURE 3.1: *i*-band image of W2246−0526. Black circles and rectangles show the masked area that we did not use for our LBG selection (see Section 3.2.2 for details). The 5 arcsec radius solid orange circle indicates the position of the W2246−0526, 4 by 4 arcsec blue rectangles show the LBG candidates selected with the modified O04 and Y06 selection criteria (see Table 3.3), and the 3 arcsec radius blue circles show those selected with the modified Y06 selection criteria only (see Fig. 3.5 and Table 3.4). There are no LBG candidates present in the SE corner of the image that has been clipped.

them. Specifically, we masked all sources of each fully reduced frame detected at $> 5\sigma$ by the `DAOStarFinder` routine of the `photutils`[2] Python package. Most sources were masked with a 15-pixel radius circle, but larger radii were used for brighter sources. We modeled the source-subtracted images as a combination of two Moffat profiles (one for the extended glow of each star) and a flat background. Then, we subtracted the best-fit Moffat profiles and coadded the resulting

---

[2]https://photutils.readthedocs.io/en/stable/

images without correcting for dithering to create an illumination correction frame. As observations for some bands were obtained across multiple nights, we created one illumination correction frame per night per band. Finally, each Moffat-profile subtracted frame was corrected by the appropriate illumination frame[3]. The corrected frames were finally stacked using the imcoadd task of the Gemini `IRAF` package. The reduced $i$-band image is shown in Fig. 3.1.

### 3.2.2 Photometry

Using the `astroalign` Python module, we aligned the $r$- and $z$-band images to the $i$-band image. We then used `SExtractor`[4] (Bertin and Arnouts, 1996) for source detection and photometry. Specifically, we measured the photometry in fixed $2''$ diameter apertures with `SExtractor` in dual image mode using the $i$-band image for source detection. We used a detection and analysis threshold of at least 3 pixels detected above $1.5\sigma$. We used a global model for the background with mesh and filter sizes of 32 and 3, respectively. We carried out the source detection in the $i$-band and used those positions to obtain photometric measurements in all three bands. We masked out the bright stars and their spikes and cut off the borders of the images (as well as regions not covered by all three bands) to avoid spurious sources. The final $i$-band image with the masking applied is shown in Fig. 3.1. We estimated the usable area by generating $10^6$ random uniform points, distributed throughout the image, and counting the fraction of unmasked points. The usable area remaining after the masking is 23.7 arcmin$^2$. For reference, the masked regions in Fig. 3.1 account for 13% of the combined field of view.

---

[3]The scripts to subtract the Moffat-profiles, create and apply the illumination corrections can be found at https://github.com/rjassef/GMOS_W2246_ICMS

[4]`SExtractor` version 2.5.0 https://www.astromatic.net/software/sextractor/

The photometric calibration was carried out using data from the Panoramic Survey Telescope & Rapid Response System (Pan-STARRS) Survey (Tonry et al., 2012). We only considered point sources, selected using the probabilistic classification of unresolved point sources with `ps_score` greater than 0.83 as suggested by Tachibana and Miller (2018)[5]. The Pan-STARRS point sources were cross-matched with the sources from our imaging using a 1 arcsec radius. We find 36 Pan-STARRS point sources within the unmasked area of our images. To estimate the photometric calibration constant, we only consider sources with magnitudes $19 < i < 21$ (21 sources), $19 < r < 21.7$ (18 sources), and $17 < z < 20.4$ (21 sources) in Pan-STARRS. These magnitude limits are meant to avoid sources bright enough to be in the nonlinear regime of the GMOS observations as well as poorly detected sources in Pan-STARRS. We fit for the photometric calibration of the GMOS data in $r$-band using $g - r$ and $r - i$ colors, in $i$-band using $r - i$ and $i - z$ colors, and in $z$-band using $i - z$ color. These corrections were required to obtain an accurate calibration (see Section 3.3.1) given the differences between the instruments and filters. We applied the $3\sigma$ detection catalog limit to the $i$ (27.16) and $z$ (26.57) bands.

### 3.2.3 Detection completeness

We estimate the detection completeness as a function of the $i$-band apparent magnitude since our LBG candidates were selected from sources detected in the $i$-band image. The detection completeness was estimated using a Monte Carlo simulation. Specifically, we injected 100 mock sources into the $i$-band image with a Gaussian PSF with a full-width-at-half-maximum (FWHM) of 0.61 arcsecs (i.e., the

---

[5]https://outerspace.stsci.edu/display/PANSTARRS/How+to+separate+stars+and+galaxies

average seeing in this band). We randomized the positions of the injected sources across the *i*-band image and found that 92 sources fell within the unmasked region. We ran `SExtractor` to recover the injected sources using the same procedure described in Section 3.2.2. We repeated this process by changing the magnitude of the injected sources in the range between 24.1 to 27.0 mag in steps of 0.1 mag. The recovered fraction of injected sources is shown in Fig. 3.2 as a function of the input magnitude. As expected, the completeness sharply decreases with increasing magnitude when approaching the $3\sigma$ limit of the observations.
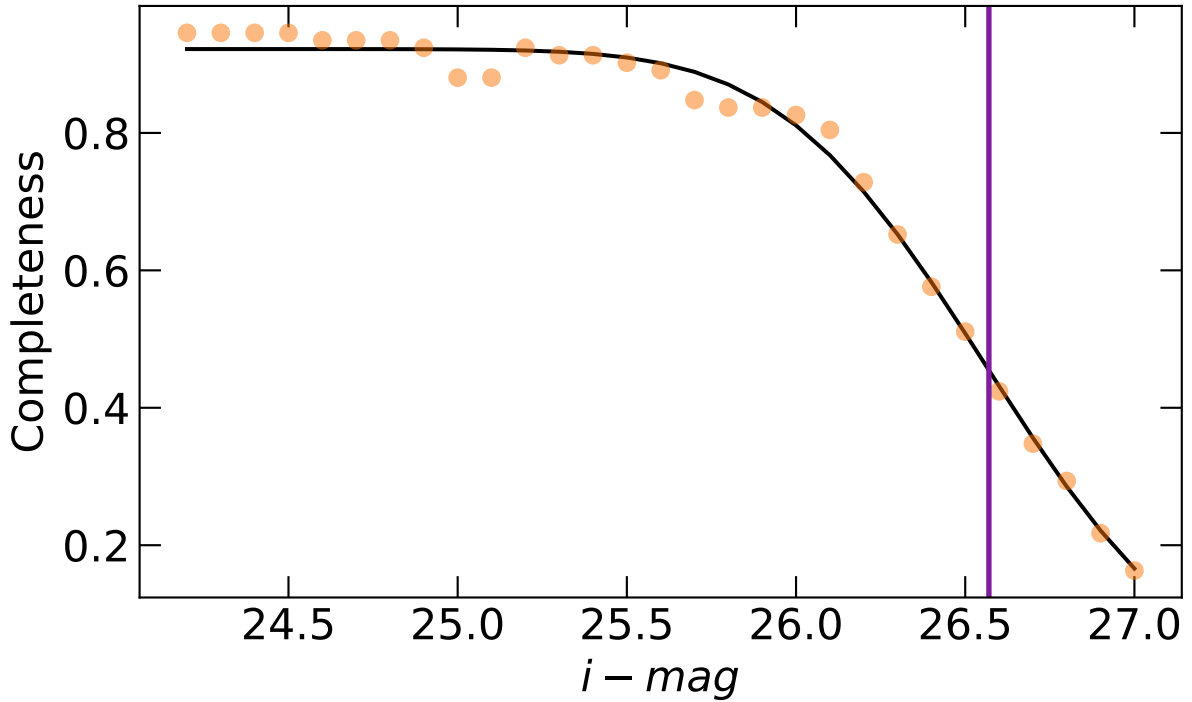


FIGURE 3.2: Detection completeness in the *i*-band image. The dots show the completeness as a function of the apparent magnitudes in the *i*-band solid black line shows the best fit to the detection completeness. The vertical purple line shows the $3\sigma$ limit of our *z*-band observation.

We fit the recovered fraction of injected sources using an error function. Specifically, we fit the completeness $\rho$ as

$$\rho(m_i) = \frac{1}{2}\alpha[1 - erf(\frac{m_i - \mu}{\sigma})], \tag{3.1}$$

where $m_i$ is the $i$-band apparent magnitude, and $\alpha$, $\mu$, and $\sigma$ are fit to the data. We find that the completeness is best modeled by $\alpha$=0.92, $\mu$=26.56, and $\sigma$=0.68.

## 3.3   Selected Lyman break galaxy candidates

### 3.3.1   Modified method to identify LBG candidates

We used the LBG color selection criteria proposed by O04 and Y06. In general, the Y06 criteria is a more permissive version of the O04 criteria aimed at obtaining a larger number of LBG candidates. Both of them were developed using observations obtained with the Subaru Telescope Suprime-cam instrument. We consider them representative of the average surface density of sources in the sky. Both studies used the $R_{\mathrm{c}}$-, $i$-, and $z$-band imaging of the Subaru Deep Field (SDF) and while O04 also used observations of the Subaru XMM-Newton Deep Field (SXDF). Since the Suprime-cam filters do not exactly match the GMOS-S $r$-, $i$-, and $z$-bands (see Fig. 3.3), we modify the selection function to ensure that the contamination level by interlopers of our sample is consistent with that of the samples of O04 and Y06.

We used the $z \sim 3$ LBG composite spectrum from Shapley et al. (2003) to estimate the changes needed to be applied to the O04 and Y06 selection criteria to accommodate the GMOS filter set. At z=4.601, we expect significantly more IGM absorption shortward of Ly$\alpha$ than at $z \sim 3$. Therefore, in order to incorporate the expected excess absorption at $z = 4.601$, we used the Madau (1995) model,
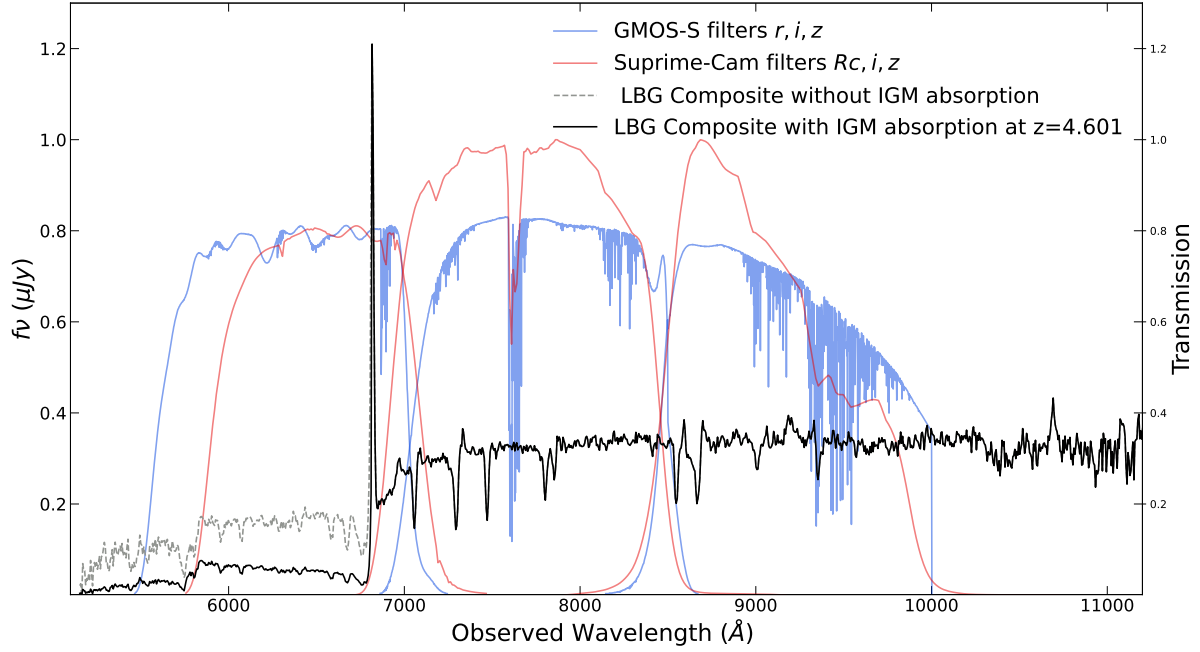
FIGURE 3.3: Composite LBG spectrum of Shapley et al. (2003), with the IGM absorption at $z = 3$ and shifted to $z = 4.601$ (grey-shaded line), and the IGM absorption correction at $z = 4.6$ (black-solid line). See text for further details. After accounting for quantum efficiency and atmospheric transmission, the blue and the red solid line are the GMOS-S (used in this work) and Subaru Suprime-cam filter curves, respectively.

adding a parameter $\kappa$ to account for variations in the IGM optical depth. The equation we used to incorporate the dispersion and excess absorption is as follows:

$$f_\nu^{(\mathrm{LBG})}(z = 4.6) = f_\nu^{(\mathrm{LBG})}(z = 3) \exp\left(-\kappa\tau_{\mathrm{eff}(z=4.6)} + \tau_{\mathrm{eff}(z=3)}\right) \quad (3.2)$$

where $\tau_{\mathrm{eff}}$ corresponds to the mean optical depth of the Madau (1995) model.

As can be seen in Fig. 3 of Madau (1995), there is a significant dispersion around the mean optical depth of IGM absorption, $\tau_{\mathrm{eff}}$, at $z \sim 3.5$. We find that the $1\sigma$ range in that Figure corresponds to $\kappa = 0.18$ to $2.69$ times the mean optical depth at $z \sim 3.5$. We later consider this range of $\kappa$ values when assessing the effectiveness of our selection.

Figure 3.3 shows the LBG composite spectrum of Shapley et al. (2003) shifted to $z = 4.601$ assuming the mean IGM optical depth at this redshift (i.e., $\kappa = 1$ see in Eq. 3.2). The Figure also shows, for comparison, the same LBG composite spectrum but corrected for IGM absorption.

To estimate the modifications to the selection function, we computed the expected photometry of this LBG template at $z = 4.601$ for $\kappa = 1$ and the Suprime-cam filters used by O04 and Y06 and in the GMOS-S bands using the `synphot` package[6]. The transmission curves of the GMOS-S and Subaru Suprime-cam filters were obtained from the Spanish Virtual Observatory (SVO)[7]. Subaru SuprimeCam's $i$ and $z$ filter transmissions are available considering the pass-band and atmospheric transmissions as well as the quantum efficiency, but for the $R_{\mathrm{c}}$ band only the passband transmission is available. For the GMOS-S filters, only the pass-band transmission is available. We used the quantum efficiency of the respective CCDs[8] and the expected atmospheric transmission[9] to construct the full transmission curves for these filters.

We calculated the colors of the LBG template redshifted to $z = 4.601$ with $\kappa = 1$ to be $(r - i) = 1.18$, $(i - z) = 0.058$, $(Rc - i_{\mathrm{S}}) = 0.95$ and $(i_{\mathrm{S}} - z_{\mathrm{S}}) = 0.075$. Applying this color difference, we can write the O04 selection criteria in the GMOS-S bands as:

---

[6]https://synphot.readthedocs.io/en/latest/.

[7]http://svo2.cab.inta-csic.es/svo/theory/fps3/index.php?mode=browse

[8]quantum efficiency of Subaru Suprime-cam CCDs https://www.subarutelescope.org/Observing/Instruments/SCam/ccd.html and the GMOS-S CCDs http://www.gemini.edu/instrumentation/gmos/components#GSHam

[9]Based on the location of the two instruments, we get the atmospheric transmission for both instruments using the Sky Model Calculator https://www.eso.org/observing/etc/

$$r - i > 1.43,$$

$$i - z < 0.683,$$

$$r - i > i - z + 1.247, \tag{3.3}$$

and the Y06 selection criteria in the GMOS-S bands as:

$$r - i > 1.23,$$

$$i - z < 0.683,$$

$$r - i > 1.2(i - z) + 1.15. \tag{3.4}$$
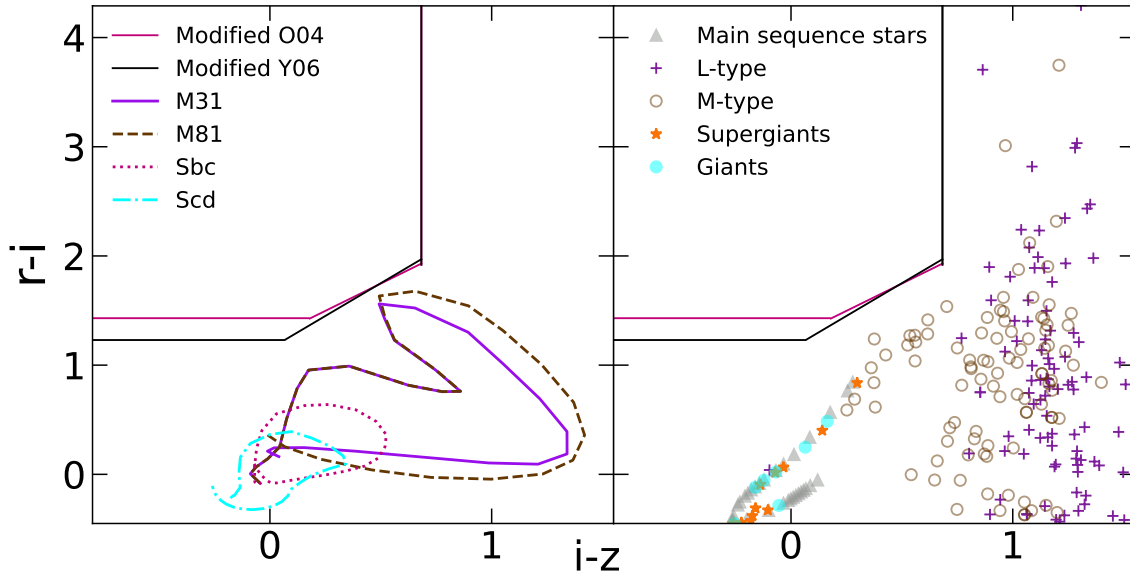


FIGURE 3.4: $r - i$ vs $i - z$ color-color diagram used in this work to select LBG candidates and exclude contaminants. The solid magenta and black lines define the selection boundaries in the color diagram established by the modified color selection criteria from O04 and Y06, respectively. In the left panel, we show the representative colors of several classes of galaxies from Coleman et al. (1980) as a function of redshift from z= 0 to 3. In the right panel we show the colors of different types of stars, from main-sequence to brown dwarfs, obtained by using models of stellar atmospheres from Castelli and Kurucz (2004) and brown dwarf spectra from Burgasser (2014) .

To assess if our modified selection could be differently affected by contamination from stars and lower redshift galaxies, we follow a

similar procedure as O04. Figure 3.4 shows the colors of representative galaxy templates from Coleman et al. (1980), shifted in the redshift range $0-3$. The figure also shows the colors of the main sequence, giant, and super-giant stellar atmosphere models of Castelli and Kurucz (2004) and of the M and L dwarfs of Burgasser (2014). Figure 3.4 shows that our modified selection should not be more affected by contaminants than the O04 selection (see their Fig. 6) or the Y06 selection.

Figure 3.5 shows the color tracks for the LBG composite spectrum of Shapley et al. (2003), modified for the changes in the IGM absorption expected through Eq. (3.2). We show the colors expected for the typical absorption ($\kappa = 1$) as well as for $\kappa = 0.18$ and $\kappa = 2.69$ (see above). We find that neither the O04 nor the Y06 selection is able to identify an LBG at $z = 4.601$ with $\kappa = 1$, assuming the Shapley et al. (2003) composite spectrum, as O04 identifies sources with $z > 4.715$, and Y06 with $z > 4.625$. Figure 3.5 also shows how colors at $z = 4.601$ change due to dust absorption, assuming the reddening law of Calzetti et al. (2000). While the figure shows that LBGs with typical IGM absorption and no dust reddening would not be selected, an increase in either parameter can shift the sources into the selection region. Figure 3.6 shows the relation between the minimum value of $\kappa$ and the minimum value of $E(B-V)$ needed to shift our assumed LBG spectrum (Eq. [3.2]) into the O04 and Y06 selection boxes. While unreddened sources would need $\kappa = 1.4$ ($\kappa = 1.08$) to appear inside the O04 (Y06) selection box, sources with $\kappa = 1$ would only need a moderate amount of obscuration with $E(B-V) = 0.34$ [$E(B-V) = 0.08$] to be shifted into the selection region. We note too that as reddening affects the $i-z$ color, a maximum amount of reddening of $E(B-V) = 1.53$ can be

tolerated before $z = 4.601$ LBGs escape through the left boundary of the selection region. This suggests our selection is likely missing a significant amount of sources with less reddening/IGM absorption than the minima in Fig. 3.6.

Although we assume all sources are at $z = 4.601$ (in contrast to the assumption of $z = 4.9$ by both O04 and Y06), we need to find out the redshift range over which our modified criteria can find LBGs. As shown in Fig. 3.5, the modified selection criteria of O04 yield redshift intervals of $4.715 < z < 5.361$ and of Y06 are $4.625 < z < 5.361$, for $\kappa = 1.0$, the mean IGM absorption of Madau (1995). While we assume $\kappa=1$ for simplicity to estimate the volume over which our sources are found, for completeness we note that the redshift range for $\kappa = 2.69$, the upper $1\sigma$ range of the Madau (1995) IGM absorption distribution, is $z = 4.477$ to $z = 5.277$ which is comparable to the range found by O04 ($z = 4.6 - 5.2$) and when we used the modified selection criteria of Y06 ($z = 4.7 - 5.1$), we found the redshift range to be $z = 4.401$ to $z = 5.277$.

We tested the modified selection function that would be obtained by doing the same analysis but using instead the mock spectrum at $z = 4.601$ from the JWST Advanced Deep Extragalactic Survey (JADES; Williams et al. 2018). We find that using these spectra instead of the Shapley et al. (2003) composite to calculate the color changes between the filter sets results in a very similar, yet slightly more permissive version of the selection criteria in Eqs. (3.3) and (3.4). Given this, and the fact that the JADES mock spectrum is estimated for much fainter galaxies than the LBG candidates targeted here, we use the selection based on the Shapley et al. (2003) LBG composite spectrum.

### 3.3.2 Selected LBG candidates

Using the modified O04 selection criteria, we identified 41 LBG candidates within the unmasked regions of our images. Of these, 4 have their photometry potentially contaminated by nearby CCD features as assessed by visual inspection, so we discard them. Of the remaining 37 LBG candidates, 27 are brighter than the $1\sigma$ limit in the $r$-band. Using the modified Y06 selection criteria, we identified instead 55 candidates unaffected by CCD features and 45 of them are brighter than the $1\sigma$ limit in the $r$-band. Photometry and cutout images in $r$, $i$, and $z$-band of all candidates and the Hot DOG provided in the Appendix in Tables 3.3 and 3.4 and Figs. 3.13 - 3.14.
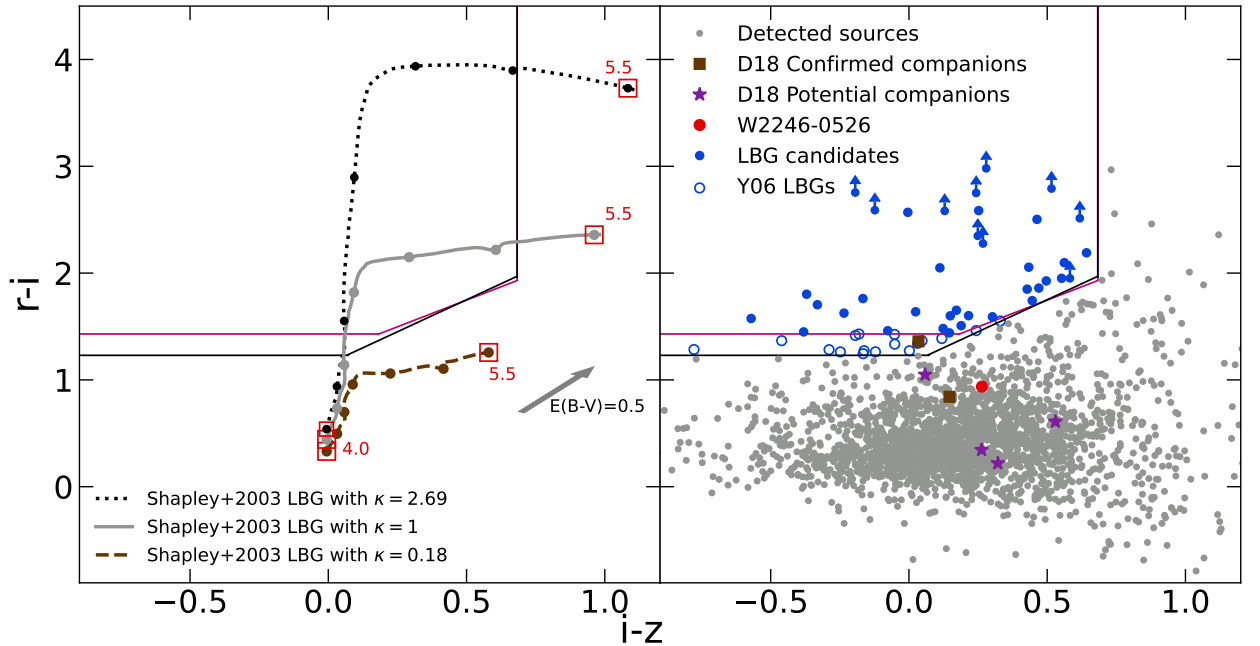


FIGURE 3.5: Left panel: Color-redshift track of the LBG composite spectrum of Shapley et al. (2003) with the IGM absorption of Madau (1995) as described in Eq. (3.2) for values of $\kappa$= 2.69 (dotted black line), 1.0 (solid grey line), and 0.18 (dashed brown line). The open red squares mark the $z = 4.0$ and $z = 5.5$ endpoints of each color-redshift track. The dots in each track indicates $\Delta z = 0.25$ bins. Right panel: Distribution of the $r - i$ and $i - z$ colors of sources around W2246$-$0526 (grey dots). The blue-filled circles show the LBG candidates identified by both the O04 and Y06 selection criteria. The blue open circles show the LBG candidates identified by only the Y06 selection criteria. The spectroscopically confirmed (brown squares) and potential (purple star) companions from Díaz-Santos et al. (2018) are also shown, and the red dot shows the Hot DOG. Ten of the identified LBG candidates are fainter than $1\sigma$ in the $r$-band, and hence their $(r - i)$ Colors are shown as lower limits.
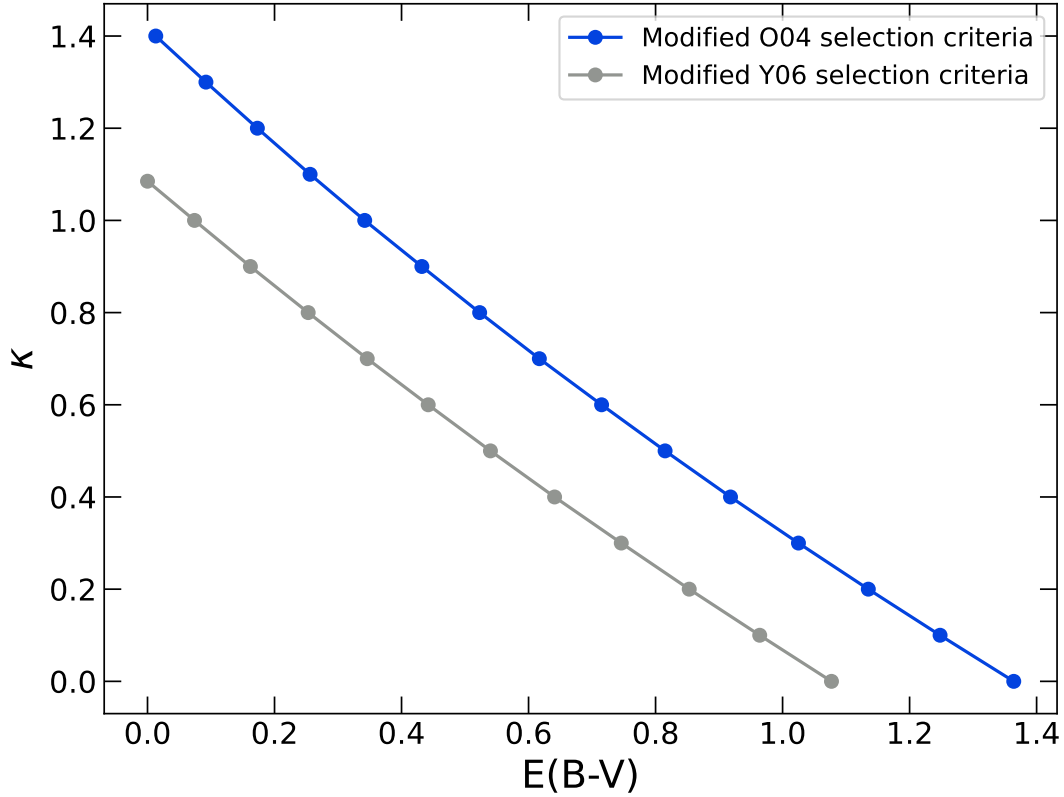
FIGURE 3.6: Relation between the minimum value of the $\kappa$ and the minimum value of $E(B-V)$ that shift the Shapley et al. (2003) LBG composite spectrum at $z = 4.601$ into the modified selection criteria of O04 and Y06. In both modified selection criteria, the selected sources with $\kappa = 1$ would only require a moderate amount of obscuration with $E(B-V) = 0.34$ and $(E(B-V) = 0.08)$ to be shifted into the modified O04 and Y06 selection box

Figure 3.5 shows the color distribution diagram of all detected objects in the W2246−0526 field, with those selected as LBG candidates highlighted in blue. We also highlight the locations of W2246−0526 and of the companions (both potential and with spectroscopic confirmation) identified with ALMA data by Díaz-Santos et al. (2016) and Díaz-Santos et al. (2018). Interestingly, the modified O04 selection criteria do not identify the Hot DOG, and the previously identified companions (Díaz-Santos et al., 2018) as LBG candidates. However, the spectroscopically confirmed companions are closer to the selection box than the potential companions, suggesting the latter may be interlopers. We note that we are comparing populations of detected galaxies that were obtained in different ways. Using the modified
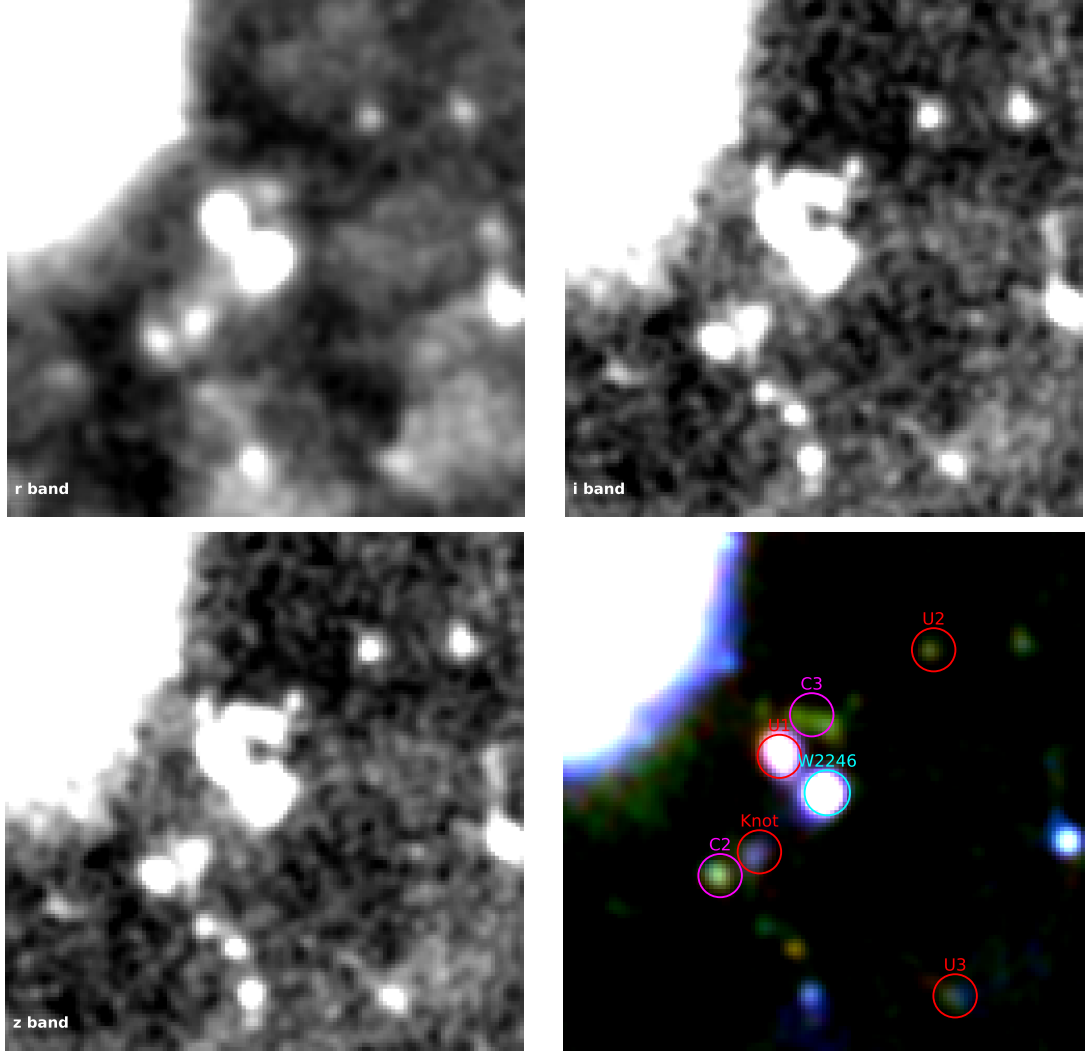
FIGURE 3.7: Postage stamps (20″ x 20″) of W2246-0526 with similar field of view of deep ALMA observation by Díaz-Santos et al. (2016) and Díaz-Santos et al. (2018). The top-left panel is *r*-band, the top-right panel is the *i*-band, the bottom-left panel is *z*-band and the bottom-right panel is the color composite of W2246-0526. The spectroscopically confirmed and potential companions of Díaz-Santos et al. (2016, 2018) are shown in magenta and red circles, respectively. The Hot DOG is shown by the cyan circle. Cutouts of 8″ x 8″ of each of the marked sources are shown in Fig. 3.15.

Y06 selection criteria, we were able to identify one of the spectro-scopically confirmed companions as an LBG candidate. Figure 3.7 shows a zoomed-in view of a field that closely resembles the field of view of the deep ALMA observations of Díaz-Santos et al. (2018). Additionally, we have marked the locations of spectroscopically con-firmed and potential companion galaxies identified by Díaz-Santos et al. (2016) and Díaz-Santos et al. (2018), and their stamps of 8″ x

8″ are shown in Figs. 3.15.

Figure 3.8 shows the magnitude distribution of the selected LBG candidates in the three bands. For the $r$-band, we only show sources brighter than the $1\sigma$ limit. The $i$- and $z$-band magnitudes have similar distributions, which is expected since LBGs have, by definition, flat UV SEDs. Figure 3.1 shows the $i$-band image with the position of the selected LBG candidates based on the modified O04 and Y06 selection criteria.
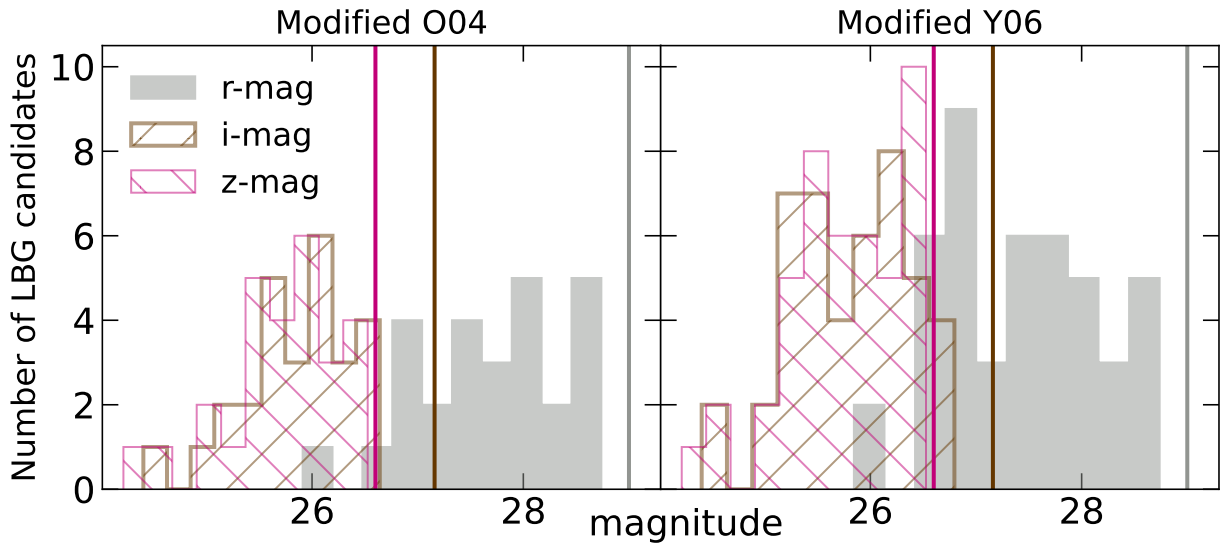


FIGURE 3.8: Left and right panels show the magnitude distribution of the LBG candidates selected with the modified O04 and Y06 selection criteria, respectively, in each band. The $r$-band magnitude distributions only show the LBG candidates that are brighter than the $1\sigma$ limit. The three vertical lines are the $3\sigma$ magnitude limit for the $i$-band (brown) and $z$-band (purple) and the $1\sigma$ magnitude limit for the $r$-band (grey).

### 3.3.3   Surface density of selected LBG candidates

Figure 3.9 compares the number counts of LBG candidates in the field of W2246−0526, as a function of apparent $z$-band magnitude, to those measured by O04 in the SDF and SXDF areas, and to those measured by Y06 using only the SDF. In both studies, the number counts were not corrected for detection completeness. Figure

3.2 shows the detection completeness corrections and the corrected number counts in the field of W2246−0526 are shown alongside the uncorrected ones in Fig. 3.9. For simplicity, we estimate the uncertainties of our surface density as the square root of the number of LBG candidates in each magnitude bin, neglecting cosmic variance.
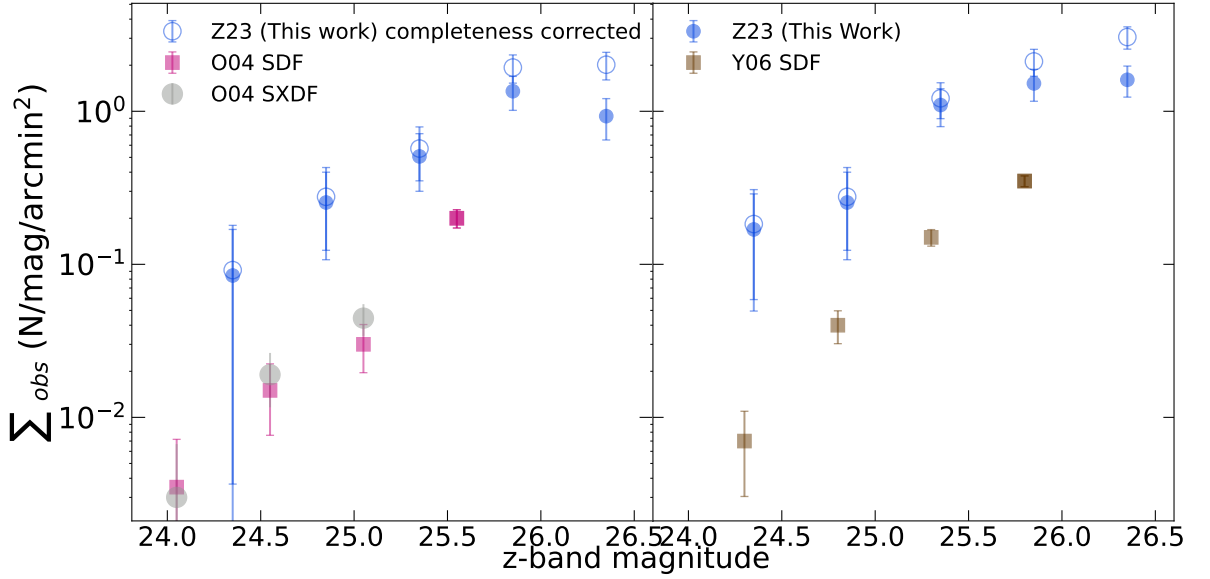


FIGURE 3.9: Surface density of the selected LBG candidates (filled blue circles) and LBG candidates corrected for completeness (open blue circles) compared to that measured in the SDF field by O04 and Y06 (magenta and brown squares, respectively). We also show the measurement of LBG number counts in the SXDF field by O04 (filled grey circles).

Based on the modified O04 and Y06 selection criteria, we find 37 and 55 LBG candidates, respectively, by matching the $z$-band magnitude depth in the field studies. We estimate the overdensity, $\delta = N_{found}/N_{expected}$, to be $\delta = 7.1 \pm 1.1$ ($\delta = 5.1 \pm 1.2$) when compared with the O04 study of the SDF (SXDF). On the other hand, we measure $\delta = 5.2 \pm 1.4$ when compared with the Y06 study of the SDF field. The average overdensity is hence $\delta = 5.8^{+2.4}_{-1.9}$.

### 3.3.4 Spatial distribution of the LBG candidates

To gauge whether the two-dimensional overdensity is concentrated around W2246−0526, we count the number of LBG candidates in annuli with widths of 20 arcsecs, centered on W2246−0526 and starting 2 arcsecs (∼13 kpc) away from the Hot DOG, The brightness of W2246-0526 interferes with the detection of candidates at smaller radii. We estimate the unmasked area of each ring using randomly distributed points within each ring and counting the unmasked fraction. Figure 3.10 shows the density of LBG candidates as a function of distance to the Hot DOG. While the highest density of LBG candidates is in the second ring around W2246−0526, there is not a clear radial profile centered on this Hot DOG. As done earlier, for simplicity, we estimate the uncertainties as the square root of the number of LBG candidates found in the ring divided by the usable area of the ring.

### 3.3.5 Luminosity function of Lyman break galaxy candidates

We estimate the UV luminosity function of our LBG candidates at rest-frame wavelength 1700Å following the approach of O04. Specifically, we estimate a correction to transform the $z$-band (rest-frame effective wavelength = 9521.7Å at $z$ = 4.601) magnitude into a monochromatic flux at 1700Å using the `synphot` package with the LBG composite of Shapley et al. (2003). We assume a top-hat band pass at rest-frame 1700Å with a ±5Å width. Given that the $z$-band is already covering a region close to that of rest-frame 1700Å, we find an almost negligible $k$ correction of 0.022 mag. Finally, we convert the $z$-band apparent magnitude by using the following equation.
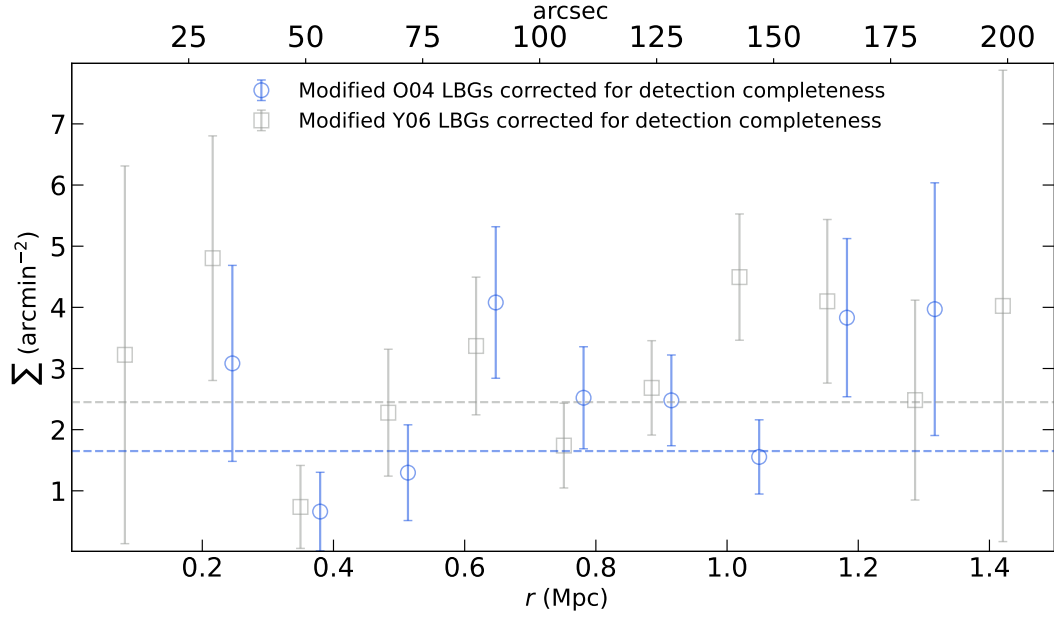
FIGURE 3.10: Spatial distribution of LBG candidates as a function of distance to W2246−0526. The blue open circles and gray open squares show the selected LBG candidates based on the modified O04 and Y06 selection criteria, respectively, corrected for detection completeness. We count the number of LBG candidates in annuli with 20 arcsec radius intervals avoiding the inner 2 arcseconds (∼13 kpc). For clarity, we shift the surface density of the O04 selected LBG candidates by +0.03 Mpc on the x-axis.

$$M_{1700 \text{ Å}} = m_z + 2.5 \log(1 + z) - 5 \log dl + 5 - k, \qquad (3.5)$$

where $m_z$ is the apparent magnitude in the $z$-band and $dl = 42305.5$ Mpc, is the luminosity distance at $z = 4.601$.

Similarly, we follow Y06 to estimate the UV luminosity function of our LBG candidates at 1500Å in the rest-frame for which we calculate a $k$ correction of -0.015.

We estimate the effective volume $V_{\text{eff}}$ on which our sample is found as the comoving volume between the $z_{\text{min}}$ and $z_{\text{max}}$ redshifts of each selection (see Section 3.2.3) within our field of view of 23.7 arcmin$^2$. For the O04 and Y06 selections, this corresponds to 20638.77 Mpc$^{-3}$

and 23633.09 Mpc$^{-3}$ respectively. We computed the luminosity function from the observed number density of the completeness corrected $z$-band at the UV rest-frame using these comoving volumes:
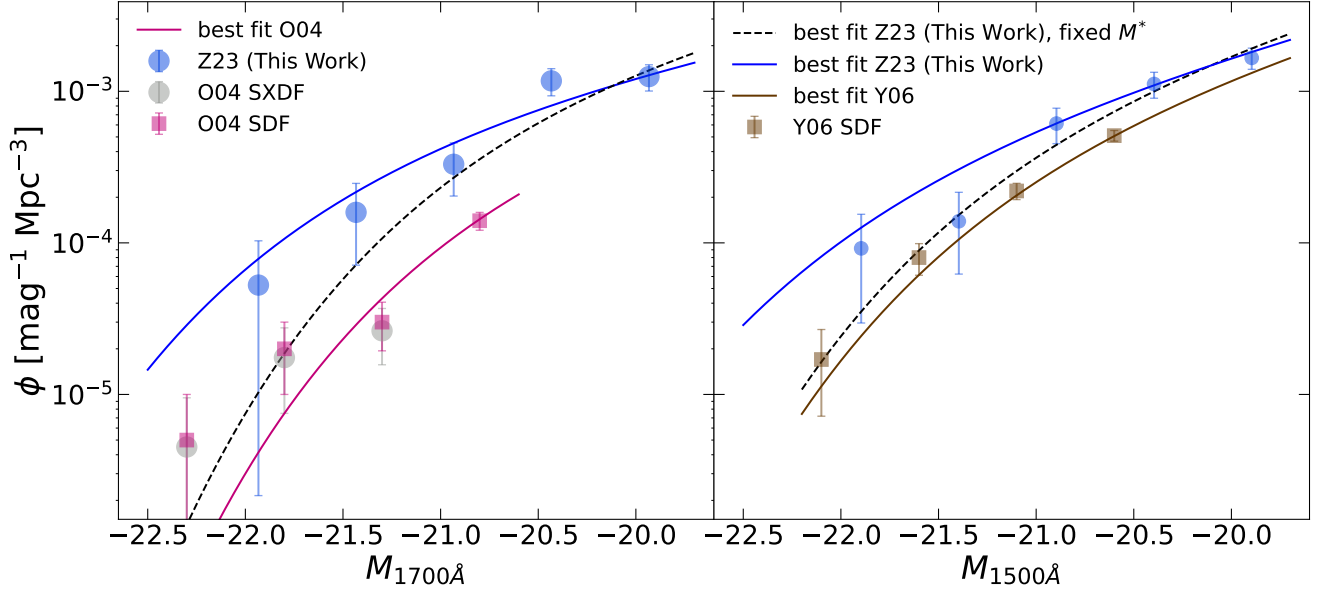


FIGURE 3.11: UV luminosity functions of the LBGs at $z \sim 4.6$. The blue circles are selected LBG candidates around the Hot DOGs. The magenta and brown rectangles are from O04 and Y06, respectively. The solids line shows the best-fit Schechter function for each study and the black dashed lines show the best fit by fixing the $M_*$ and $\alpha$ based on the result of O04 and Y06.

$$\phi(m) = \frac{1}{V_{\text{eff}}\Delta m} \sum_j \frac{1}{\rho(m_i)}, \qquad (3.6)$$

where $\rho(m_i)$ is the detection completeness based on the $i$-band magnitude of each source j (see Section 3.2.3). Figure 3.11 shows the estimated luminosity functions.

We fit the luminosity function using a Schechter (1976) function, namely,

$$\phi(M_{\mathrm{UV}})dM_{\mathrm{UV}} = (0.4 \ln 10) \, \phi^* \left(10^{0.4(M_{\mathrm{UV}}^* - M_{\mathrm{UV}})}\right)^{\alpha+1}$$
$$\exp\left(-10^{0.4(M_{\mathrm{UV}}^* - M_{\mathrm{UV}})}\right) dM_{\mathrm{UV}}, \quad (3.7)$$

where $M_{\mathrm{UV}}^*$ is the characteristic magnitude, $\phi^*(h_{70}^3 Mpc^{-3})$ is the normalization that provides the number density and $\alpha$ is the slope of the luminosity function at the faint end.

As can be seen in Fig. 3.11 the luminosity function of the LBG candidates around W2246−0526 has significantly larger space density than in the SDF studies of O04 and Y06, as expected given our results based on the number densities (see Fig. 3.9). The best-fit parameters of the luminosity function are shown in Table 3.2, for the modified O04 and Y06 selection functions.

TABLE 3.2: Parameters of the Luminosity Function calculated in this work, using the modified O04 and Y06 criteria for selecting LBG candidates.

| | O04 | | | Y06 | |
|---|---|---|---|---|---|
| $\phi^*(h_{70}^3 Mpc^{-3})$ | $M_{1700}^*(mag)$ | $\alpha$ | $\phi^*(h_{70}^3 Mpc^{-3})$ | $M_{1500}^*(mag)$ | $\alpha$ |
| $2.487 \times 10^{-3}$ | $-20.3^\dagger$ | $-1.6^\dagger$ | $1.78 \times 10^{-3}$ | $-20.72^\ddagger$ | $-1.82^\ddagger$ |
| $9.557 \times 10^{-4}$ | $-21.18 \pm 0.70$ | $-1.6^\dagger$ | $7.029 \times 10^{-4}$ | $-21.55 \pm 0.44$ | $-1.82^\ddagger$ |

$\dagger$: Value fixed to that used by O04.
$\ddagger$: Value fixed to that used by Y06.

## 3.4 Discussion

### 3.4.1 Overdensities around Hot DOGs

In Section 3.3.3, we showed that LBGs are more abundant by a factor of $\sim 6$ around W2246−0526 than in a blank field, leading to the conclusion that W2246−0526 lives in a dense region at a time when

the Universe was 1.3 Gyr old. This result is qualitatively consistent with the conclusions of other studies. In particular, Assef et al. (2015) studied the environment of a large number of Hot DOGs using *Spitzer*/IRAC imaging. Based on the number counts of red galaxies within $1'$ of the Hot DOGs, Assef et al. (2015) found that, statistically, these objects live in dense environments, comparable to those of radio-loud AGN found by Wylezalek et al. (2013). Similarly, Jones et al. (2014, 2017) concluded that Hot DOGs live in overdense environments based on the excess of companions detected at submillimeter wavelengths with JCMT/SCUBA-2.

More directly, Díaz-Santos et al. (2016, 2018) studied W2246$-$0526 using deep ALMA observations. They found three spectroscopically confirmed companions joined by dusty streamers within $\sim$35 kpc of W2246$-$0526. Additionally, they found 4 more continuum sources in a $\sim 20''$ field of view that may correspond to further companions. Díaz-Santos et al. (2018) argue that this Hot DOG is at the center of a triple merger and speculate its environment may become a massive cluster at $z = 0$ with the Hot DOG as the BCG. However, we do not find a strong indication that the Hot DOG is at the center of the overdensity. This may be because a) the overdensity, most likely a proto-cluster, is in a very early stage of collapse and is far from being virialized; b) this Hot DOG is not the most massive, central galaxy of the structure, even if it is the most luminous and radiating well above its Eddington limit (Tsai et al., 2018); or c) the Hot DOG may be luminous enough to affect the IGM transparency around it, effectively erasing the LBG overdensity's radial pattern. We notice that option b) appears unlikely given the lack of other bright sources in the field. However, JWST observations probing the peak of stellar emission are needed to confirm this. We note that possibility

c) is consistent with the fact that the spectroscopically confirmed companions of W2246−0526, as well as W2246−0526 itself, are not identified as LBG candidates. The potential consequence of the Hot DOG's feedback on the IGM is that we may be underestimating the number of companions in the vicinity of W2246-0526.

Recently, Ginolfi et al. (2022) studied the environment of W0410-0913, a Hot DOG at z = 3.631, using VLT/MUSE observations, and also concluded that this Hot DOG lives in a dense environment. Specifically, they found the number density of Ly$\alpha$ emitters within 0.4 Mpc of W0410-0913 to be $14^{+16}_{-8}$ times that of field galaxies with comparable Ly$\alpha$ luminosity. Also recently, Luo et al. (2022) studied the environment of W1835+4355 at $z = 2.3$ and found a factor of two enhancement in the number of DRGs in its surroundings. The overdensity differences between these studies may be indicative of the diversity of the environments around Hot DOGs, but may also be driven by the specific selection methods used in each study. Cosmological simulations show that the presence of early SMBHs with masses of $\sim 10^9 M_\odot$ at $z \geq 6$ is typically associated with galaxy overdensities, although the number of galaxies involved can vary (e.g., Costa et al., 2014, Habouzit et al., 2019). Habouzit et al. (2019) conducted a study using the Horizon AGN simulations, which focus on a wide range of galaxy and black hole properties, as well as the potential overdensity of the regions. They predict a wide variety of both obscured and unobscured quasar environments that are not driven by cosmic variance. While the use of photometric selection presents challenges due to cosmic variance, the inclusion of a large sample and the consideration of spectroscopic confirmation has the potential to provide additional insights (Champagne et al., 2023, Wang et al., 2023). Despite using a photometric selection and focusing on

a single Hot DOG environment, the observed level of overdensity of LBG candidates around the Hot DOG could potentially represent a lower limit if spectroscopically confirmed.

### 3.4.2 Comparisons of overdensities around other luminous sources

Studies based on a number of different techniques and wavelengths show that dense environments are not a unique property of Hot DOGs, but are shared by different types of luminous quasars, consistent with the evolutionary picture recently proposed by Assef et al. (2022) in which Hot DOGs correspond to a phase in the life of luminous quasars. Figure 3.12 shows a compilation of overdensities measured in quasar studies, which we detail below.
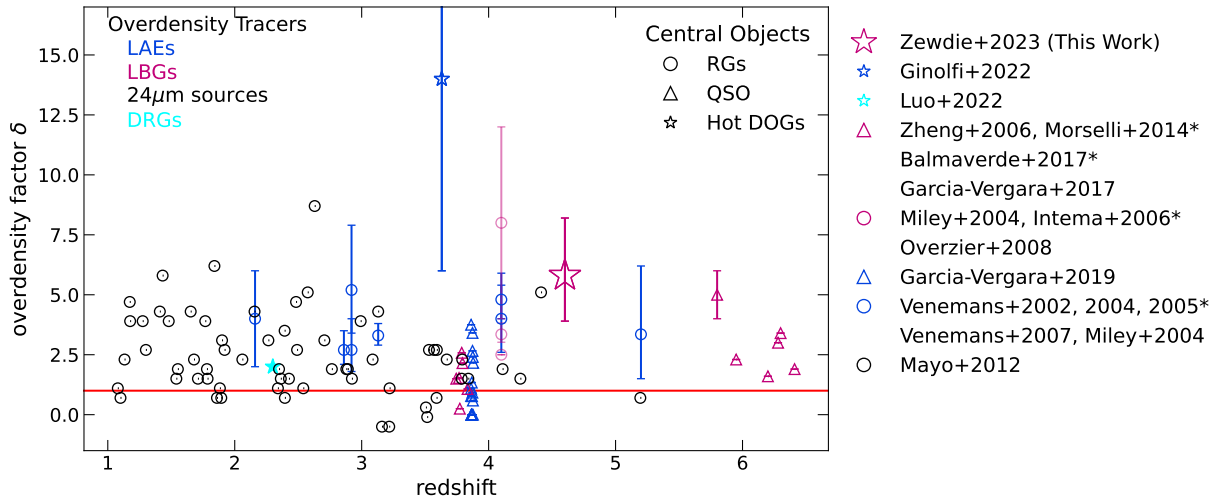


FIGURE 3.12: Overdensity around high redshift radio galaxies, quasars, and Hot DOGs as a function of redshift. We highlight the studies based on LBGs around quasars (magenta triangles, Morselli et al., 2014, Zheng et al., 2006, García-Vergara et al., 2017, Balmaverde et al., 2017), around radio galaxies (magenta circles, Miley et al., 2004, Intema et al., 2006, Overzier et al., 2008) and Hot DOGs (magenta star, this work), those based on LAEs around quasars (blue triangles, García-Vergara et al., 2019), radio galaxies (blue circles, Venemans et al., 2007, Miley et al., 2004, Venemans et al., 2002, 2004, 2005), and Hot DOGs (blue star, Ginolfi et al., 2022) and a study based on DRGs around Hot DOGs (cyan star, Luo et al., 2022). Overdensities of $24\mu m$ sources around high redshift radio galaxies are also shown (grey dot, Mayo et al., 2012). The red solid horizontal line indicates no overdensity.
∗: These studies defined the overdensity instead as $\delta = N_{found}/N_{expected} - 1$. We transformed these estimates to reflect our definition of $\delta$ before adding them to the Figure.

### 3.4.2.1    LBGs around quasars and radio galaxies

García-Vergara et al. (2017) studied LBGs around six quasars at $z \sim 4$ using VLT/FORS narrow band imaging and found a strong LBG clustering with an overall overdensity of $\delta = 1.5$. Morselli et al. (2014) also studied the overdensities of LBGs around four luminous z$\sim$6 quasars and found a significant galaxy overdensity of $\delta = 2.35$. This finding is also supported by Balmaverde et al. (2017) and Mignoli et al. (2020), who obtained a similar result. Utsumi et al. (2010) and Overzier et al. (2006) independently investigated LBGs around quasars and found overdensities that exceeded the 99% confidence level. Miley et al. (2004) studied the overdensity of LBGs around a radio galaxy at redshift $z = 4.1$ and found the environment to be 2.5 times denser than the field. Furthermore, when they restricted the inspected area to a 1 Mpc radius, they found that the field of the radio galaxy exhibited an overdensity five times higher than the average blank field, which is a comparable result to our findings in similarly sized **regions**. Intema et al. (2006) conducted a study on the overdensity of LBGs in the vicinity of a radio galaxy and reported an overdensity of $\delta=7\pm4$. Similarly, Overzier et al. (2008) studied the overdensity of LBGs and LAEs around a radio galaxy and found an average overdensity of $\delta = 3.53^{+0.47}_{-0.33}$. In addition, Ota et al. (2018) found high-density excess clumps of LBGs around quasars at $z = 6.61$, and Kashino et al. (2023) and Matthee et al. (2023) conducted spectroscopic analysis and verified the existence of an overdensity of [OIII] emission surrounding the most luminous quasar at $z > 6$.

### 3.4.2.2 LAEs around quasars and radio galaxies

García-Vergara et al. (2019) probed the overdensity of Ly$\alpha$ emitters around 17 quasars at $z \sim 4$ using the VLT/FORS2 narrow band imaging and observed clustering with an average overdensity of $\delta = 1.4 \pm 0.4$ although they note that 10 of the 17 targets have nominally underdense environments. They highlight the large cosmic variance inherent in quasar environments, with overdensities ranging from 0.0 to 3.75. Venemans et al. (2002) studied the environment of radio galaxies and found that the number density of Ly$\alpha$ emitters is $\delta = 4 \pm 1.4$. They also evaluated the overdensity by taking into account the detected FWHM of the velocity distribution, which is four times smaller than the FWHM of the filter width, and revealed this radio galaxy field is 15 times denser than a blank field in Ly$\alpha$ emitters. Venemans et al. (2004) also found an overdensity of Ly$\alpha$ emitters of $\delta = 3.35^{+2.85}_{-1.85}$ around radio galaxy at z=5.2.

### 3.4.2.3 Mid-Infrared sources around radio galaxies

Mayo et al. (2012) studied overdensities of 24 $\mu$m sources around 63 high redshift radio galaxies between redshift $z = 1 - 5.2$ using the using the Multiband Imaging Photometer for *Spitzer* (MIPS) and found an average overdensity of $2.2 \pm 1.2$ compared to the *Spitzer* Wide-area InfraRed Extragalactic Survey (SWIRE) fields. In this large sample of high redshift radio galaxies, they confirmed 11 protocluster candidates and identified 9 new. The selected protocluster candidates have an overdensity ranging from 3.1 to 8.7. Note that, in particular, Mayo et al. (2012) found a protocluster candidate of a high redshift radio galaxy with an overdensity of $\delta$=5.1 at z=4.413.

Wylezalek et al. (2013) studied the environment of obscured and un-obscured radio-loud AGNs at $1.3 < z < 3.2$ and found that 92% of radio-loud AGNs are overdense, however, they did not quantify the overdensities using the delta parameter. As can be seen in Fig. 3.12, Hot DOGs sit toward the upper range of the diversity of environments around other types of luminous quasars, but mostly within it. This is consistent with Hot DOGs being one of the phases in the evolution of luminous quasars, as while the AGN properties are widely different between them, they live in qualitatively similar regions of the Universe.

## 3.5    Conclusions

We present GMOS-S deep imaging observations of the Hot DOG, $W2246-0526$ in the $r$-, $i$-, and $z$-bands, and we use them to identify potential LBG companions and characterize the density of its environment. We use the O04 and Y06 color selection criteria to identify LBG candidates, modified to account for the differences between the GMOS-S and Suprime-cam bands, using the Shapley et al. (2003) LBG composite modified to include the additional IGM absorption expected at $z = 4.601$. Figure 3.5 shows that both modified criteria can successfully isolate LBG candidates from foreground objects and brown dwarf stars (see Section 3.3.1 and Fig. 3.4). Using the modified O04 and Y06 color selection, we found 37 and 55 LBG candidates ($r$-dropouts), respectively, in an area of 23.7 arcmin$^2$ centered on $W2246-0526$. We find the following main results:

1. $W2246-0526$ lives in a dense environment as compared with the mean density of the Universe. Specifically, matching to $z$-band

magnitude depth of O04 and Y06 studies, this corresponds to $\delta = 5.8^{+2.4}_{-1.9}$ times the surface density of LBGs expected in the field

2. Figure 3.6 shows that, in order to be selected, companion LBGs may need a combination of mild dust obscuration and excess IGM absorption over the typical expected amount. This suggests that we might be missing many potential companions to W2246−0526. In fact, we find that the O04 selection does not identify either of the known, resolvable companions found by Díaz-Santos et al. (2016, 2018), and the Y06 selection identifies only one of them.

3. We estimated the UV luminosity function of the selected LBG candidates around W2246−0526 in both modified selection criteria and found the presence of the LBG candidates in significantly higher space densities than in the studies of O04 and Y06, consistent with our findings based on the number densities.

4. We studied the density of LBG candidates as a function of distance from the Hot DOG, counting them in rings of 20 arcsec widths starting 2 arcsec away from W2246−0526. We did not observe a clear radial profile centered on the Hot DOG. While W2246−0526 lives in an overdense environment, the overdensity is not clearly concentrated around the Hot DOG. This may be because a) the overdensity is in an early stage of collapse and has not yet virialized; b) although this Hot DOG is the most luminous object in the structure and radiates well above the Eddington limit, it is not the most massive or central galaxy in the structure; or c) the intense radiation emitted by the Hot

DOG may affect the IGM transparency around it, deleting the radial pattern in the LBG overdensity.

5. The W2246−0526 overdense environment is qualitatively consistent with statistical studies of `Spitzer`/IRAC and submillimeter companions to Hot DOGs (Assef et al., 2015, Jones et al., 2014, Fan et al., 2017) and with recent observational studies of the environment around the Hot DOGs W0410 at z=3.6 (Ginolfi et al., 2022) and W1835 at z=2.35 (Luo et al., 2022).

6. Compared with radio galaxies and rest-frame UV bright quasars at a similar redshift, Hot DOGs live in somewhat denser environments (see Fig. 3.12).

The high overdensities identified for W2246-0526 and other Hot DOGs suggest that these objects might be good tracers of dense regions like proto-clusters at high redshift. Further studies of their environments, particularly at different redshifts and luminosities, and considering different ways of selecting the potential nearby counterparts, will push forward our understanding of SMBHs, galaxies, and large structure formation and evolution.

## Acknowledgements

# A. LBG Candidates

The coordinates and magnitudes of all LBG candidates that were selected based on the modified O04 and Y06 criteria are shown in Table 3.3. Those selected solely by the Y06 criteria are shown in Table 3.4. We also list the previously detected sources by Díaz-Santos et al. (2016) and Díaz-Santos et al. (2018) in Table 3.5. Stamps of 8″ x 8″ are shown in Figs. 3.13 and 3.14 for all LBG candidates. The stretch in the stamps of all bands is linear and normalized to the $i$-band flux of each source. We also show the stamps of the detected sources by Díaz-Santos et al. (2016) and Díaz-Santos et al. (2018) using the deep ALMA observations and stamps of W2246-0526 in Fig. 3.15.

TABLE 3.3: The list of selected LBG candidates in order of $i$-band magnitude from brightest to faintest using the modified selection criteria of O04 and Y06, the magnitudes are measured in 2'' apertures.

| LBG candidates | Ra | Dec | r'mag | r'magerr | i'mag | i'magerr | z'mag | z'magerr |
|---|---|---|---|---|---|---|---|---|
| LBGC1 | 341.5000812 | -5.4621209 | 25.91 | 0.06 | 24.40 | 0.02 | 24.21 | 0.04 |
| LBGC2 | 341.5238785 | -5.4738352 | 26.62 | 0.11 | 24.98 | 0.04 | 24.95 | 0.08 |
| LBGC3 | 341.5634960 | -5.4611731 | 26.93 | 0.15 | 25.07 | 0.05 | 24.60 | 0.05 |
| LBGC4 | 341.5406383 | -5.4077323 | 26.98 | 0.16 | 25.18 | 0.06 | 25.55 | 0.14 |
| LBGC5 | 341.5674046 | -5.4257313 | 26.93 | 0.15 | 25.45 | 0.07 | 25.33 | 0.11 |
| LBGC6 | 341.5546196 | -5.4564413 | 27.22 | 0.20 | 25.51 | 0.08 | 25.84 | 0.18 |
| LBGC7 | 341.5676332 | -5.4255572 | 26.99 | 0.16 | 25.54 | 0.08 | 25.92 | 0.19 |
| LBGC8 | 341.5167494 | -5.4631821 | 27.74 | 0.32 | 25.55 | 0.08 | 24.91 | 0.07 |
| LBGC9 | 341.5434564 | -5.4698341 | 27.06 | 0.17 | 25.61 | 0.09 | 25.47 | 0.13 |
| LBGC10 | 341.5683588 | -5.4263881 | 28.22 | 0.51 | 25.64 | 0.09 | 25.39 | 0.12 |
| LBGC11 | 341.4862233 | -5.4518122 | 27.37 | 0.23 | 25.72 | 0.09 | 25.55 | 0.13 |
| LBGC12 | 341.4896542 | -5.4596500 | 27.46 | 0.25 | 25.86 | 0.11 | 25.71 | 0.16 |
| LBGC13 | 341.5260347 | -5.4651164 | 27.48 | 0.25 | 25.88 | 0.11 | 25.66 | 0.15 |
| LBGC14 | 341.5436721 | -5.4741600 | 27.53 | 0.27 | 25.95 | 0.12 | 26.52 | 0.34 |
| LBGC15 | 341.5239417 | -5.4254533 | 28.58 | 0.71 | 26.01 | 0.12 | 26.01 | 0.21 |
| LBGC16 | 341.5683885 | -5.4150181 | ¿29.0 | ... | 26.01 | 0.12 | 25.73 | 0.16 |
| LBGC17 | 341.4860620 | -5.4519042 | 28.53 | 0.68 | 26.03 | 0.13 | 25.56 | 0.14 |
| LBGC18 | 341.5175633 | -5.3935374 | 28.14 | 0.47 | 26.09 | 0.13 | 25.98 | 0.20 |
| LBGC19 | 341.5725185 | -5.4205112 | 28.15 | 0.48 | 26.10 | 0.13 | 25.67 | 0.15 |
| LBGC20 | 341.5289983 | -5.4473865 | 27.79 | 0.34 | 26.16 | 0.14 | 26.40 | 0.30 |
| LBGC21 | 341.5316215 | -5.4170330 | 27.91 | 0.38 | 26.17 | 0.14 | 25.73 | 0.16 |
| LBGC22 | 341.4826847 | -5.4571690 | ¿29.0 | ... | 26.20 | 0.15 | 25.69 | 0.15 |
| LBGC23 | 341.5347913 | -5.4452524 | ¿29.0 | ... | 26.24 | 0.15 | 26.44 | 0.31 |
| LBGC24 | 341.5055473 | -5.4173291 | ¿29.0 | ... | 26.24 | 0.15 | 26.00 | 0.21 |
| LBGC25 | 341.5244762 | -5.4688419 | 27.76 | 0.33 | 26.30 | 0.16 | 26.38 | 0.30 |
| LBGC26 | 341.5619358 | -5.4686734 | 28.11 | 0.46 | 26.35 | 0.17 | 26.52 | 0.34 |
| LBGC27 | 341.5160667 | -5.4269681 | 27.95 | 0.40 | 26.36 | 0.17 | 26.06 | 0.22 |
| LBGC28 | 341.5059390 | -5.4178372 | ¿29.0 | ... | 26.41 | 0.18 | 26.53 | 0.34 |
| LBGC29 | 341.5148175 | -5.4221763 | ¿29.0 | ... | 26.41 | 0.18 | 26.28 | 0.27 |
| LBGC30 | 341.5530543 | -5.4439086 | 28.37 | 0.58 | 26.44 | 0.19 | 25.94 | 0.20 |
| LBGC31 | 341.5428250 | -5.4423416 | ¿29.0 | ... | 26.48 | 0.19 | 25.86 | 0.18 |
| LBGC32 | 341.5230371 | -5.4030845 | 28.54 | 0.69 | 26.59 | 0.21 | 26.04 | 0.21 |
| LBGC33 | 341.5228025 | -5.4275428 | 28.48 | 0.65 | 26.63 | 0.22 | 26.21 | 0.25 |
| LBGC34 | 341.5267696 | -5.4423843 | 28.73 | 0.82 | 26.64 | 0.22 | 26.07 | 0.22 |
| LBGC35 | 341.5189382 | -5.4619869 | ¿29.0 | ... | 26.65 | 0.23 | 26.40 | 0.30 |
| LBGC36 | 341.4958418 | -5.4524641 | ¿29.0 | ... | 26.72 | 0.24 | 26.45 | 0.32 |
| LBGC37 | 341.5494098 | -5.4744106 | ¿29.0 | ... | 27.04 | 0.33 | 26.46 | 0.32 |

TABLE 3.4: The list of selected LBG candidates in order of *i*-band magnitude from brightest to faintest using the modified selection criteria of Y06

| LBG candidates | Ra | Dec | r´mag | r´magerr | i´mag | i´magerr | z´mag | z´magerr |
|---|---|---|---|---|---|---|---|---|
| LBGC38 | 341.5315566 | -5.4424653 | 25.84 | 0.05 | 24.48 | 0.03 | 24.43 | 0.05 |
| LBGC39 | 341.5348617 | -5.4496508 | 26.63 | 0.11 | 25.27 | 0.06 | 25.73 | 0.16 |
| LBGC40 | 341.5879426 | -5.4218498 | 26.69 | 0.12 | 25.27 | 0.06 | 25.32 | 0.11 |
| LBGC41 | 341.5128808 | -5.4353647 | 26.64 | 0.12 | 25.28 | 0.06 | 25.23 | 0.10 |
| LBGC42 | 341.5497232 | -5.4772553 | 26.62 | 0.11 | 25.28 | 0.06 | 25.33 | 0.11 |
| LBGC43 | 341.5290441 | -5.4836258 | 26.58 | 0.11 | 25.31 | 0.06 | 25.47 | 0.13 |
| LBGC44 | 341.5136125 | -5.4468992 | 26.76 | 0.13 | 25.35 | 0.07 | 25.54 | 0.13 |
| LBGC45 | 341.5174896 | -5.4302933 | 26.82 | 0.14 | 25.47 | 0.07 | 25.44 | 0.12 |
| LBGC46 | 341.5306453 | -5.4806720 | 26.77 | 0.13 | 25.49 | 0.07 | 26.27 | 0.27 |
| LBGC47 | 341.5376427 | -5.4820949 | 26.96 | 0.16 | 25.50 | 0.08 | 25.26 | 0.10 |
| LBGC48 | 341.5623409 | -5.4306788 | 26.94 | 0.15 | 25.68 | 0.09 | 25.80 | 0.17 |
| LBGC49 | 341.5373545 | -5.4108363 | 27.16 | 0.19 | 25.89 | 0.11 | 26.14 | 0.24 |
| LBGC50 | 341.5324556 | -5.4005839 | 27.44 | 0.24 | 26.16 | 0.14 | 26.44 | 0.31 |
| LBGC51 | 341.5418400 | -5.4629014 | 27.43 | 0.24 | 26.19 | 0.15 | 26.35 | 0.29 |
| LBGC52 | 341.5611256 | -5.4731423 | 27.65 | 0.30 | 26.22 | 0.15 | 26.40 | 0.30 |
| LBGC53 | 341.5673180 | -5.4646407 | 27.61 | 0.29 | 26.34 | 0.17 | 26.34 | 0.28 |
| LBGC54 | 341.5493831 | -5.4784556 | 27.85 | 0.36 | 26.46 | 0.19 | 26.34 | 0.29 |
| LBGC55 | 341.5210883 | -5.4012651 | 28.34 | 0.57 | 26.79 | 0.26 | 26.46 | 0.32 |

TABLE 3.5: Díaz-Santos et al. (2016) and Díaz-Santos et al. (2018) list of two spectroscopically confirmed and potential companions in order of *i*-band magnitude from brightest to faintest found through deep ALMA observations.

| LBG candidates | Ra | Dec | r'mag | r'magerr | i'mag | i'magerr | z'mag | z'magerr |
|---|---|---|---|---|---|---|---|---|
| U1 | 341.5319518 | -5.4427905 | 24.02 | 0.01 | 23.41 | 0.01 | 22.87 | 0.01 |
| C3 | 341.5315566 | -5.4424653 | 25.84 | 0.05 | 24.48 | 0.03 | 24.43 | 0.05 |
| C2 | 341.5326256 | -5.4440949 | 25.51 | 0.04 | 24.67 | 0.03 | 24.52 | 0.05 |
| Knot | 341.5322715 | -5.4439102 | 25.13 | 0.03 | 24.92 | 0.04 | 24.58 | 0.05 |
| U3 | 341.5300995 | -5.4454121 | 25.77 | 0.05 | 25.42 | 0.07 | 24.58 | 0.09 |
| U2 | 341.5303579 | -5.4416845 | 26.64 | 0.11 | 25.59 | 0.08 | 25.52 | 0.13 |
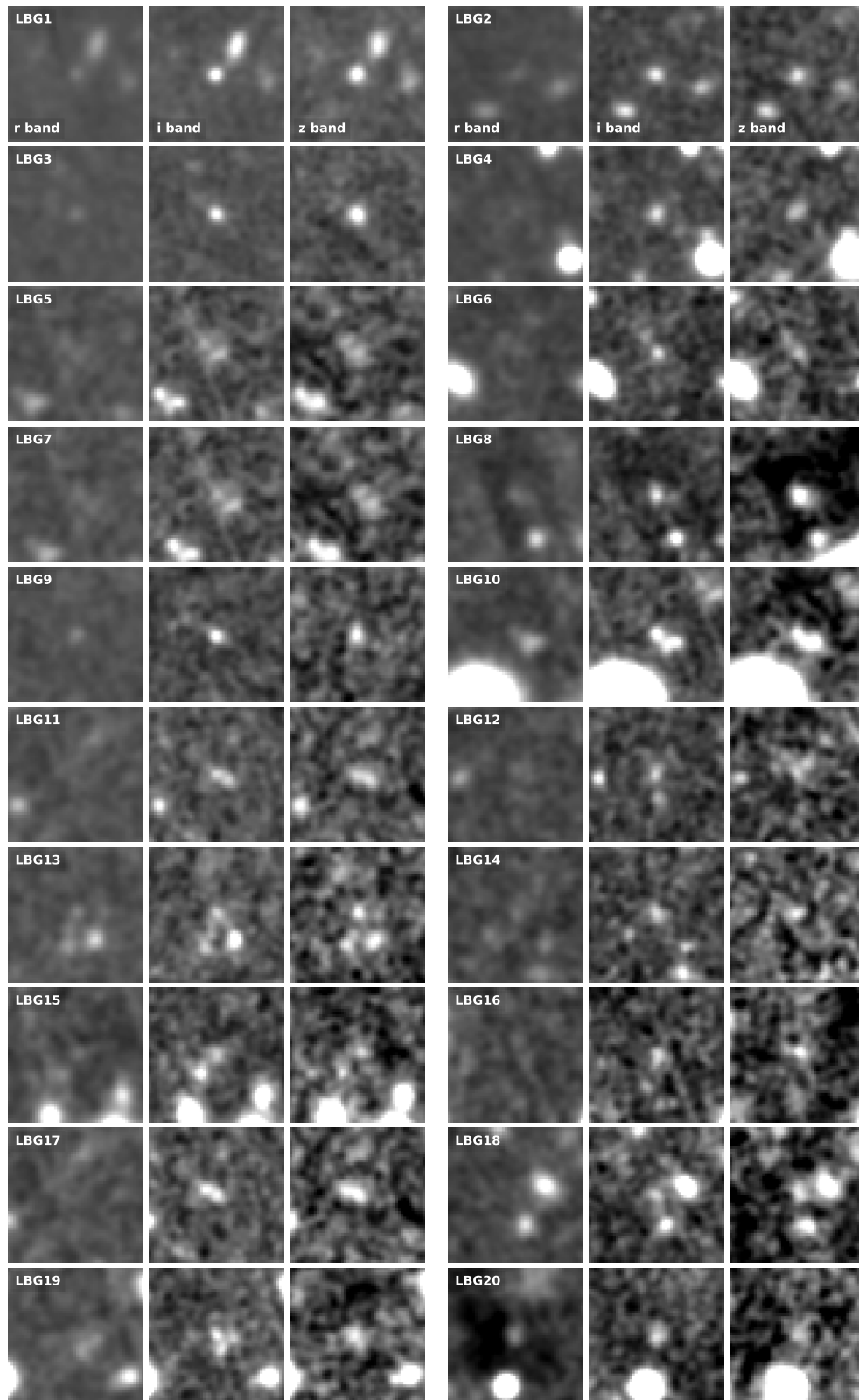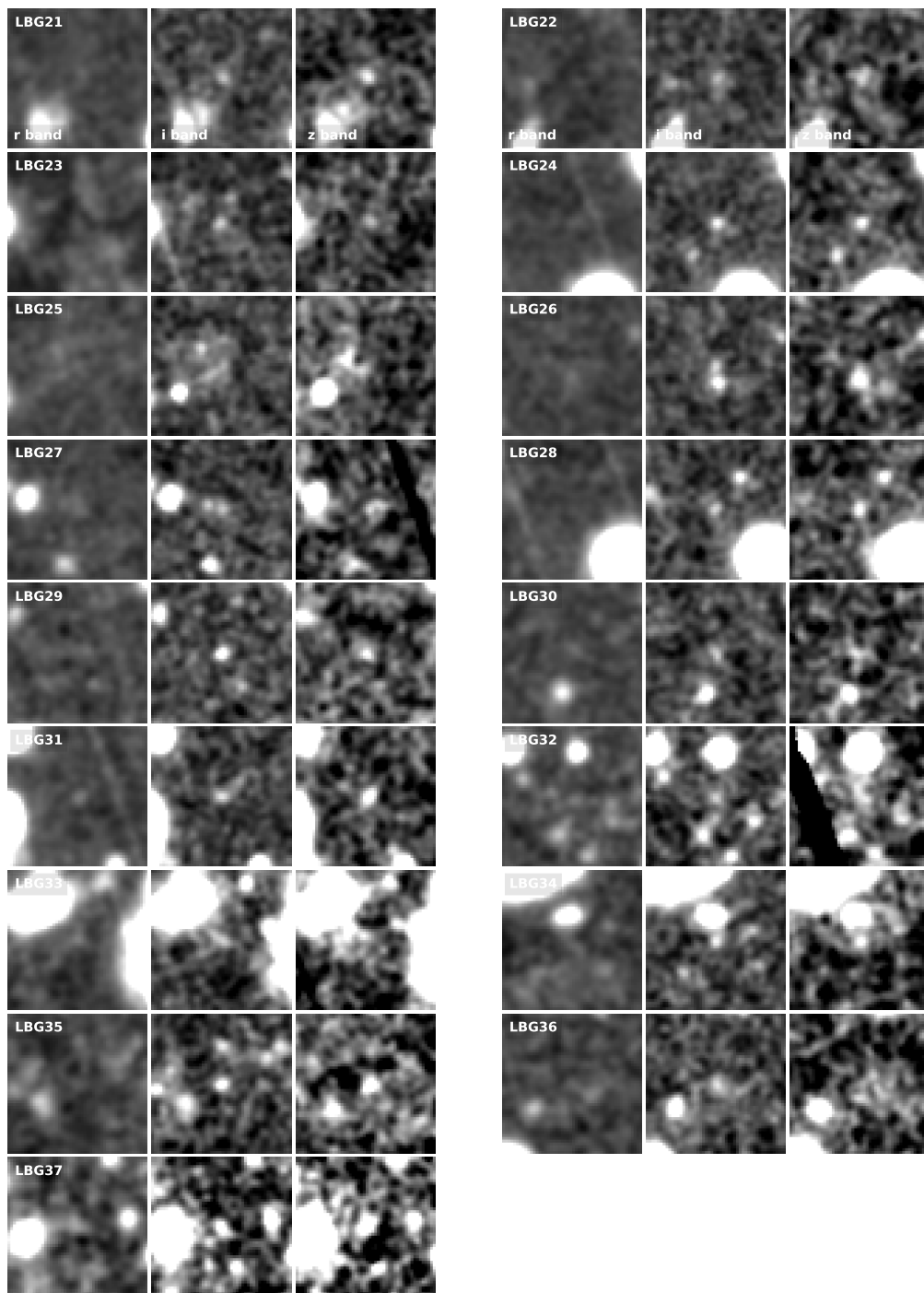
FIGURE 3.13: Postage stamps ($8''$ x $8''$) of the selected LBG candidates using the modified criteria of O04 and Y06 in each band.
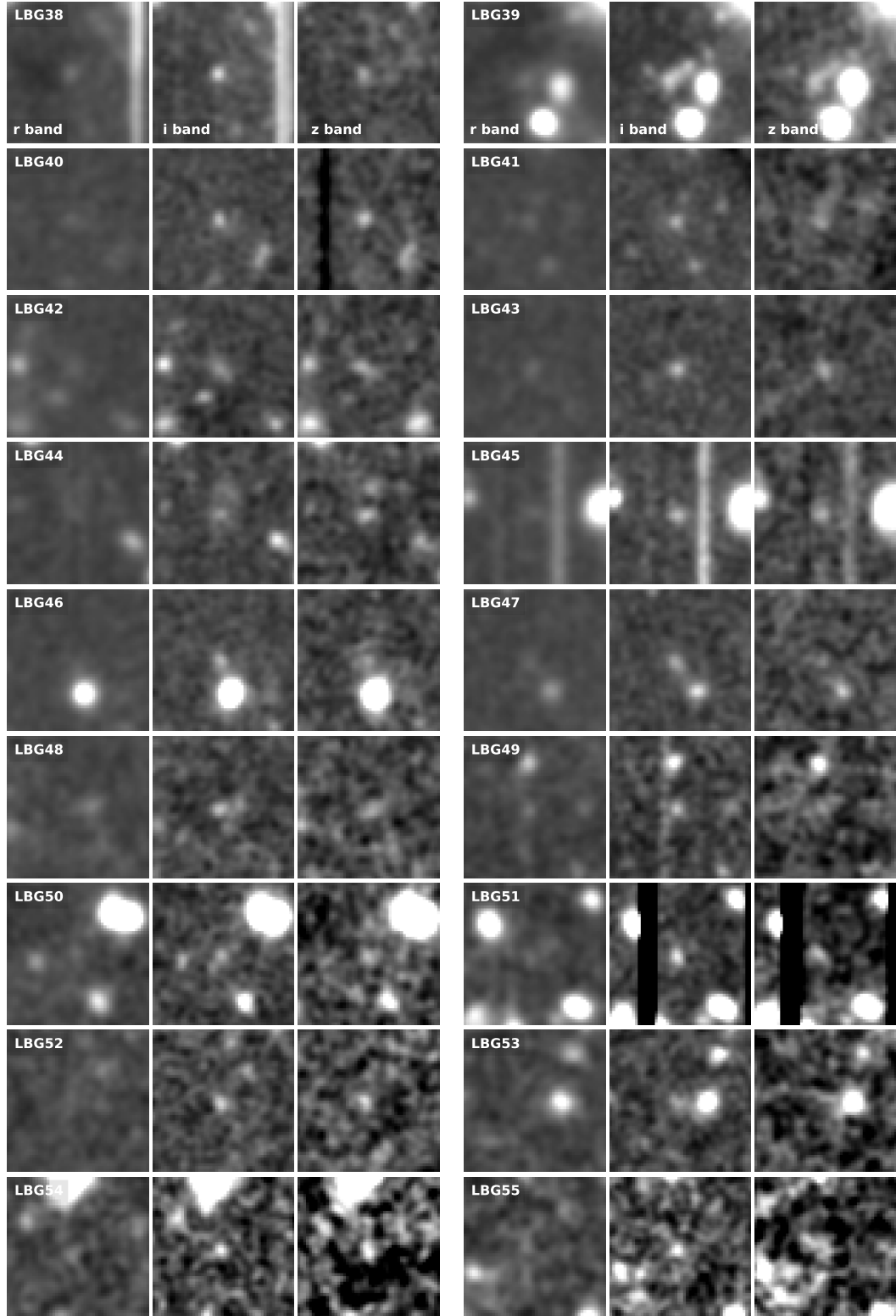
FIGURE 3.14: Postage stamps (8″ x 8″) of the 18 LBG candidates that were selected only by the modified criteria of Y06.
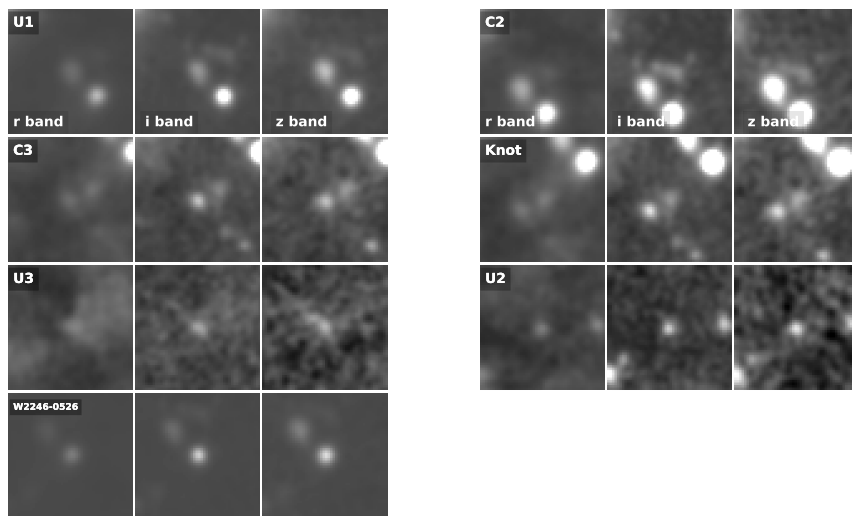
FIGURE 3.15: Postage stamps ($8''$ x $8''$) of the W2246–0526, 2 spectroscopically confirmed companions (C2 and C3) and 4 potential companions (U1, U2, U3, and knot) that were detected using deep ALMA observation by Díaz-Santos et al. (2016) and Díaz-Santos et al. (2018). All those companions with W2246–0526 are shown in Fig. 3.7

# Chapter 4

# The Environment of Hot Dust Obscured Galaxies

*Zewdie et al., (2023b, in prep)*

We present the identified Lyman Break Galaxy (LBG) candidates in the vicinity of three hyper-luminous Hot Dust-Obscured Galaxies (Hot DOGs): W0410–0913 at z=3.631, W0813+0140 at $z = 3.912$, and W2246–0526 at $z = 4.601$. The work are based on the data already presented in Zewdie et al. (2023), but reanalized in a manner consistent with that of the other Hot DOG fields. We used deep Magellan/IMACS imaging in the $g$-, $r$,- and i-bands for the fields of the first two targets. We optimized the photometric selection criteria using the COSMOS2020 catalog. When comparing the density of LBG candidates with the COSMOS2020 blank field, we find an overdensity of sources around each Hot DOG. Our analysis revealed that the overdensity of the two Hot DOGs observed with IMACS, W0410–0913 and W0813+0140, shows a steep decline at distances greater than $250''$. The smaller field of view of GMOS precludes us from confirming this for W2246–0526. This radial density profile may indicate the broader structure of the cosmic environment. Our

results strongly suggest that Hot DOGs are an excellent tracer of protoclusters.

## 4.1   Introduction

The formation and growth of massive galaxies in the early universe occurs through hierarchical merging (e.g., Bower et al., 2006, Collins et al., 2009), wherein smaller galaxies merge over time to form massive galaxy and/or a larger-scale structures (Kauffmann et al., 1999). The hierarchical merging of galaxies implies that the environment in which galaxies are born and live can play a fundamental role in driving their evolution. This merging process is thought to be driven by the gravitational interactions between galaxies, as well as the accretion of material onto supermassive black holes (SMBHs) at their centers. SMBHs grow the majority of their mass through mergers and through gas accretion during Active Galactic Nuclei (AGN) phases. The existence of SMBHs in the early universe (e.g., Mazzucchelli et al., 2017, ?) and the amounts of gas needed to fuel the rapid growth necessary to create these $10^9 M_\odot$ SMBHs require these objects to live in the densest regions of the Universe. Some observational studies show the existence of an overdensity around high-redshift radio galaxies ($1 < z < 5$; e.g., Miley et al., 2004, Intema et al., 2006, Venemans et al., 2002, Mayo et al., 2012), high-redshift quasars ($z \gtrsim 4$; e.g., Morselli et al., 2014, Zheng et al., 2006, García-Vergara et al., 2017, Balmaverde et al., 2017), confirming these expectations. These overdense environments also provide a unique opportunity to understand the formation of large-scale structures such as protoclusters.

Spanning over two decades, the exploration of overdensities around luminous high-redshift quasars and radio galaxies has notably deepened our comprehension of the environment surrounding extremely luminous, high-redshift obscured quasars throughout cosmic time. Identifying most companion galaxies spectroscopically to these quasars and radio galaxies is difficult due to their inherent faintness, so various methods based purely on photometric observations have been devised to trace overdense regions around luminous quasars or radio galaxies. These include the selection of Lyman-Break Galaxies (LBGs; e.g., Ouchi et al., 2004, Yoshida et al., 2006, Morselli et al., 2014, Husband et al., 2013, García-Vergara et al., 2017, Steidel et al., 2003) through broad-band optical colors or Lyman alpha emitters (LAEs; e.g., Kashikawa et al., 2007, García-Vergara et al., 2019) via narrow-band observations.

Hot Dust-Obscured Galaxies (Hot DOGs; Eisenhardt et al., 2012, Wu et al., 2012), discovered through the Wide-field Infrared Survey Explorer (WISE; Wright et al., 2010) mission, are some of the most luminous and rare population of obscured quasars. These objects are heavily obscured by dust and are powered by intense accretion onto SMBHs, buried under enormous amounts of gas and dust. They are strongly detected at 12 and 22 ¯m WISE bands while appearing faint or undetected in the 3.4 and 4.6 ¯m ones. The extreme bolometric luminosities of Hot DOGs, with $L_{bol} > 10^{13}L_{\odot}$, with some exceeding $L_{bol} > 10^{14}L_{\odot}$ (Tsai et al., 2015). These objects play a significant role in influencing their host galaxies by inducing substantial gas outflows (Díaz-Santos et al., 2016, Finnerty et al., 2020, Jun et al., 2020).

Numerous studies have been conducted using multiwavelength observations to comprehend the characteristics of the environments surrounding Hot DOGs. Previous studies regarding the environments of Hot DOGs have suggested that they might inhabit densely populated regions (Assef et al., 2015, Jones et al., 2014, 2017, Fan et al., 2017). In particular, Assef et al. (2015) studied a large number of Hot DOGs through Spitzer/IRAC imaging and revealed that these objects statistically exist in dense environments similar to radio-loud AGN. Jones et al. (2014, 2017) explored the overdensities of submillimeter galaxies (SMGs) and mid-IR Spitzer-selected galaxies situated in proximity to Hot DOGs.Their findings suggest that Hot DOGs could potentially reside in overdense environments similar as the CARLA clusters (Assef et al., 2015, Wylezalek et al., 2013).

Recently, Ginolfi et al. (2022) studied the environment of W0410–0913, $z = 3.361$ through VLT/MUSE observations, found a significant overdensity $14^{+16}_{-8}$ of LAEs around it. Luo et al. (2022) found an overdensity, $\delta = 2$ of distant red galaxies around W1835+4355 at $z = 2.3$ using near-infrared observations conducted with the wide-field infrared camera on the Palomar 200-inch telescope. Recently, Zewdie et al. (2023) studied the environment of the most luminous known Hot DOG, W2246–0526 at $z = 4.601$, using deep GMOS-S imaging in the r, i, and z bands and revealed an overdensity $\delta = 6$ of LBGs around this Hot DOG within a scale of 1.4 Mpc. However, they did not observe a radial profile overdensity of LBGs around it. They suggested that the overdensity, likely a proto-cluster in early collapse, lacks a clear central positioning for the Hot DOG. This Hot DOG, despite being hyper-luminous and radiating beyond its Eddington limit, $\lambda_{Edd}$=2.8 (Tsai et al., 2018), might not constitute the most massive or central galaxy. Alternatively, its luminosity could

affect intergalactic transparency, potentially leading to the alteration of the LBG pattern. Deep ALMA observations, Díaz-Santos et al. (2016, 2018) revealed the presence of companions around W2246–0526 linked by dust-streams to the Hot DOG, extending to 30 kpc. They suggested a triple merger, which signifies ongoing merging and a locally dense environment. These studies suggest that Hot DOGs reside in and underscore their potential as indicators for investigating, dense regions at high redshifts, where processes of galaxy formation and evolution processes are enhanced.

In this work, we study the environment of three Hot DOGs: W0410–0913, W0831+0140, and W2246–0526, by surveying their LBG companions. Specifically, we investigate LBG candidates at redshifts $z \sim 3.631$ and $z \sim 3.912$, selected as g-dropouts in the Inamori-Magellan Areal Camera and Spectrograph (IMACS), and we used the data from Zewdie et al. (2023), who studied the selection as r-band dropouts at $z \sim 4.601$ in deep Gemini Multi-Object Spectrographs South (GMOS-S) imaging. We use optimized selection functions based on the observations, redshifts and classifications of the Cosmic Evolution Survey (COSMOS; Scoville et al., 2007) catalog. The Chapter is organized as follows: In Section 4.2, we discuss the observations from IMACS, data reduction, photometric measurement, and the COSMOS catalog. In Section 4.3, we discuss the optimization of the selection function based on the color selection criteria and we discuss the study of the color and spatial distribution of the LBG candidates. In Section 4.4, we compare our results with other Hot DOG and quasar environments presented in the literature. Our conclusions are presented in Section 4.5. Throughout this Chapter, all magnitudes are given in the AB system. We assume a flat $\Lambda$CDM cosmology with $H_0 = 70 \mathrm{kms}^{-1}\mathrm{Mpc}^{-1}$ and $\Omega_M = 0.3$. At a redshift

of $z = 3.631$, W0410–0913 is observed at 1.696 billion years after the Big Bang, and an observed spatial scale of $1''$ is equal to 7.222 kpc. Similarly, at a redshift of $z = 3.912$, W0831+0140 is observed at 1.554 billion years after the Big Bang, with an observed spatial scale of $1''$ being equal to 7.014 kpc.

## 4.2    Observation and data reduction

### 4.2.1    Magellan/IMACS Observations

We used the IMACS instrument at the Magellan Baade telescope to obtain deep images in the $g$-, $r$-, and $i$-bands of the fields around W0410–0913 at z=3.621 and W0813+0140 at z=3.912 on the night of UT2019-11-25 (Program: PI R.J. Assef). The average seeing was $1.02''$, $1.07''$, and $1.08''$ for the W0410–0913 observations in the $g$-, $r$-, and $i$-bands, respectively, with airmass ranging 1.07 to 1.15. For the W0831+0140 observations, the $r$-band exhibited a better mean seeing of $0.81''$ compared to the $g$- and $i$-bands, which were $1.1''$ and $1.01''$, respectively, with the airmass ranging from 1.17 to 1.54. All images were obtained with a pixel scale of $0.22''$ pix$^{-1}$. The details of the observations are summarized in Table 4.1.

#### 4.2.1.1    IMACS data reduction

We reduced the IMACS observations by applying bias and flat field corrections using `Theli` (Schirmer, 2013). The raw IMACS images have no World Coordinate System (WCS) information, so we developed a simple `python` package[1] to calibrate the image astrometry. We first made an initial guess based on the telescope information in

---

[1] https://github.com/TrystanScottLambert/imacs_wcs

TABLE 4.1: Summary of IMACS observations information used in this work

| Hot DOGs | Band | Exposure Time | Mean Seeing | Mean Airmass | UT Dates | Depth of the Stack Image 5 $\sigma$ /3 $\sigma$ /1 $\sigma$ |
|---|---|---|---|---|---|---|
| | g | 21 × 200s 6 × 100s 1 × 83.202s | 1.02″ | 1.15 | 2019-11-25 | 26.69/27.24/28.42 |
| W0410−0913 | r | 21 × 100s | 1.07″ | 1.08 | 2019-11-25 | 25.84/26.39/27.53 |
| | i | 16 × 100s | 1.08 ″ | 1.07 | 2019-11-25 | 25.14/25.68/26.88 |
| | g | 15 × 200s 6 × 100s | 1.1″ | 1.30 | 2019-11-25 | 26.45/27.00/28.19 |
| W0813+0140 | r | 5 × 200s 6 × 100s 5 × 50s | 0.81″ | 1.17 | 2019-11-25 | 25.47/26.02/27.20 |
| | i | 5 × 200s 2 × 100s | 1.01 ″ | 1.54 | 2019-11-25 | 25.09/25.64/26.68 |
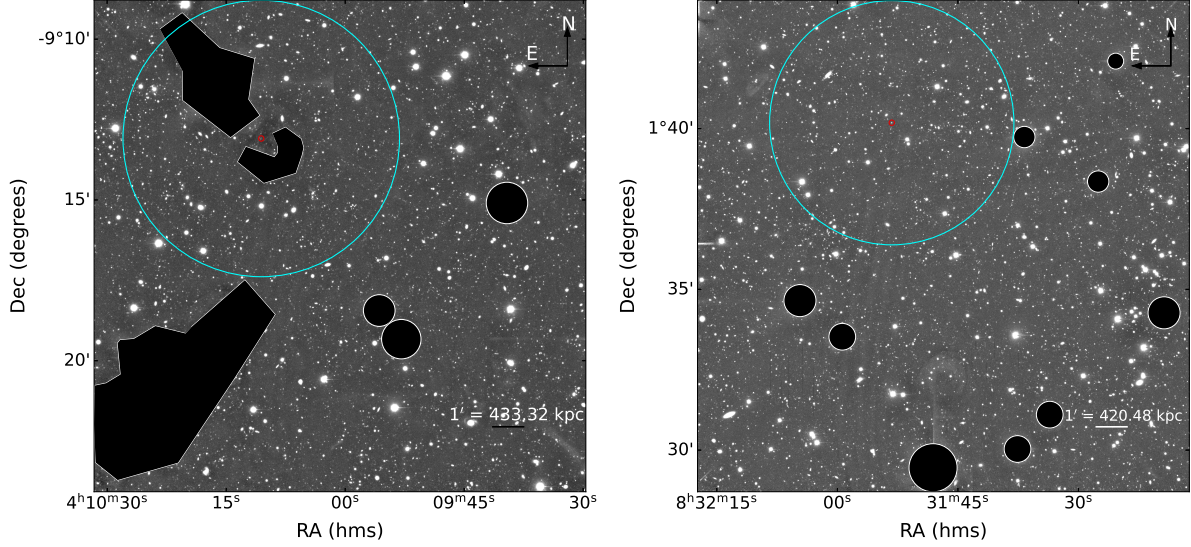
FIGURE 4.1: Left Panel: $r$-band image of W0410–0913. Black circles and polygons show the masked area that we did not use for our LBG selection (see Section 4.2.1.2 for details). The cyan circles indicates the area of the Hot DOG at the centered position, and the red circle represents the position of W0410–0913. Right Panel: $r$-band image of W0831+0140. Black circles show the masked area that we did not use for our selection. The cayn circles indicates the area of the Hot DOG at the centered position, and the red circle represents the position of W0831+0140.

the image headers. We then cross-match our sources with objects in Gaia DR3 (Gaia Collaboration et al., 2023) using the `astroquery` package. The pixel to world relation was then used to define an accurate wcs object for each image. We found that the initial guess was off by about $20''$. Finally, we used `Swarp`[2] to coadd our images.

There are a number of saturated stars, particularly in the field of W0410–0913, with large saturation spikes that cause irregular systematic features in the image, so we applied some conservative masking to avoid the detection of spurious sources. The final masked images are shown in Figure 1. We have estimated the usable area by generating $10^6$ randomly uniform points distributed throughout the image and counting the fraction of unmasked points. The usable area remaining after is $\sim 213$ arcmin$^2$ and $\sim 236$ arcmin$^2$, respectively for the W0410–0913 and W0831+0140 fields. As can be seen

---

[2]Swarp version 2.3 8

in Figure 4.1, our IMACS observation is not centered on the Hot DOGs. We repositioned the cropped-out positions of our targets to be at the center of the images. We trimmed them to an area of 8.5 by 8.5 arcmin$^2$ for W0410 and 7.5 by 7.5 arcmin$^2$ for W0831.

#### 4.2.1.2   Photometry

We carried out the photometry using fixed $2''$ diameter apertures with `SExtractor`[3] (Bertin and Arnouts, 1996) in dual-image mode, using the $r$-band image for source detection. Our approach involved applying a detection and analysis threshold requiring a minimum of 3 pixels detected above $1.5\sigma$. We applied a 5x5 convolution filter based on a Gaussian Point Spread Function (PSF) with a Full Width at Half Maximum (FWHM) of 3.0 pixels. For reference, the seeing in the r-band was 4.9 and 3.7 pixels respectively for W0410–0913 and W0831+0140. For the background, we used a global model with mesh and filter sizes of 32 and 3, respectively.

The photometric calibration was conducted using data from the Panoramic Survey Telescope & Rapid Response System (Pan-STARRS) Survey (Tonry et al., 2012). We exclusively considered point sources, which were selected based on the probabilistic classification of unresolved point sources with a `ps_score` greater than 0.83, following the suggestion by Tachibana and Miller (2018)[4]. The Pan-STARRS point sources were cross-matched with the sources from our imaging using a 1 arcsec radius and we found 346 and 414 matches within the unmasked areas of the W0410–0913 and W0831+0140 fields respectively. To avoid issues with saturation and non-linearity in the IMACS images and issues with low SNR detections in PanSTARRS,

---

[3]SExtractor version 2.28

[4]https://outerspace.stsci.edu/display/PANSTARRS/How+to+separate+stars+and+galaxies

we perform the photometric calibration in the IMACS g, $r$- and i-bands using objects with PanSTARRS magnitudes in the range of 17.2–21.5 (67 sources), 17.0–20.8 (99 sources) and 16.9–20.0 (95 sources) respectively in the field of W0410–0913. In the field of W0831+0140, the ranges used were 17.8–20.5 (106 sources), 17.8–21.0 (102 sources) and 18.7–20.5 (132 sources) for g, r and i respectively. We found two color terms were needed, so we used the g-r and r-i PanSTARRS colors for the IMACS r-band, and the r-i and i-z PanSTARRS colors for the IMACS z-band. The 1, 3 and 5$\sigma$ depths of the image stacks are shown in Table 4.1.

We estimated the photometric constant considering point sources with magnitudes: for W0410–0913, $17.2 < g < 21.5$ (67 sources), $17.0 < r < 20.8$ (99 sources), and $16.9 < i < 20.0$ (95 sources) in Pan-STARRS. For W0831+0140, $17.8 < g < 20.5$ (106 sources), $17.8 < r < 21.0$ (102 sources), and $18.7 < i < 20.5$ (132 sources) in Pan-STARRS. We found that to calibrate the g-band IMACS observations, a single color term, g-r from PanSTARRS was needed in addition to the PanSTARRS g-band magnitude. For the r- and i-band IMACS observations

### 4.2.2   Gemini GMOS-S data

We also used deep imaging data in the $r$-, $i$-, and $z$-bands of Gemini GMOS-S presented by Zewdie et al. (2023). This study focused on examining the environment of W2246–0526 and comparing it with the SDF/SXDF blank field. The magnitude limits of the detected sources in the observations were established based on the 3$\sigma$ limit of the $i$- and $z$-band magnitudes, which are 27.16 and 26.57, respectively. Additionally, the $r$-band magnitude was required to be

brighter than the $1\sigma$ limit, which is 29.0. The field of view of GMOS-S is $5.5' \times 5.5'$. In their study,Zewdie et al. (2023) masked the area around bright saturated stars.. They also masked the spikes and the border of the image, resulting in a usable area of 23.7 arcmin$^2$. For detailed information regarding the observations, we refer the reader to Zewdie et al. (2023).

### 4.2.3   COSMOS data

The COSMOS field (Scoville et al., 2007) offers a unique and multi-wavelength dataset covering a relatively large area of $\sim$2 deg$^2$. Here, we use Here, we use the COSMOS2020 catalog (Weaver et al., 2022)[5], with detection of over $\sim$1.7 million sources.

We, specifically, use the Subaru HSC $g$-, $r$-, $i$- and $z$- photometry of the sources in the COSMOS2020 catalog. We only considered sources that were detected without photometric issues caused by saturated stars and their spikes. We require sources to be in the combined region (i.e., to have FLAG_COMBINED=0, hereafter, combined catalog) to ensure a uniform quality of photometric redshifts and object classifications. The area of this combined region is 1.278 deg$^2$. As discussed earlier, we use the COSMOS field both as a blank to assess the magnitude of the overdensities, as well as to optimize the selection function (see Section 4.3.

## 4.3   Selection function optimization

We use the COSMOS2020 catalog to define optimal selection functions for companions. In order to optimize the selection function,

---

[5]The COSMOS2020 catalog is available for download at `https://cosmos2020.calet.org/`

we used the HSC $g$, $r$, $i$, and $z$ observations of COSMOS (see Section 4.2.3), as the depths of these observations are deeper than our IMACS observations and comparable in depth to the GMOS-S observations. The filter curves are very similar between the instruments.

Specifically, we derive the selection function for the field of each of the three Hot DOGs, W0410–0913 at $z = 3.631$, W0831+0140 at $z = 3.912$, and W2246–0526 at $z = 4.601$, by optimizing the selection of sources within +/-0.1 units of redshift from each Hot DOG. The combined catalog has a total of 723,897 sources and includes spectroscopic or accurate photometric redshift estimates, as well as separate classifications for galaxies, stars, X-rays, and failures, which enable us to estimate the contamination level.

As mentioned earlier, the HSC observations of the COSMOS field are much deeper than our IMACS observations. This is not ideal as the sources in COSMOS will have a different scatter than those in our IMACS fields that could impact the efficiency of the selection function. To account for this, we added noise to the HSC COSMOS photometry to match that of our observations. We modeled the photometric uncertainty as a function of magnitude in our IMACS fields as:

$$\delta m(m) = Ae^{\beta m} \tag{4.1}$$

where $\delta$m is the magnitude error, m is magnitude, and A and $\beta$ are constants to fit for.

As shown in Table 4.2, we find $\beta$ and A values for each filter in both Hot DOG fields. We note that for background dominated uncertainties, one would expect $\beta = 0.92$, which is very close to the best-fit

TABLE 4.2: Constants to model the photometric uncertainty as a function of magnitude in our IMACS fields.

| Hot DOGs | filters | $\beta$ | A $(10^{-11})$ |
|---|---|---|---|
| W0410–0913 | g | 0.903 | 0.801 |
|  | r | 0.896 | 2.035 |
|  | i | 0.901 | 3.371 |
| W0831+0140 | g | 0.905 | 0.909 |
|  | r | 0.894 | 3.022 |
|  | i | 0.902 | 3.350 |

values. Using this relation, we create a simulated version of the COS-MOS data for the depth of each of the IMACS field. Specifically, for every object in COSMOS2020, we simulate a new magnitude as a random draw from a Gaussian distribution with mean equal to the COSMOS HSC magnitude in the respective band, and a dispersion equal to $\delta m^2(m) - \delta m^2_{\mathrm{HSC}})^{1/2}$, where $\delta m_{\mathrm{HSC}}$ is the photometric uncertainty of the HSC observations. We exclusively consider sources that are brighter than the $1\sigma$ depth in the $r$- and i-bands. For sources fainter than the $1\sigma$ depth in the g band, we treat them as upper limits without simulating their magnitudes. Similarly, for W2246–0526, where the $1\sigma$ depth in the r band applies, we also treat the sources as upper limits. The GMOS-S observation are similarly deep to the HSC observations of the COSMOS field, and therefore it was not necessary to modify the COSMOS2020 magnitudes.

We optimize the selection separately for each of our fields.We consider COSMOS sources according to specific criteria to minimize the effects of contaminants. In the $g$-, r, and $i$-bands, we select sources fainter than 20 mag. In the i-band, our criteria include selecting sources fainter than the Hot DOG and brighter than the $3\sigma$ depth of our images in the $r$- and i-bands. Specifically, for the IMACS sources, we apply an i-band magnitude limit of i=23.95 for W0410–0913 and i=22.33 for W0831+0140. Similarly, for Hot DOG W2246–0526, we

select COSMOS sources fainter than 20 mag in the $r$- and i-bands and sources in the z-band fainter than the Hot DOG (z=22.31). In the $i$- and z-bands, we ensure that these sources are brighter than the $3\sigma$ depth of our images. We do this because it is unlikely that companions will be brighter than the Hot DOG, so it is better to focus the optimization on the fainter sources to avoid contaminants.

We assume general shape of the selection function compatible with those of Ouchi et al. (2004). Specifically, our selection function requires: i) that sources are red in the bluest color (g-r or r-i depending on the field) to target the Lyman break and the break due to IGM absorption; ii) that sources are blue in the reddest color (r-i or i-z depending on the field); and iii) that they are above a diagonal color threshold joining criteria i and ii to avoid contamination from the lower redshift galaxies. We optimize the selection function by maximizing the contrast of the number of galaxies in the intended redshift range ($N_{\mathrm{Targ}}$) with respect to contaminants. Specifically, we maximize the function:

$$\Theta = \frac{N_{\mathrm{Targ}}}{(N_{\mathrm{Targ}} + N_{\mathrm{low}z} + N_{\mathrm{high}z} + N_{\mathrm{Stars}} + N_{\mathrm{X-ray}} + N_{\mathrm{Fail}})^{1/2}}, \quad (4.2)$$

where $N_{\mathrm{low}z}$ are the galaxies with redshifts below the targeted range, $N_{\mathrm{high}z}$ are the galaxies with redshifts high the targeted range, $N_{\mathrm{Targ}z}$ are the galaxies with redshift targeted +/-0.1, $N_{\mathrm{Stars}}$ are the stars in COSMOS, $N_{\mathrm{X-ray}}$ are the X-ray sources in COSMOS, and $N_{\mathrm{Fail}}$ are the failures in COSMOS, which are failure in the fit (most of these objects have less than 1 band, the reader refers the COSMOS2020 catalogue and  Weaver et al., 2022).

The optimized selection functions are:

$$g - r > 1.017,$$
$$r - i < 0.498,$$
$$g - r > 1.449(r - i) + 0.881, \qquad \text{for W0410–0913, z = 3.631.} \quad (4.3)$$

$$g - r > 1.354,$$
$$r - i < 0.585,$$
$$g - r > 1.311(r - i) + 0.789, \qquad \text{for W0831+0140, z = 3.912.}$$
$$(4.4)$$

$$r - i > 0.968,$$
$$i - z < 0.315,$$
$$r - i > 1.466(i - z) + 0.788, \qquad \text{for W2246–0526, z = 4.601.} \quad (4.5)$$

Figures 4.2 - 4.4 show the color distribution of all sources used to op-
timize the selection functions. The right panels of the Figures also
show the colors of representative galaxy templates from Coleman
et al. (1980), in the redshift range of 0-3. The figure also shows the
colors of the LBG composite spectrum from Shapley et al. (2003),
shifted within the redshift range of 3.0-4.5, with the assumption of
the mean intergalactic medium (IGM) optical depth at this red-
shift (i.e., $\kappa$=1), following the methodology outlined by Zewdie et al.
(2023) and accounting for IGM absorption. The figure shows that
our optimized selection should not be significantly affected by con-
taminants. Those low-redshift galaxies are not within our selection
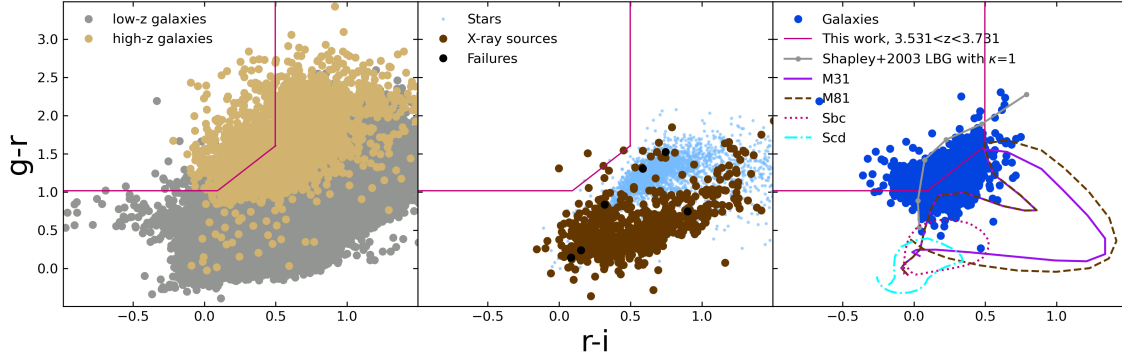
FIGURE 4.2: $g - r$ vs $r - i$ color-color distribution of sources from the combined catalog in the COSMOS field at $3.53 < z < 3.73$. The left panel represents galaxies at lower redshifts ($z < 3.53$, gray) and higher redshifts ($z > 3.73$, tan). The middle panel displays stars, X-ray sources, and failures, while the right panel shows galaxies in the targeted redshift range of $3.621 + /-0.1$. The solid magenta line represents the optimized selection function at $3.53 < z < 3.73$. The gray lines color-redshift track of the LBG composite spectrum of Shapley et al. (2003) with the IGM absorption of Madau (1995) shifted from $z = 3.0$ to $z = 4.25$, and the dots in each track indicate $\delta z = 0.25$ bins. We show the representative colors of several classes of galaxies from Coleman et al. (1980) as a function of redshift from $z = 0$ to 3.
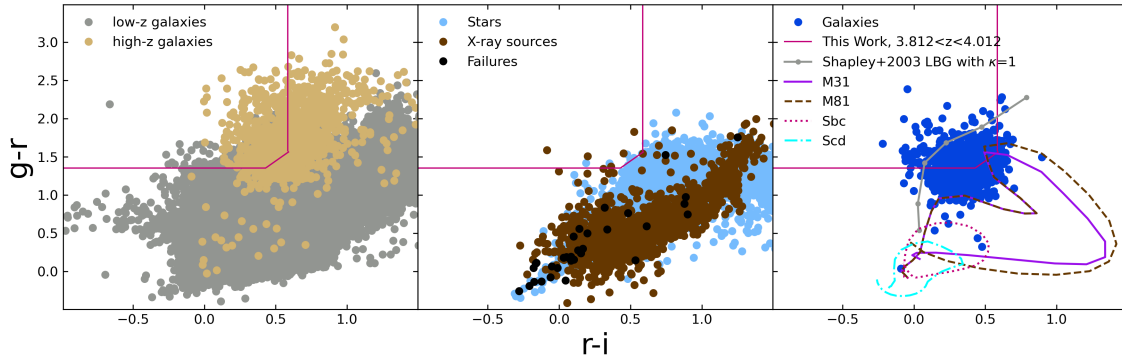


FIGURE 4.3: Same as Figure 4.2 but for optimizing the selection of companions to W0831+0140 in the redshift range $3.912 \pm 0.1$.

criteria.

### 4.3.1   Selected LBG candidates

We applied the magnitude limits that we used to optimize the selection functions described in the previous section to select LBG cadidates around each Hot DOGs field and we found 465, 914, and 89 LBG candidates around W0410–0913, W0831+0140, and W2246–0526, respectively. The Hot DOGs were not positioned at the center
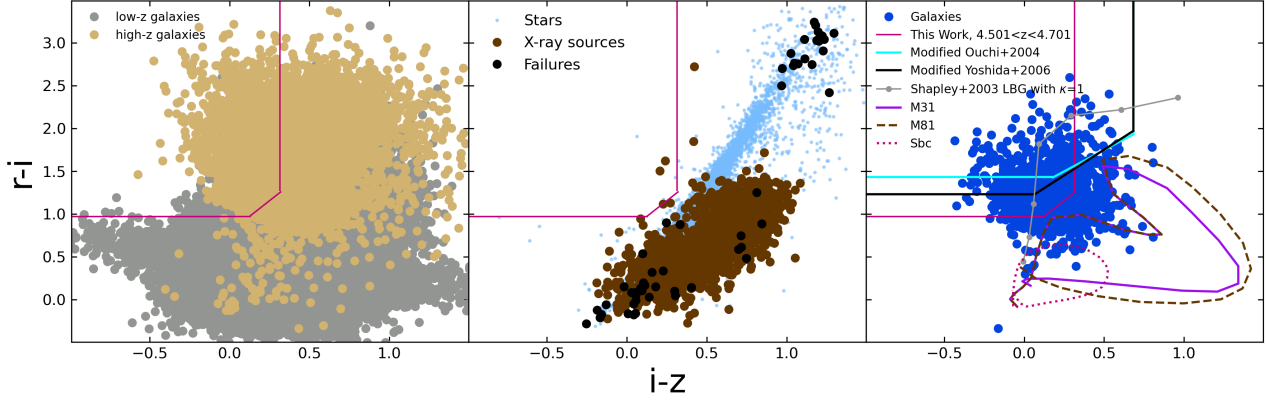
FIGURE 4.4: $r-i$ vs $i-z$ color-color distribution of sources from the combined catalog in the COSMOS field used to optimize the selection of companions to W2246–0526 in the redshift range $4.601 \pm 0.1$. Symbols are defined in the same way as in Figure 4.2. The figure also shows the selection function adopted by Zewdie et al. (2023) based on those of Ouchi et al. (2004, cyan) and the Yoshida et al. (2006, black). See Zewdie et al. (2023) for details. The gray lines color-redshift track of the LBG composite spectrum of Shapley et al. (2003) with the IGM absorption of Madau (1995) shifted from $z = 4.0$ to $z = 5.5$, and the dots in each track indicate $\delta z = 0.25$ bins.

of our IMACS observations. We considered the region around the Hot DOG as the center up to a maximum radius; we refer to this area as the smaller region (see Figure 4.1, the circle region). Within this smaller region, we applied our selection criteria, we found 173 and 259 LBG candidates in the fields of W0410–0913 and W0831+0140, respectively.

Figure 4.5 and 4.6 shows that the color distribution of all detected objects and the selected LBG candidates in each Hot DOG field. We scaled and calculated the overdensity of each Hot DOG using the COSMOS filed as a blank field (see Table 4.3).

We also applied magnitude limits for W2246–0526 and found 89 LBGs around the Hot DOG. Interestingly, we discovered a similar number of LBGs as Zewdie et al. (2023) did, using the modified Y06 selection criteria and accounting for contamination removal. However, the selection functions are not similar, and Zewdie et al. (2023) did not estimate the contaminants. However, W2246–0526 is not
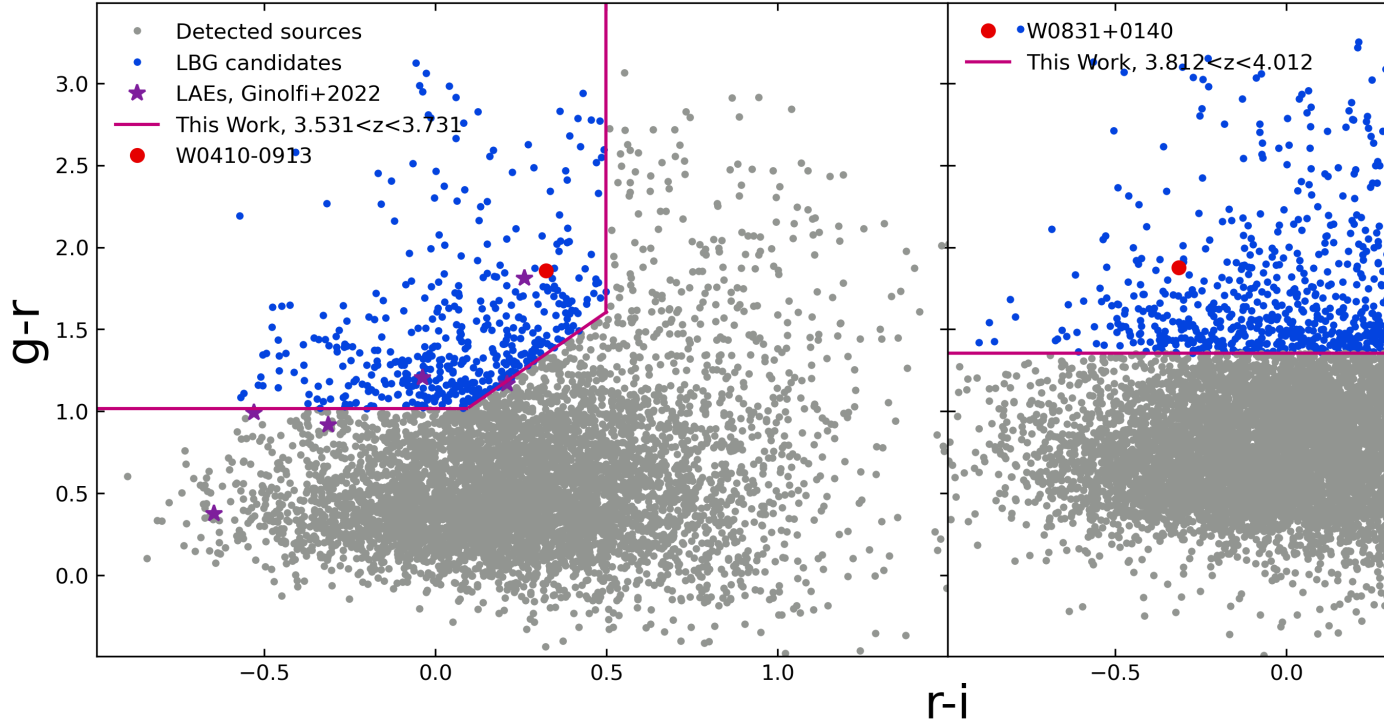
FIGURE 4.5: Left and right panels: Distribution of the $g - r$ vs $r - i$ colors of sources around W0410–0913 at $z = 3.63$ and W0831+0140 at $z = 3.92$, respectively. In both of the panels, the gray dots represent detected sources, and the blue dots represent the LBGs around each field. The magenta lines represent the optimized selection criteria using the combined catalog from the COSMOS field.

selected as an LBG in our study, nor in the study by Zewdie et al. (2023). The optimized selection function includes more sources with bluer colors, and the redward slope is higher (refer to eqn. 4.5 and Zewdie et al., 2023, equations 3 and 4)

Figure 4.7 shows the distribution of magnitudes among the selected LBG candidates around the two Hot DOGs in the three bands. Notably, the magnitudes in the $r$- and i-bands exhibit similar distributions, as expected due to the flat UV spectral energy distributions of LBGs.
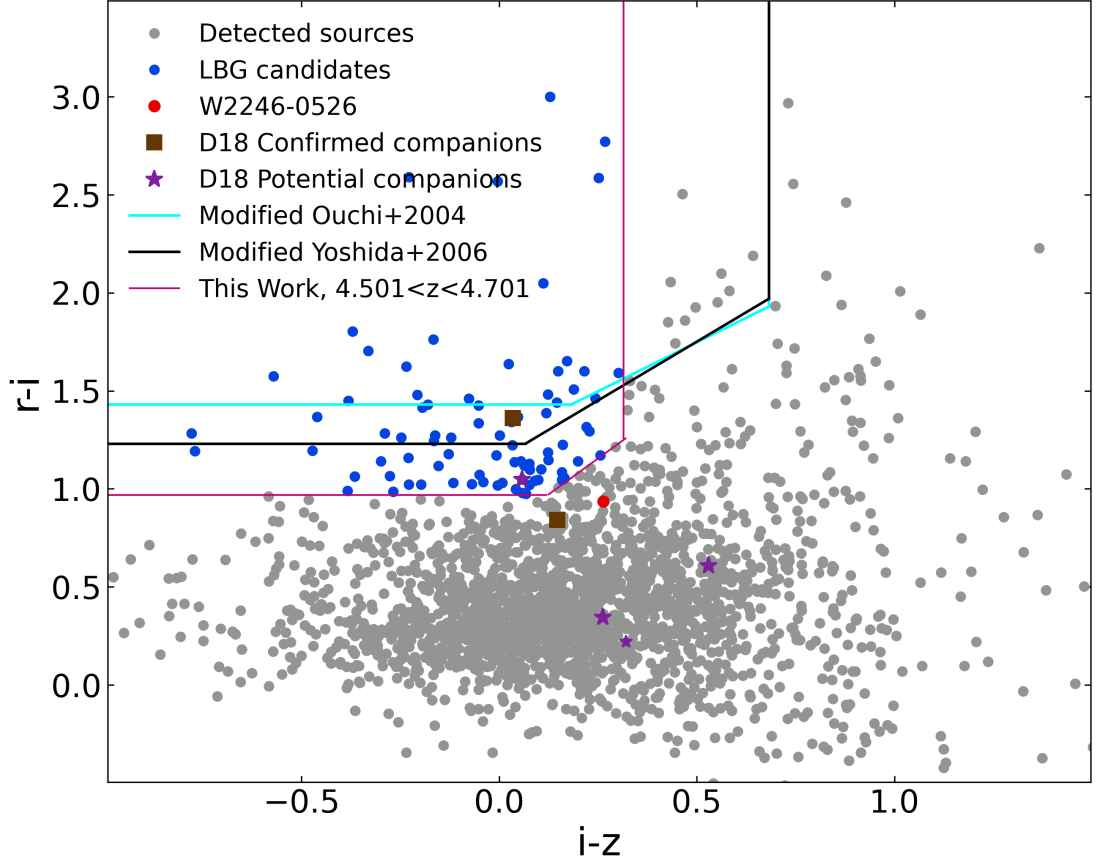
FIGURE 4.6: $r - i$ vs $i - z$ color-color distribution of sources around W2246–0526 at $z = 4.6$. The gray dots represent detected sources, and the blue dots represent the LBGs around each field. The magenta lines represent the optimized selection criteria using the combined catalog from the COSMOS field. The details description of the selection function the same as 4.4

## 4.3.2 Overdensity of LBG around the Hot DOGs

We estimate the magnitude of the overdensities using the surface density of sources identified in the COSMOS field using the optimized selection criteria. Specifically, We estimated the overdensity without considering contamination ($\delta$) and with contamination ($\delta'$). $\delta = \frac{N_F}{N_E^T}$ and $\delta' = \frac{N_F - N_E^C}{N_E^{LBGs}}$, where $N_F$ is the total number of sources selected in our field, $N_E^T$ is the total number of objects that are selected as LBGs, $N_E^C$ represents the number contaminants selected as LBGs in the COSMOS field (see 4.2). For W0410–0913, we found an overdensity of $\delta = 1.56^{+0.12}_{-0.12}$ and $\delta' = 5.37^{+0.95}_{-0.95}$, while for W0831+0140,
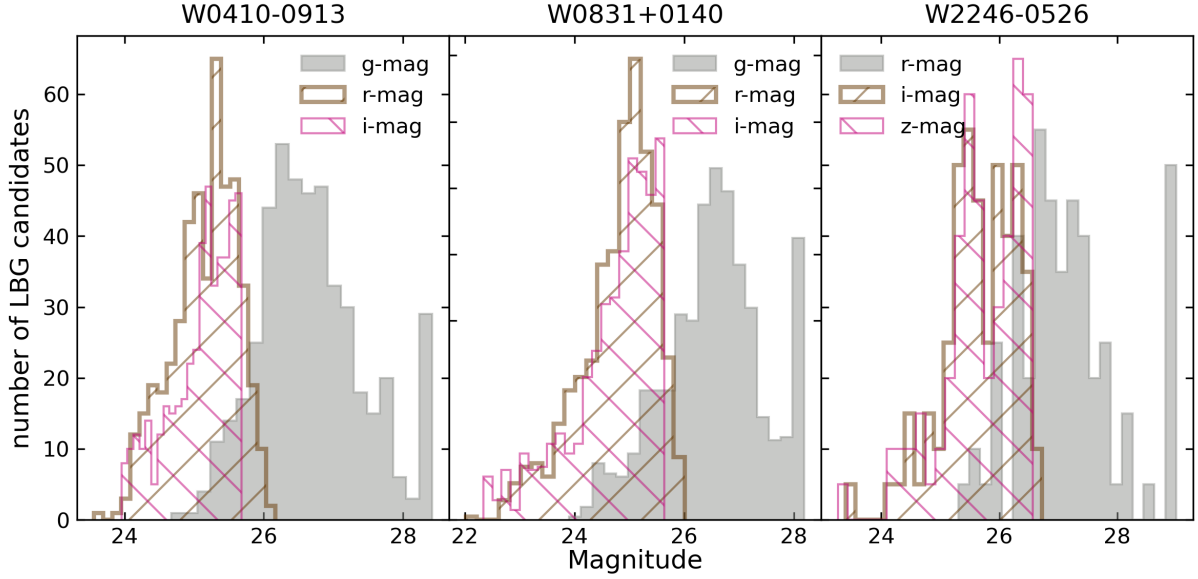
FIGURE 4.7: Left panel: Distribution of magnitudes of the selected LBG candidates at $z = 3.631$ in the W0410–0913 field. Middle panel: Magnitude distribution of selected LBG candidates in the field of W0831+0140 at $z = 3.912$. Right panel: Distribution of magnitudes of selected LBGs around the W2246–0526 field at $z = 4.601$.

the overdensity $\delta = 4.62^{+0.36}_{-0.36}$ and $\delta' = 30.83^{+6.39}_{-6.39}$. We also estimated the overdensity by making the Hot DOGs at the center to the maximizing radius, we observed significantly higher overdensity values compared to the entire area. Specifically, for W0410–0913, the overdensity $\delta = 2.47^{+0.35}_{-0.35}$ and $\delta' = 12.44^{+4.31}_{-4.31}$, and for W0831+0140, the overdensity $\delta = 5.29^{+0.82}_{-0.82}$ and $\delta' = 36.00^{+14.9}_{-14.9}$. We also estimated the overdensity of W2246–0526 and found that $\delta = 2.12^{+0.4}_{-0.4}$ and $\delta' = 6.88^{+2.6}_{-2.6}$. As can be shown in Table 4.3, the ovrdensity of LBGs around the Hot DOGs, which suggest that these objects live in quite dense environment.

Zewdie et al. (2023) found an overdensity of LBG candidates around the Hot DOG W2246–0526. They reported overdensities of $\delta = 7.1^{+1.1}_{-1.1}$ ($\delta = 5.1^{+1.2}_{-1.2}$) using the modified selection criteria from Ouchi et al. (2004) in the SDF (SXDF), and an overdensity of $\delta = 5.2^{+1.4}_{-1.4}$ using the criteria from Yoshida et al. (2006). We found similar figures of overdensity when considering potential contaminants as those that

Zewdie et al. (2023) found using the modified selection criteria from Ouchi et al. (2004) in the SDF field.

Ginolfi et al. (2022) studied the overdensity of LAEs around W0413–0913 using MUSE/VLT, and they identified 24 LAEs associated with this Hot DOG. In our observation, we also identified 10 of these LAEs, three of which were classified as LBGs. Among these, three were faint in the i-band, while one exhibited a brighter i-band. Interestingly, both W0410–0913 and W0831+0140 are selected as LBGs. These objects might have intense star formation and less dust obscuration, or the AGN activity might not be completely dominating their emission.

Figures 4.8 - 4.10 show the comparison of the counts LBG candidates in the fields of W0410–0913 and W0831+0140 as a function of apparent i-band magnitude and W2246–0526 as a function of apparent z-band magnitude. A noticeable trend is observed where the overdensity decreases towards fainter ones. To keep things straightforward, we calculate the uncertainties in our surface density by taking the square root of the number of LBG candidates within each magnitude bin, without accounting for cosmic variance.

### 4.3.3   *riz*-LBGs in COSMOS vs SDF/SXDF

As we discussed in the previous section, We studied, considering only sources fainter than the Hot DOG in the z-bands, and found interesting results. Zewdie et al. (2023) studied the overdensity of LBGs around W2246–0526 using the SDF and SXDF as blank fields. However, we did not specify the magnitude range in the z-band. Zewdie et al. (2023) addressed this aspect by considering the z-band magnitude when estimating overdensity comparisons. We used the same

TABLE 4.3: Statistical information of the three Hot DOGs

| Hot DOGs | Area (deg$^2$) | Selected sources in COSMOS field LBG candidates / Contaminants | Selected objects in our field | $\delta$ | $\delta'$ |
|---|---|---|---|---|---|
| W0410−0913 | 0.05914 | 38 / 261 | 465 | 1.56±0.12 | 5.37±0.95 |
|  | 0.01380 | 9 / 61 | 173 | 2.47±0.35 | 12.44±4.31 |
| W0831+0140 | 0.06543 | 24 / 174 | 914 | 4.62±0.36 | 30.83±6.39 |
|  | 0.01604 | 6 / 43 | 259 | 5.29±0.82 | 36.00±14.9 |
| W2246−0526 | 0.00658 | 8 / 34 | 89 | 2.12±0.40 | 6.88±2.60 |
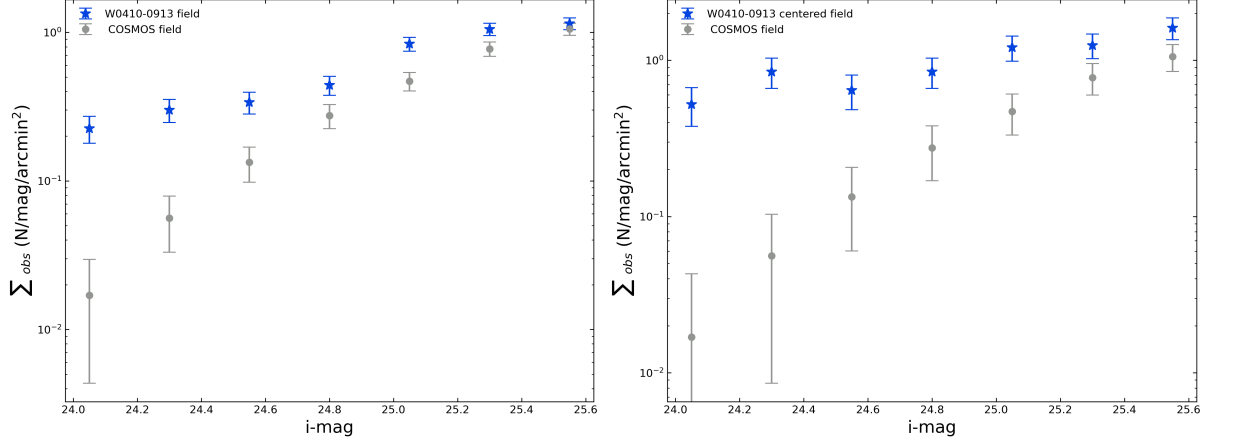
FIGURE 4.8: Surface density of the selected LBG candidates around W0410–0913 (filled blue stars) and the selected objects in the COSMOS field (gray solid circles). Left panel: the selected LBGs in the full image, and the right panel shows a smaller area as depicted in Figure 4.1.
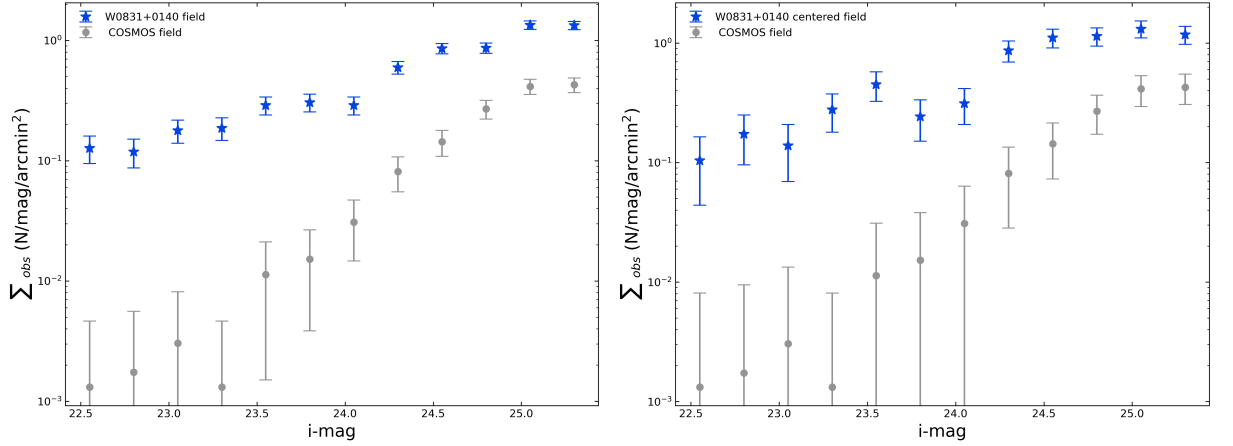


FIGURE 4.9: Surface density of the selected LBG candidates around W0831+0140 (filled blue stars) and the selected objects in the COSMOS field (gray solid circles). Left panel: the selected LBGs in the full image, and the right panel shows a smaller area as depicted in Figure 4.1.

z-band magnitude range as mentioned in both Ouchi et al. (2004) and Yoshida et al. (2006), both of whom used the SDF instrument. However, there are slight differences between the observation field of view (area) and the magnitude range they used. We applied the selection criteria modified by Zewdie et al. (2023) due to considerations of filter curve differences and intergalactic medium absorption at $z = 4.6$. Whereas, given the similarities in filter curves between the GMOS instrument and HSC, we used these selection criteria to
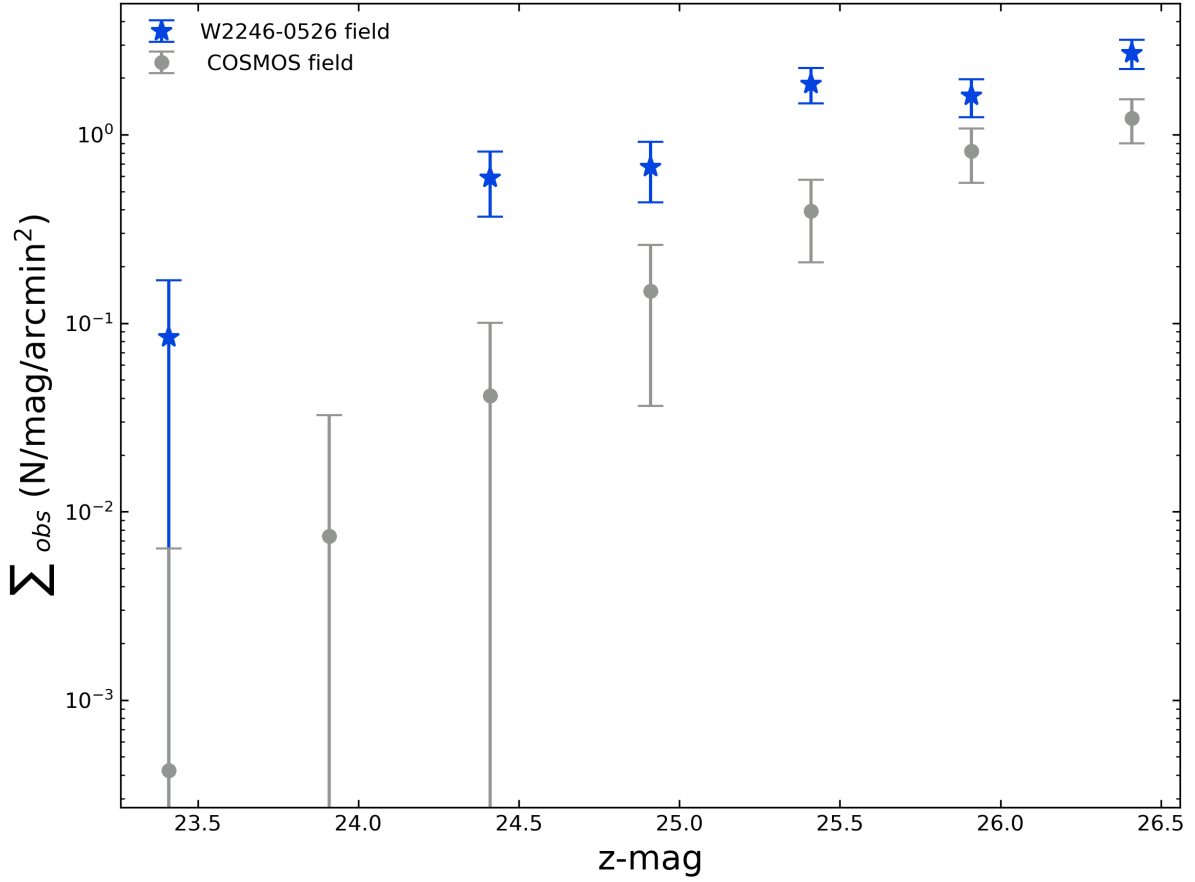
FIGURE 4.10: Surface density of the selected LBG candidates around W2246–0526 (filled blue stars) and the selected objects in the COSMOS field (gray solid circles).

compare the overdensity between the two fields. We also compared the overdensity using Zewdie et al. (2023) selection criteria against the overdensity estimated using the SDF in Ouchi et al. (2004) and Yoshida et al. (2006). Our findings reveal that the COSMOS field exhibits greater density than the SDF/SXDF field. However, we did uncover slight differences between the two selection criteria, which is an intriguing result. We found that the COSMOS field is 2.7 times denser than the SDF, while using the criteria of Yoshida et al. (2006), it is 1.6 times denser. Furthermore, we conducted a comparison with the SXDF and found that the density of the COSMOS field is 2.1 times higher. We checked the targeted coordinates for all fields and confirmed that they are located significantly away from
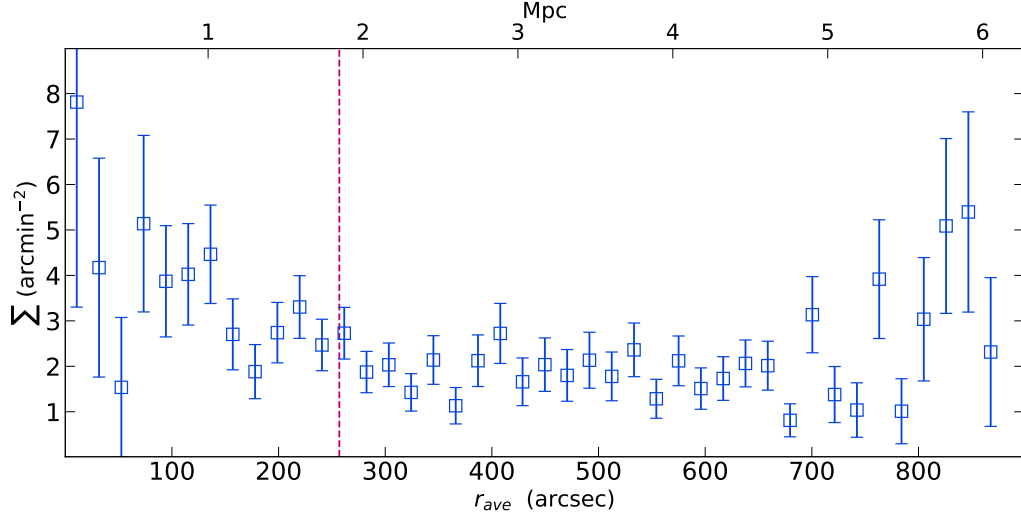
FIGURE 4.11: Spatial distribution of LBG candidates as a function of distance to W0410–0913. We count the number of LBG candidates in annuli with 20 arcsec radius intervals avoiding the inner 1 arcsec (7.222 kpc). The vertical dashed red lines represent the radius (256 arcsec) of the circle, as shown in Figure 4.1.

Galactic coordinates.

### 4.3.4 Spacial distribution

Figures 4.11 and 4.12 show the density of LBG candidates as a function of distance to W0410–0913, and W0831+0140, respectively, measured in 20″ wide annuli centered on the Hot DOG, with the first annulus beginning at 1″. As can be seen in the figures, the overdensity of LBGs tentatively show a profile centered around these Hot DOGs. However, in the case of W2246–0526, we could observe this radial profile. Nonetheless, the observed physical scale is is smaller ∼1.5Mpc, which might be related to the area that we have considered.
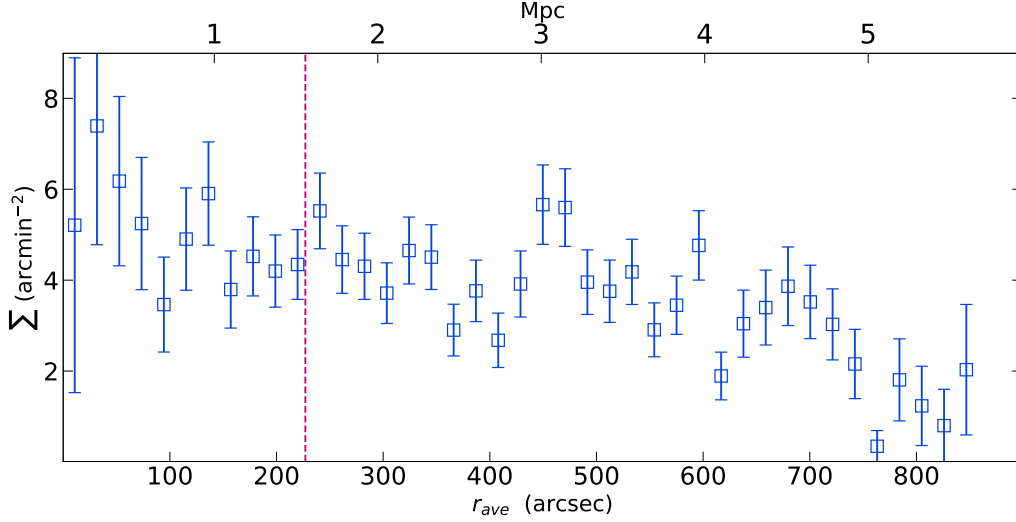
FIGURE 4.12:  Spatial distribution of LBG candidates as a function of distance to W0831+0140. We count the number of LBG candidates in annuli with 20 arcsec radius intervals avoiding the inner 1 arcsec (7.014 kpc). The vertical dashed red lines represent the radius (227 arcsec) of the circle, as shown in Figure 4.1.
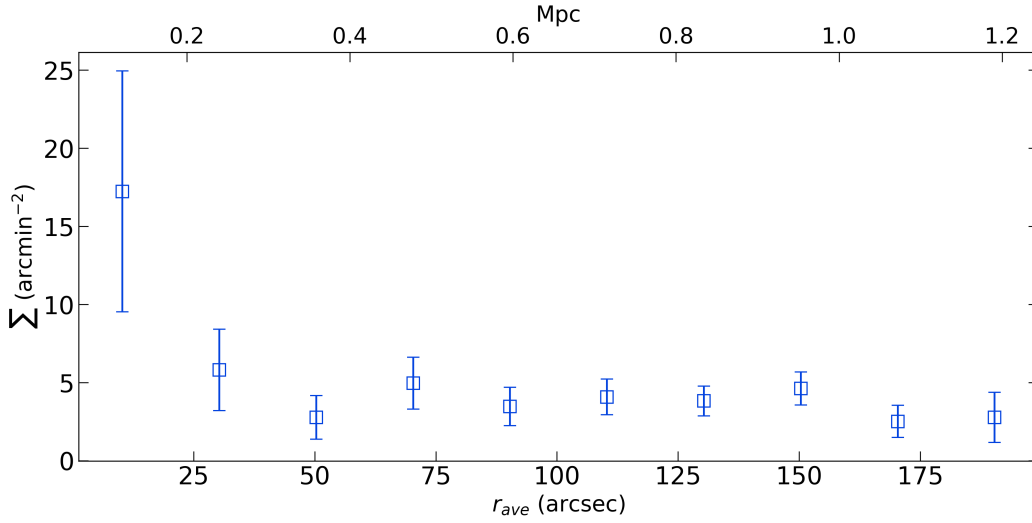


FIGURE 4.13:  Spatial distribution of LBG candidates as a function of distance to W2246–0526.

## 4.4   Discussion

Our analysis has revealed that the three Hot DOGs we are studying reside in clearly overdense environments. We estimated the overdensity of LBG candidates around each field in two ways (see Section 4.3.2): 1) by considering all selected sources in the blank field as

LBGs (without contaminants), $\delta$, and 2) by accounting for potential contaminants in the blank field, $\delta'$. These contaminants include $N_{lowz}$, representing galaxies with redshifts below the targeted range, and $N_{high}$, representing galaxies with redshifts above the targeted range. Additionally, we considered stars, X-ray sources, and failures, but only LBGs with redshifts within the targeted range $\pm 0.1$ were included.

For W0410–0913, we found that $\delta = 1.56^{+0.12}_{-0.12}$ and $\delta' = 5.37^{+0.95}_{-0.95}$, while for W0831+0140, the overdensity was $\delta = 4.62^{+0.36}_{-0.36}$ and $\delta' = 30.83^{+6.39}_{-6.39}$. Additionally, when considering the maximum area that keeps the Hot DOG at the center in all directions, we observed significantly higher overdensity values compared to the full area. Specifically, for W0410–0913, the overdensity was $\delta = 2.47^{+0.35}_{-0.35}$ and $\delta' = 12.44^{+4.31}_{-4.31}$, and for W0831+0140, the overdensity was $\delta = 5.29^{+0.82}_{-0.82}$ and $\delta' = 36.00^{+14.9}_{-14.9}$.

Furthermore, we reanalyzed the study of the environment of W2246–0526 using optimized selection criteria and found $\delta = 2.12^{\pm 0.40}$ and $\delta' = 6.88^{+2.6}_{-2.6}$ times the number of sources found in the COSMOS field. When considering potential contaminants, we obtained a similar result with modified selection criteria Zewdie et al. (2023) and Ouchi et al. (2004), yielding $\delta = 7.1^{+1.1}_{-1.1}$.

Previous studies (e.g., Assef et al., 2015, Jones et al., 2014) have suggested that Hot DOGs reside in dense environments. As mentioned earlier, Zewdie et al. (2023) recently performed a comparison involving the overdensity of Hot DOGs, quasars, and radio galaxies, as illustrated in their Figure 12. In Figure 4.14, we have adapted their figure by adding the overdensity of the three Hot DOGs. Zewdie et al. (2023) estimated the overdensity and studied the spatial distribution
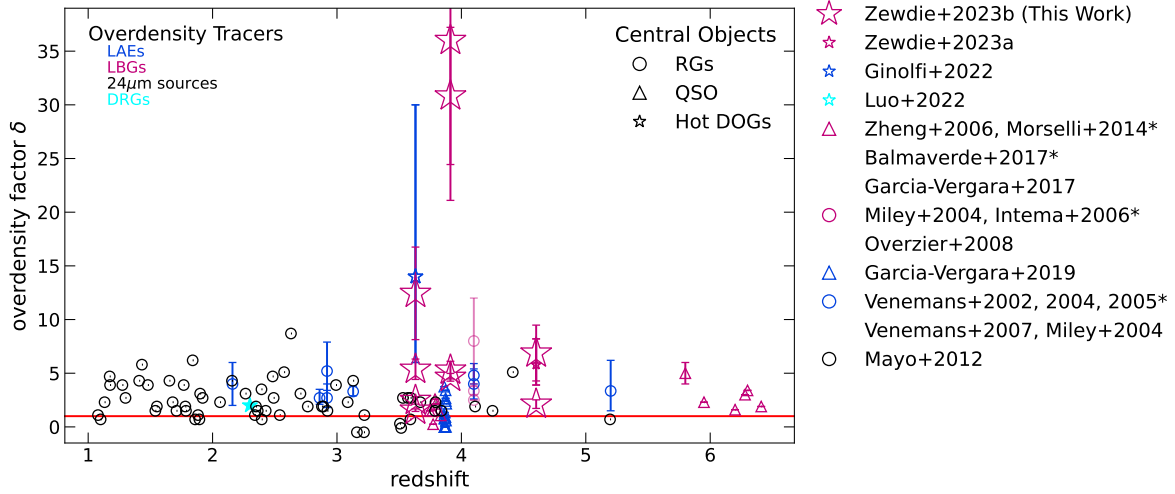
FIGURE 4.14: Adapted from Zewdie et al. (2023), overdensity around high redshift radio galaxies, quasars, and Hot DOGs as a function of redshift. We added additional overdensity figures for Hot DOGs to their figure.

as a function of the distance to the Hot DOG. They found that there is no clear indication of clustering in the radial profile. However, we observed a clear overdensity of LBGs around Hot DOGs, as shown in Figure 4.13. It is important to note that the overdensity is quite similar, but clustering depends on the selection function.

It is worth noting that other galaxies can also inhabit dense environments. The dense environments of Hot DOGs may be related to their unique properties, such as extreme infrared luminosities and high accretion rates onto SMBHs. However, further studies are needed to fully understand the relationship between galaxy properties and their environments.

We found a higher overdensity of LBGs surrounding Hot DOGs compared to other types of quasars, implying that Hot DOGs exist in more densely populated regions. This finding suggests that Hot DOGs inhabit considerably overdense environments, indicating the potential influence of these surroundings on their evolutionary pathways. Consequently, Hot DOGs could serve as potential indicators for protoclusters at high redshifts.

## 4.5    Conclusions

In this work, we present IMACS and GMOS-S observations of three Hot DOGs to study their environments and search for LBGs around each target redshift. The IMACS field of view is larger, enabling us to identify a large sample of LBGs around W0410–0913 at $z = 3.631$ and W0831+0140 at $z = 3.912$, and we reanalyzed W2246–0526 at $z = 4.601$. We optimized the selection criteria using the COSMOS combined catalog, resulting in selected LBG candidates based on these optimized criteria. However, in our IMACS observations, the Hot DOGs were not centered. We studied the environment of these Hot DOGs across the entire field of view. Additionally, we studied the environment by considering the maximum area that keeps the Hot DOG at the center in all directions, with radii of $4.3'$ and $3.8'$ from the Hot DOGs, W0410–0913 and W0831+0140, respectively. Our main findings are as follows:

1. We estimated the overdensity of LBG candidates around three Hot DOGs, covering the entire field of view (the maximum area that keeps the Hot DOG at the center in all directions). For W0410–0913, we found $\delta = 1.56^{+0.12}_{-0.12}$ and $\delta' = 5.37^{+0.95}_{-0.95}$ ($\delta = 2.47^{+0.35}_{-0.35}$ and $\delta' = 12.44^{+4.31}_{-4.31}$), and for W0831+0140, $\delta = 4.62^{+0.36}_{-0.36}$ and $\delta' = 30.83^{+6.39}_{-6.39}$ ($\delta = 5.29^{+0.82}_{-0.82}$ and $\delta' = 36.00^{+14.9}_{-14.9}$). We also re-estimated the overdensity of W2246–0526 and found $\delta = 2.12^{\pm0.40}$ and $\delta' = 6.88^{+2.6}_{-2.6}$ times the surface density of LBGs expected in the COSMOS field.

2. Figure 4.11 and 4.12 show the density of LBG candidates as a function of distance from the Hot DOG, counted in rings of 20 arcsec widths starting $1''$ away from W0410–0913 and

W0831+0140, while Figure 4.13 shows the same counting start-
ing 2 arcsec away from W2246−0526. We can observe a clear
radial profile centered on the Hot DOGs.

3. The 3 Hot DOGs live in overdense environments. Our results
   are qualitatively consistent with recent observational studies of
   the environments around Hot DOGs, such as W0410–0913 at
   $z = 3.6$ (Ginolfi et al., 2022), W1835+4355 at $z = 2.35$ (Luo
   et al., 2022), and W2246–0526 at $z = 4.601$ (Zewdie et al., 2023),
   as well as with statistical studies of `Spitzer`/IRAC and submil-
   limeter companions to Hot DOGs (Assef et al., 2015, Jones et al.,
   2014, Fan et al., 2017).

We also compared our work with previous overdensity studies involv-
ing tracers such as LBGs, LAEs, and other companions around Hot
DOGs, quasars, and radio galaxies. We found a higher overdensity
of LBGs around Hot DOGs. This correlation might be linked to the
high-density region, suggesting that Hot DOGs are strong candidates
for protocluster searches. Consequently, further follow-up spectro-
scopic observations are requied to confirm the presence of LBGs, as
well as to identify faint LAEs using instruments like JWST, HST,
and VLT, within these fields on a larger scale.

# Chapter 5

# Conclusions and Outlook

In this thesis, we presented a comprehensively study the AGN and star-formation properties of inside-out assembled galaxies, and the environment of extremely luminous Hot DOGs. The summary of our work, the conclusions drawn, and future directions are presented in this chapter.

## 5.1   General summary

The thesis specifically focuses on achieving two major research projects. In the first project, presented in Chapter 2, we characterized the physical properties of IOAG candidates, aiming to gain a better understanding of the nature of inside-out growth and the connection between environments, AGN, and galaxy evolution. The second area of focus, covered in Chapters 3 and 4, involves characterizing the environments of Hot DOGs by identifying companion Lyman Break Galaxies.

## 5.2 Conclusions

The main results from this comprehensive analysis are:

We studied the physical properties of galaxies expected to show inside-out stellar mass assembly, and their morphologies, focusing on the relationship between AGN and star formation. Specifically, We studied galaxies within a stellar mass range of $\log M* = 10.73 - 11.03 L_\odot$ and redshift $z < 0.1$, using data from SDSS DR8, WISE, GALEX GR6+7, and Galaxy Zoo. Pérez et al. (2013) found that in this stellar mass range the inner regions ($< 0.5 R_{50}$) of galaxies reached 80% of their final stellar mass twice as fast as in the outskirts. Using the BPT diagram for sources with emission lines exhibiting a signal-to-noise ratio (S/N) greater than 3, we identified a substantial fraction of AGN, 40% (33% as LINERs, and 7% as Seyfert 2 galaxies) and composite galaxies (40%) within the subset of galaxies possessing sufficiently strong emission lines for this classification. Notably, IOAG candidates classified as LINERs exhibited the lowest SFRs, with a median $\log SFR/[Myr^{-1}]$ of -1.14. Among these, those with a morphological classification skewed predominantly towards being spirals (35%), rather than ellipticals (14%). Remarkably, the majority of these sources (76%) are located below the main sequence of star formation in the SFR-stellar mass diagram, and in the green valley or red sequence in the color-stellar mass diagram. These results suggest that AGN could have an important role in quenching SF in galaxies.

We presented the environment study using deep Gemini GMOS-S imaging in the $r$, $i$, and $z$ bands. We identified LBG candidates

in the vicinity of W2246–0526 by applying the selection criteria developed by O04 and Y06 in the Subaru Deep Field and the Subaru XMM-Newton Deep Field. These criteria were slightly modified to account for differences in the filters used. As a result, we found 37 and 55 LBG candidates in the two fields, respectively.

Furthermore, we optimized the selection criteria using the COS-MOS2020 photometric redshift catalog and the HSC $r$, $i$, and $z$ bands, identifying a total of 89 LBG candidates in the COSMOS field. We also estimated the overdensity of LBGs around this Hot DOG by comparing with the SDF, SXDF, and COSMOS fields for both the modified O04 and Y06 selection criteria.

The results indicated an overdensity of $\delta = 7.1^{+1.1}_{-1.1}$ ($\delta = 5.1^{+1.2}_{-1.2}$) for the modified O04 selection criteria in the SDF (SXDF), and an overdensity of $\delta = 5.2^{+1.4}_{-1.4}$ for the Y06 selection criteria, and an overdensity $\delta = 2.12^{+0.4}_{-0.4}$ for is the optimized selection in the COSMOS field, assuming that all the selected sources in COS-MOS are LBGs. Additionally, due to the information provided by COSMOS, we are able to estimate the contamination. An overdensity of $\delta^{'} = 6.88^{+2.6}_{-2.6}$ was observed with the optimized COSMOS selection, factoring in the potential contamination in the field. The similarity between the overdensity $\delta^{'}$ and the result obtained with the modified O04 criteria in the SDF field suggests minimal contamination when employing the modified O04 selection function, as they indicated negligible contamination. However, when considering the SXDF and SDF with the modified Y06 selection criteria, we observed a lower level of overdensity. This suggests a potential increase in contamination for

both the SXDF and SDF fields based on the modified Y06 selection criteria. However, there is a possibility of overestimating contamination in COSMOS. Similarly, we do not expect all the selected sources in COSMOS to be LBGs. Therefore, we assume that the overdensity lies between $\delta$ and $\delta'$, implying that $\delta < \delta_{expect} \leq \delta'$.

We further investigated two additional Hot DOGs using deep Magellan/IMACS imaging in the $g$, $r$, and $i$ bands. LBGs were selected around W0410–0913 and W0831+0140 using the optimized selection criteria, as determined by the COSMOS2020 photometric redshift catalog and the HSC $g$, $r$, and $i$ bands. Our optimized selection function factors in selected sources within $\Delta = \pm 0.1$.

We estimated the overdensity without considering contamination ($\delta$) and with contamination ($\delta'$), while also taking into account the central area (where the Hot DOG is kept at the center) and the extended area (as outlined in Table 4.3). For W0410–0913, we found an overdensity of $\delta = 1.56^{+0.12}_{-0.12}$ and $\delta' = 5.37^{+0.95}_{-0.95}$, while for W0831+0140, the overdensity was $\delta = 4.62^{+0.36}_{-0.36}$ and $\delta' = 30.83^{+6.39}_{-6.39}$.

However, when considering the entire field of view, including the maximum area that keeps the Hot DOG at the center in all directions, we observed significantly higher overdensity values compared to the full area. Specifically, for W0410–0913, the overdensity was $\delta = 2.47^{+0.35}_{-0.35}$ and $\delta' = 12.44^{+4.31}_{-4.31}$, and for W0831+0140, the overdensity was $\delta = 5.29^{+0.82}_{-0.82}$ and $\delta' = 36.00^{+14.9}_{-14.9}$.

We discovered an overdensity of LBGs around 3 Hot DOGs, irrespective of the differences in overdensity values. When examining the spatial distribution of LBGs as a function of distance from the Hot DOG, counting them in rings of 20 arcsec widths starting 1 arcsec (W0410–0913 and W0831+0140) and $2''$ (W2246–0526) away from each Hot DOG, we observed a distinct radial profile in all of the Hot DOGs. However, as can be seen Figure 3.9 we did not see a clear radial profile around W2246–0526 when we used the modified O04 and Y06 selection criteria .

We discovered an overdensity of LBGs around 3 Hot DOGs, regardless of the differences in overdensity values. When examining the spatial distribution of LBGs as a function of distance from the Hot DOG, we counted them in rings with widths of 20 arcseconds, starting 2 arcseconds away from each Hot DOG. We observed a distinct radial profile in two of the Hot DOGs, namely W0410–0913 and W0831+0140. However, a clear radial profile was not discernible around W2246–0516. This lack of a clear profile could be due to several factors:

a) The overdensity might be in an early stage of collapse and has not yet fully virialized.

b) While this Hot DOG is the most luminous object in the structure and radiates significantly above the Eddington limit, it might not be the most massive or central galaxy within the structure.

c) The intense radiation emitted by the Hot DOG could potentially impact the transparency of the IGM around it, possibly affecting the radial pattern in the LBG overdensity.

d) The overdensity might be we are looking smaller physical scale

Furthermore, this discrepancy could also be attributed to the field of view of our observation. The IMACS instrument has a field of view 9 times larger than GMOS-S, which might suggest a potential connection with the specific area that we are observing.

Compared with radio galaxies and rest-frame UV bright quasars at a similar redshift, Hot DOGs live in somewhat denser environments (refer to Figure 4.14). This significant overdensity strongly indicates that Hot DOGs are excellent indicators for protoclusters at high redshift.

Previous statistical studies have found significant overdensities of submillimeter- and mid-IR-selected galaxies around Hot DOGs, indicating that they may reside in dense regions. Deep ALMA observations show that W2246–0526 lives in disturbed morphologies within a locally dense environment. Recently, Ginolfi et al. (2022) found an overdensity of LAEs around Hot DOGs, while Luo et al. (2022) revealed an overdensity of distant red galaxies. We also found an overdensity of LBGs around three Hot DOGs. All studies of Hot DOGs' environments show an overdensity with different tracers, suggesting that Hot DOGs are excellent indicators of protoclusters or that these galaxies are in a critical stage of evolution. The underdensity issue that we have might be related to the orientation or depend on the level of obscuration. If the central target is a Type 1 AGN, the radiation (jets) from the center might suppress the UV radiation coming from the companions. This point is not clear yet.

This thesis pushes forward our knowledge of the environment of extremely luminous Hot DOGs population, by presenting a comprehensive study of the overdensity of LBGs around Hot DOGs. However, several questions are still left unanswered:

Do Hot DOGs trace protoclusters or regions of large-scale structure formation?

Are these regions tracers of the early stages of cluster and galaxy group assembly, or are they related to different physical processes in the early universe?

How does the overdensity of Hot DOGs change over cosmic time?

What role does feedback from Hot DOGs play in shaping their surrounding environments?

Can the energy and radiation output from these objects impact the gas properties, star formation, and AGN activity in their vicinity, potentially influencing the overdensity evolution?

Are these overdense regions consistent with our current understanding of galaxy and AGN evolution, or do they challenge existing models and theories of cosmic evolution and large-scale structure formation?

In the following section, we will outline potential future directions aimed at addressing these questions. These directions will make use of both state-of-the-art and upcoming observational facilities and surveys.

## 5.3 Outlook

We selected the LBGs using photometric methods. With the modified and optimized selection function, we surveyed a large number of LBGs around three Hot DOGs. We have plans to conduct follow-up observations for our selected LBG candidates. For one of the Hot DOGs, we have deep MUSE/VLT data for W2246-0526, and the data reduction is complete; the preliminary results are promising. We are able to confirm the selection of five LBG candidates around the Hot DOG within the MUSE field of view (approximately 0.4 Mpc) and are searching for any fainter LAEs. These findings will enable us to gain meaningful insights into the intricate interplay between star formation processes and the environment within these galaxies, providing significant insights into their intrinsic characteristics and surroundings.

The multi-faceted approach of this research expands our knowledge and contributes to the field, providing valuable information about galaxy formation and evolution. Considering the significance of these research endeavors and their potential contributions, we also plan to submit a follow-up proposal to spectroscopically confirm the selected LBGs in the vicinity of Hot DOGs. We aim to observe the bright LBGs surrounding the Hot DOG in our selected sample and confirm the LBG candidates through deep, multi-object spectroscopy, covering projected distances of up to approximately 1.5 Mpc. This will help us confirm the selected LBGs, quantify our selection criteria, and improve our understanding of the intergalactic medium and dust extinction.

We have plans to study the environments of a substantially larger number of Hot DOGs at $z = 3 - 4$ in upcoming semesters. We also

have plans to conduct searches through various publicly available surveys, including COSMOS and LEGACY, targeting Hot DOGs, as well as other obscured AGNs such as Extremely Red Quasars (ERQs). Studying large samples of the environment of extremely luminous, high-redshift Hot DOGs provide valuable insights into the early Universe, probes the co-evolution of galaxies and supermassive black holes, maps the large-scale structure of the Universe, helps us understand quasar fuelling and feedback mechanisms, and tests cosmological models.

We also want to advance our understanding of the formation mechanisms of dense environments in optical-selected ERQs. ERQs and Hot DOGs show similar outflows and their potential close relationship to blue-excess Hot DOGs Assef et al. (2022). Therefore, studying ERQs within their environments is of particular interest. These quasars can provide valuable insights into the conditions and structures of the universe during its early stages. Overall, studying extremely red quasars can provide crucial clues about the evolution of galaxies and the universe itself. The insights gained from this research will be instrumental in the development of models and the ability to make precise predictions concerning galaxy formation, feedback processes, and quasar evolution, which, in turn, will contribute to a more profound understanding of the cosmos.

We find ourselves in a remarkable era marked by the pursuit of overdensity in high-redshift quasars, thanks to the emergence of advanced, extensive sky surveys. In particular, over the last two years, the JWST has greatly expanded the search for high-redshift quasars. Euclid, which recently launched, is instrumental in measuring the distribution of galaxies and galaxy clusters across cosmic time

and understanding high-redshift quasar environments. These instruments have been making a huge contribution to our understanding of high-redshift quasars with $z > 5.5$, allowing us to gain a better understanding of the early universe. Furthermore, several new transformative instruments and surveys are scheduled to come online in the near future (e.g., LSST, 4MOST, ELT, Roman Space Telescope). They will provide an additional exploration of these early galaxies in excellent detail and follow their evolution through cosmic time. This will help us understand how galaxies form and evolve, providing a key contribution to our knowledge of the Universe. Some of them will provide a new foundation for spectroscopic exploration of these early galaxies.

For example, some of the instruments that we expected to come online in the next two years will be available.

**4MOST - 4-metre Multi-Object Spectroscopic Telescope** is a ground-based, wide-area survey optical spectrograph installed on a dedicated 4-meter class telescope. It operates by simultaneously capturing spectra from approximately 2400 objects across a hexagonal field of view spanning 4.2 deg$^2$. This versatile instrument serves as a crucial tool for various spectroscopic follow-up campaigns. It enables us to explore a wide range of astronomical phenomena, including the observation of LBG and fainter LAEs. Moreover, it facilitates the investigation of the growth rate of structures within galaxy clusters and the study of AGN evolution and the growth of black holes over cosmic time, allowing for an exploration of their connection to galaxy evolution.

**The Large Synoptic Survey Telescope (LSST)** is a ground based observatory located in Cerro Pachon, Chile, designed to survey the sky repeatedly over a decade. Its primary scientific objectives include unraveling AGN, dark energy, galaxies, informatics and statistics, the solar system, stars, the Milky Way, the local volume, strong lensing, and transients and variable stars. With its impressive 3.2 Gigapixel camera boasting a wide 9.6-degree field of view, LSST will map a vast expanse of the sky, totaling 30,000 deg$^2$ (Ivezić et al., 2019). LSST have 6 broad band filters (ugrizy).

# References

Masami Ouchi, Kazuhiro Shimasaku, Sadanori Okamura, Hisanori Furusawa, Nobunari Kashikawa, Kazuaki Ota, Mamoru Doi, Masaru Hamabe, Masahiko Kimura, Yutaka Komiyama, Masayuki Miyazaki, Satoshi Miyazaki, Fumiaki Nakata, Maki Sekiguchi, Masafumi Yagi, and Naoki Yasuda. Subaru Deep Survey. V. A Census of Lyman Break Galaxies at z~=4 and 5 in the Subaru Deep Fields: Photometric Properties. *ApJ*, 611(2):660–684, August 2004. doi: 10.1086/422207.

Makiko Yoshida, Kazuhiro Shimasaku, Nobunari Kashikawa, Masami Ouchi, Sadanori Okamura, Masaru Ajiki, Masayuki Akiyama, Hiroyasu Ando, Kentaro Aoki, Mamoru Doi, Hisanori Furusawa, Tomoki Hayashino, Fumihide Iwamuro, Masanori Iye, Hiroshi Karoji, Naoto Kobayashi, Keiichi Kodaira, Tadayuki Kodama, Yutaka Komiyama, Matthew A. Malkan, Yuichi Matsuda, Satoshi Miyazaki, Yoshihiko Mizumoto, Tomoki Morokuma, Kentaro Motohara, Takashi Murayama, Tohru Nagao, Kyoji Nariai, Kouji Ohta, Toshiyuki Sasaki, Yasunori Sato, Kazuhiro Sekiguchi, Yasuhiro Shioya, Hajime Tamura, Yoshiaki Taniguchi, Masayuki Umemura, Toru Yamada, and Naoki Yasuda. Luminosity Functions of Lyman Break Galaxies at z~4 and z~5 in the Subaru Deep Field. *ApJ*, 653(2):988–1003, December 2006. doi: 10.1086/508621.

Carl K. Seyfert. Nuclear Emission in Spiral Nebulae. *ApJ*, 97:28, January 1943. doi: 10.1086/144488.

M. Schmidt. 3C 273 : A Star-Like Object with Large Red-Shift. *Nature*, 197(4872):1040, March 1963. doi: 10.1038/1971040a0.

Maarten Schmidt. Space Distribution and Luminosity Functions of Quasi-Stellar Radio Sources. *ApJ*, 151:393, February 1968. doi: 10.1086/149446.

D. Lynden-Bell and M. J. Rees. On quasars, dust and the galactic centre. *MNRAS*, 152:461, January 1971. doi: 10.1093/mnras/152.4.461.

Robert Antonucci. Unified models for active galactic nuclei and quasars. *ARA&A*, 31:473–521, January 1993. doi: 10.1146/annurev.aa.31.090193.002353.

C. Megan Urry and Paolo Padovani. Unified Schemes for Radio-Loud Active Galactic Nuclei. *PASP*, 107:803, September 1995. doi: 10.1086/133630.

Maia Nenkova, Matthew M. Sirocky, Robert Nikutta, Željko Ivezić, and Moshe Elitzur. AGN Dusty Tori. II. Observational Implications of Clumpiness. *ApJ*, 685(1):160–180, September 2008a. doi: 10.1086/590483.

Maia Nenkova, Matthew M. Sirocky, Željko Ivezić, and Moshe Elitzur. AGN Dusty Tori. I. Handling of Clumpy Media. *ApJ*, 685(1):147–159, September 2008b. doi: 10.1086/590482.

Cristina Ramos Almeida and Claudio Ricci. Nuclear obscuration in active galactic nuclei. *Nature Astronomy*, 1:679–689, October 2017. doi: 10.1038/s41550-017-0232-z.

J. A. Baldwin, M. M. Phillips, and R. Terlevich. Classification parameters for the emission-line spectra of extragalactic objects. *PASP*, 93:5–19, February 1981. doi: 10.1086/130766.

G. Kauffmann, T. M. Heckman, S. D. M. White, S. Charlot, C. Tremonti, J. Brinchmann, G. Bruzual, E. W. Peng, M. Seibert, M. Bernardi, M. Blanton, J. Brinkmann, F. Castander, I. Csábai, M. Fukugita, Z. Ivezic, J. A. Munn, R. C. Nichol, N. Padmanabhan, A. R. Thakar, D. H. Weinberg, and D. York. Stellar masses and star formation histories for $10^5$ galaxies from the Sloan Digital Sky Survey. *MNRAS*, 341:33–53, May 2003. doi: 10.1046/j.1365-8711.2003.06291.x.

L. J. Kewley, B. Groves, G. Kauffmann, and T. Heckman. The host galaxies and classification of active galactic nuclei. *MNRAS*, 372: 961–976, November 2006. doi: 10.1111/j.1365-2966.2006.10859.x.

K. Schawinski, D. Thomas, M. Sarzi, C. Maraston, S. Kaviraj, S.-J. Joo, S. K. Yi, and J. Silk. Observational evidence for AGN feedback in early-type galaxies. *MNRAS*, 382:1415–1431, December 2007. doi: 10.1111/j.1365-2966.2007.12487.x.

Dejene Zewdie, Mirjana Pović, Manuel Aravena, Roberto J. Assef, and Asrate Gaulle. AGN and star formation properties of inside-out assembled galaxy candidates at z ¡ 0.1. *MNRAS*, 498(3):4345–4355, November 2020. doi: 10.1093/mnras/staa2488.

Edward L. Wright, Peter R. M. Eisenhardt, Amy K. Mainzer, Michael E. Ressler, Roc M. Cutri, Thomas Jarrett, J. Davy Kirkpatrick, Deborah Padgett, Robert S. McMillan, Michael Skrutskie, S. A. Stanford, Martin Cohen, Russell G. Walker, John C. Mather, David Leisawitz, III Gautier, Thomas N., Ian McLean, Dominic Benford, Carol J. Lonsdale, Andrew Blain, Bryan Mendez,

William R. Irace, Valerie Duval, Fengchuan Liu, Don Royer, Ingolf Heinrichsen, Joan Howard, Mark Shannon, Martha Kendall, Amy L. Walsh, Mark Larsen, Joel G. Cardon, Scott Schick, Mark Schwalm, Mohamed Abid, Beth Fabinsky, Larry Naes, and Chao-Wei Tsai. The Wide-field Infrared Survey Explorer (WISE): Mission Description and Initial On-orbit Performance. *AJ*, 140(6): 1868–1881, December 2010. doi: 10.1088/0004-6256/140/6/1868.

Peter R. M. Eisenhardt, Jingwen Wu, Chao-Wei Tsai, Roberto Assef, Dominic Benford, Andrew Blain, Carrie Bridge, J. J. Condon, Michael C. Cushing, Roc Cutri, II Evans, Neal J., Chris Gelino, Roger L. Griffith, Carl J. Grillmair, Tom Jarrett, Carol J. Lonsdale, Frank J. Masci, Brian S. Mason, Sara Petty, Jack Sayers, S. A. Stanford, Daniel Stern, Edward L. Wright, and Lin Yan. The First Hyper-luminous Infrared Galaxy Discovered by WISE. *ApJ*, 755(2):173, August 2012. doi: 10.1088/0004-637X/755/2/173.

R. J. Assef, D. Stern, C. S. Kochanek, A. W. Blain, M. Brodwin, M. J. I. Brown, E. Donoso, P. R. M. Eisenhardt, B. T. Jannuzi, T. H. Jarrett, S. A. Stanford, C. W. Tsai, J. Wu, and L. Yan. Mid-infrared Selection of Active Galactic Nuclei with the Wide-field Infrared Survey Explorer. II. Properties of WISE-selected Active Galactic Nuclei in the NDWFS Boötes Field. *ApJ*, 772(1):26, Jul 2013. doi: 10.1088/0004-637X/772/1/26.

R. J. Assef, D. Stern, G. Noirot, H. D. Jun, R. M. Cutri, and P. R. M. Eisenhardt. The WISE AGN Catalog. *ApJS*, 234:23, February 2018. doi: 10.3847/1538-4365/aaa00a.

P. Padovani, D. M. Alexander, R. J. Assef, B. De Marco, P. Giommi, R. C. Hickox, G. T. Richards, V. Smolcic, E. Hatziminaoglou, V. Mainieri, and M. Salvato. Active galactic nuclei: what's in

a name? *Astron. Astrophys. Rev.*, 25(1):2, August 2017. doi: 10.1007/s00159-017-0102-9.

Alar Toomre and Juri Toomre. Galactic Bridges and Tails. *ApJ*, 178:623–666, December 1972. doi: 10.1086/151823.

A. Dressler. Galaxy morphology in rich clusters: implications for the formation and evolution of galaxies. *ApJ*, 236:351–365, March 1980. doi: 10.1086/157753.

H. Butcher and Jr. Oemler, A. The evolution of galaxies in clusters. V. A study of populations since Z 0.5. *ApJ*, 285:426–438, October 1984. doi: 10.1086/162519.

R. B. Larson, B. M. Tinsley, and C. N. Caldwell. The evolution of disk galaxies and the origin of S0 galaxies. *ApJ*, 237:692–707, May 1980. doi: 10.1086/157917.

Kenji Bekki, Warrick J. Couch, and Yasuhiro Shioya. Passive Spiral Formation from Halo Gas Starvation: Gradual Transformation into S0s. *ApJ*, 577(2):651–657, October 2002. doi: 10.1086/342221.

J. Christopher Mihos and Lars Hernquist. Gasdynamics and Starbursts in Major Mergers. *ApJ*, 464:641, June 1996. doi: 10.1086/177353.

Tiziana Di Matteo, Volker Springel, and Lars Hernquist. Energy input from quasars regulates the growth and activity of black holes and their host galaxies. *Nature*, 433(7026):604–607, February 2005. doi: 10.1038/nature03335.

Philip F. Hopkins, Lars Hernquist, Thomas J. Cox, and Dušan Kereš. A Cosmological Framework for the Co-Evolution of Quasars, Supermassive Black Holes, and Elliptical Galaxies. I. Galaxy Mergers and Quasar Activity. *ApJS*, 175(2):356–389, April 2008. doi: 10.1086/524362.

D. M. Alexander and R. C. Hickox. What drives the growth of black holes? *New A Rev.*, 56(4):93–121, June 2012. doi: 10.1016/j. newar.2011.11.003.

E. Treister, K. Schawinski, C. M. Urry, and B. D. Simmons. Major Galaxy Mergers Only Trigger the Most Luminous Active Galactic Nuclei. *ApJL*, 758(2):L39, October 2012. doi: 10.1088/2041-8205/ 758/2/L39.

C. Ricci, F. E. Bauer, E. Treister, K. Schawinski, G. C. Privon, L. Blecha, P. Arevalo, L. Armus, F. Harrison, L. C. Ho, K. Iwasawa, D. B. Sanders, and D. Stern. Growing supermassive black holes in the late stages of galaxy mergers are heavily obscured. *MNRAS*, 468(2):1273–1299, June 2017. doi: 10.1093/mnras/stx173.

Darren J. Croton, Volker Springel, Simon D. M. White, G. De Lucia, C. S. Frenk, L. Gao, A. Jenkins, G. Kauffmann, J. F. Navarro, and N. Yoshida. The many lives of active galactic nuclei: cooling flows, black holes and the luminosities and colours of galaxies. *MNRAS*, 365(1):11–28, January 2006. doi: 10.1111/j.1365-2966.2005.09675. x.

P. Madau and M. Dickinson. Cosmic Star-Formation History. *ARA&A*, 52:415–486, August 2014. doi: 10.1146/ annurev-astro-081811-125615.

F. Vito, W. N. Brandt, G. Yang, R. Gilli, B. Luo, C. Vignali, Y. Q. Xue, A. Comastri, A. M. Koekemoer, B. D. Lehmer,

T. Liu, M. Paolillo, P. Ranalli, D. P. Schneider, O. Shemmer, M. Volonteri, and J. Wang. High-redshift AGN in the Chandra Deep Fields: the obscured fraction and space density of the sub-$L_*$ population. *MNRAS*, 473(2):2378–2406, January 2018. doi: 10.1093/mnras/stx2486.

Jingwen Wu, Chao-Wei Tsai, Jack Sayers, Dominic Benford, Carrie Bridge, Andrew Blain, Peter R. M. Eisenhardt, Daniel Stern, Sara Petty, Roberto Assef, Shane Bussmann, Julia M. Comerford, Roc Cutri, II Evans, Neal J., Roger Griffith, Thomas Jarrett, Sean Lake, Carol Lonsdale, Jeonghee Rho, S. Adam Stanford, Benjamin Weiner, Edward L. Wright, and Lin Yan. Submillimeter Follow-up of WISE-selected Hyperluminous Galaxies. *ApJ*, 756(1):96, September 2012. doi: 10.1088/0004-637X/756/1/96.

Chao-Wei Tsai, Peter R. M. Eisenhardt, Jingwen Wu, Daniel Stern, Roberto J. Assef, Andrew W. Blain, Carrie R. Bridge, Dominic J. Benford, Roc M. Cutri, Roger L. Griffith, Thomas H. Jarrett, Carol J. Lonsdale, Frank J. Masci, Leonidas A. Moustakas, Sara M. Petty, Jack Sayers, S. Adam Stanford, Edward L. Wright, Lin Yan, David T. Leisawitz, Fengchuan Liu, Amy K. Mainzer, Ian S. McLean, Deborah L. Padgett, Michael F. Skrutskie, Christopher R. Gelino, Charles A. Beichman, and Stéphanie Juneau. The Most Luminous Galaxies Discovered by WISE. *ApJ*, 805(2):90, June 2015. doi: 10.1088/0004-637X/805/2/90.

D. Stern, G. B. Lansbury, R. J. Assef, W. N. Brandt, D. M. Alexander, D. R. Ballantyne, M. Baloković, F. E. Bauer, D. Benford, A. Blain, S. E. Boggs, C. Bridge, M. Brightman, F. E. Christensen, A. Comastri, W. W. Craig, A. Del Moro, P. R. M. Eisenhardt, P. Gandhi, R. L. Griffith, C. J. Hailey, F. A. Harrison, R. C.

Hickox, T. H. Jarrett, M. Koss, S. Lake, S. M. LaMassa, B. Luo, C. W. Tsai, C. M. Urry, D. J. Walton, E. L. Wright, J. Wu, L. Yan, and W. W. Zhang. NuSTAR and XMM-Newton Observations of Luminous, Heavily Obscured, WISE-selected Quasars at z ~2. *ApJ*, 794(2):102, October 2014. doi: 10.1088/0004-637X/794/2/102.

R. J. Assef, P. R. M. Eisenhardt, D. Stern, C. W. Tsai, J. Wu, D. Wylezalek, A. W. Blain, C. R. Bridge, E. Donoso, A. Gonzales, R. L. Griffith, and T. H. Jarrett. Half of the Most Luminous Quasars May Be Obscured: Investigating the Nature of WISE-Selected Hot Dust-Obscured Galaxies. *ApJ*, 804(1):27, May 2015. doi: 10.1088/0004-637X/804/1/27.

R. J. Assef, D. J. Walton, M. Brightman, D. Stern, D. Alexander, F. Bauer, A. W. Blain, T. Diaz-Santos, P. R. M. Eisenhardt, S. L. Finkelstein, R. C. Hickox, C. W. Tsai, and J. W. Wu. Hot Dust Obscured Galaxies with Excess Blue Light: Dual AGN or Single AGN Under Extreme Conditions? *ApJ*, 819(2):111, March 2016. doi: 10.3847/0004-637X/819/2/111.

R. J. Assef, M. Brightman, D. J. Walton, D. Stern, F. E. Bauer, A. W. Blain, T. Díaz-Santos, P. R. M. Eisenhardt, R. C. Hickox, H. D. Jun, A. Psychogyios, C. W. Tsai, and J. W. Wu. Hot Dust-obscured Galaxies with Excess Blue Light. *ApJ*, 897(2):112, July 2020. doi: 10.3847/1538-4357/ab9814.

E. Piconcelli, C. Vignali, S. Bianchi, L. Zappacosta, J. Fritz, G. Lanzuisi, G. Miniutti, A. Bongiorno, C. Feruglio, F. Fiore, and R. Maiolino. The hidden quasar nucleus of a WISE-selected, hyper-luminous, dust-obscured galaxy at z ~2.3. *A&A*, 574:L9, February 2015. doi: 10.1051/0004-6361/201425324.

Suzy F. Jones, Andrew W. Blain, Daniel Stern, Roberto J. Assef, Carrie R. Bridge, Peter Eisenhardt, Sara Petty, Jingwen Wu, Chao-Wei Tsai, Roc Cutri, Edward L. Wright, and Lin Yan. Submillimetre observations of WISE-selected high-redshift, luminous, dusty galaxies. *MNRAS*, 443(1):146–157, September 2014. doi: 10.1093/mnras/stu1157.

Suzy F. Jones, Andrew W. Blain, Roberto J. Assef, Peter Eisenhardt, Carol Lonsdale, James Condon, Duncan Farrah, Chao-Wei Tsai, Carrie Bridge, Jingwen Wu, Edward L. Wright, and Tom Jarrett. Overdensities of SMGs around WISE-selected, ultraluminous, high-redshift AGNs. *MNRAS*, 469(4):4565–4577, August 2017. doi: 10.1093/mnras/stx1141.

T. Díaz-Santos, R. J. Assef, A. W. Blain, C. W. Tsai, M. Aravena, P. Eisenhardt, J. Wu, D. Stern, and C. Bridge. The Strikingly Uniform, Highly Turbulent Interstellar Medium of the Most Luminous Galaxy in the Universe. *ApJL*, 816(1):L6, January 2016. doi: 10.3847/2041-8205/816/1/L6.

Dominika Wylezalek, Audrey Galametz, Daniel Stern, Joël Vernet, Carlos De Breuck, Nick Seymour, Mark Brodwin, Peter R. M. Eisenhardt, Anthony H. Gonzalez, Nina Hatch, Matt Jarvis, Alessandro Rettura, Spencer A. Stanford, and Jason A. Stevens. Galaxy Clusters around Radio-loud Active Galactic Nuclei at 1.3 ¡ z ¡ 3.2 as Seen by Spitzer. *ApJ*, 769(1):79, May 2013. doi: 10.1088/0004-637X/769/1/79.

T. Díaz-Santos, R. J. Assef, A. W. Blain, M. Aravena, D. Stern, C. W. Tsai, P. Eisenhardt, J. Wu, H. D. Jun, K. Dibert, H. Inami, G. Lansbury, and F. Leclercq. The multiple merger assembly of a

hyperluminous obscured quasar at redshift 4.6. *Science*, 362(6418): 1034–1036, November 2018. doi: 10.1126/science.aap7605.

M. Ginolfi, E. Piconcelli, L. Zappacosta, G. C. Jones, L. Pentericci, R. Maiolino, A. Travascio, N. Menci, S. Carniani, F. Rizzo, F. Arrigoni Battaia, S. Cantalupo, C. De Breuck, L. Graziani, K. Knudsen, P. Laursen, V. Mainieri, R. Schneider, F. Stanley, R. Valiante, and A. Verhamme. Detection of companion galaxies around hot dust-obscured hyper-luminous galaxy W0410-0913. *Nature Communications*, 13:4574, August 2022. doi: 10.1038/s41467-022-32297-x.

Yibin Luo, Lulu Fan, Hu Zou, Lu Shen, Zesen Lin, Weida Hu, Zheyu Lin, Bojun Tao, and Guangwen Chen. An Overdensity of Red Galaxies around the Hyperluminous Dust-obscured Quasar W1835+4355 at z = 2.3. *ApJ*, 935(2):80, August 2022. doi: 10.3847/1538-4357/ac8162.

Luke Finnerty, Kirsten Larson, B. T. Soifer, Lee Armus, Keith Matthews, Hyunsung D. Jun, Dae-Sik Moon, Jason Melbourne, Percy Gomez, Chao-Wei Tsai, Tanio Díaz-Santos, Peter Eisenhardt, and Michael Cushing. Fast Outflows in Hot Dust-obscured Galaxies Detected with Keck/NIRES. *ApJ*, 905(1):16, December 2020. doi: 10.3847/1538-4357/abc3bf.

Xiaohui Fan, Eduardo Bañados, and Robert A. Simcoe. Quasars and the Intergalactic Medium at Cosmic Dawn. *ARA&A*, 61:373–426, August 2023. doi: 10.1146/annurev-astro-052920-102455.

L. Morselli, M. Mignoli, R. Gilli, C. Vignali, A. Comastri, E. Sani, N. Cappelluti, G. Zamorani, M. Brusa, S. Gallozzi, and E. Vanzella. Primordial environment of super massive black holes:

large-scale galaxy overdensities around z ~6 quasars with LBT. *A&A*, 568:A1, August 2014. doi: 10.1051/0004-6361/201423853.

K. Husband, M. N. Bremer, E. R. Stanway, L. J. M. Davies, M. D. Lehnert, and L. S. Douglas. Are z $\sim$ 5 quasars found in the most massive high-redshift overdensities? *MNRAS*, 432(4):2869–2877, July 2013. doi: 10.1093/mnras/stt642.

Yousuke Utsumi, Tomotsugu Goto, Nobunari Kashikawa, Satoshi Miyazaki, Yutaka Komiyama, Hisanori Furusawa, and Roderik Overzier. A Large Number of z &gt; 6 Galaxies Around a QSO at z = 6.43: Evidence for a Protocluster? *ApJ*, 721(2):1680–1688, October 2010. doi: 10.1088/0004-637X/721/2/1680.

Nobunari Kashikawa, Tetsu Kitayama, Mamoru Doi, Toru Misawa, Yutaka Komiyama, and Kazuaki Ota. The Habitat Segregation between Lyman Break Galaxies and Ly$\alpha$ Emitters around a QSO at z ~5. *ApJ*, 663(2):765–773, July 2007. doi: 10.1086/518410.

W. Zheng, R. A. Overzier, R. J. Bouwens, R. L. White, H. C. Ford, N. Benítez, J. P. Blakeslee, L. D. Bradley, M. J. Jee, A. R. Martel, S. Mei, A. W. Zirm, G. D. Illingworth, M. Clampin, G. F. Hartig, D. R. Ardila, F. Bartko, T. J. Broadhurst, R. A. Brown, C. J. Burrows, E. S. Cheng, N. J. G. Cross, R. Demarco, P. D. Feldman, M. Franx, D. A. Golimowski, T. Goto, C. Gronwall, B. Holden, N. Homeier, L. Infante, R. A. Kimble, J. E. Krist, M. P. Lesser, F. Menanteau, G. R. Meurer, G. K. Miley, V. Motta, M. Postman, P. Rosati, M. Sirianni, W. B. Sparks, H. D. Tran, and Z. I. Tsvetanov. An Overdensity of Galaxies near the Most Distant Radio-loud Quasar. *ApJ*, 640(2):574–578, April 2006. doi: 10.1086/500167.

M. Stiavelli, S. G. Djorgovski, C. Pavlovsky, C. Scarlata, D. Stern, A. Mahabal, D. Thompson, M. Dickinson, N. Panagia, and G. Meylan. Evidence of Primordial Clustering around the QSO SDSS J1030+0524 at z=6.28. *ApJL*, 622(1):L1–L4, March 2005. doi: 10.1086/429406.

Cristina García-Vergara, Joseph F. Hennawi, L. Felipe Barrientos, and Hans-Walter Rix. Strong Clustering of Lyman Break Galaxies around Luminous Quasars at Z ∼ 4. *ApJ*, 848(1):7, October 2017. doi: 10.3847/1538-4357/aa8b69.

Cristina García-Vergara, Joseph F. Hennawi, L. Felipe Barrientos, and Fabrizio Arrigoni Battaia. Clustering of Lyα Emitters around Quasars at z ∼ 4. *ApJ*, 886(2):79, December 2019. doi: 10.3847/1538-4357/ab4d52.

Eduardo Bañados, Bram Venemans, Fabian Walter, Jaron Kurk, Roderik Overzier, and Masami Ouchi. The Galaxy Environment of a QSO at z ~5.7. *ApJ*, 773(2):178, August 2013. doi: 10.1088/0004-637X/773/2/178.

Chris Simpson, Daniel Mortlock, Stephen Warren, Sebastiano Cantalupo, Paul Hewett, Ross McLure, Richard McMahon, and Bram Venemans. No excess of bright galaxies around the redshift 7.1 quasar ULAS J1120+0641. *MNRAS*, 442(4):3454–3461, August 2014. doi: 10.1093/mnras/stu1116.

C. Mazzucchelli, E. Bañados, R. Decarli, E. P. Farina, B. P. Venemans, F. Walter, and R. Overzier. No Overdensity of Lyman-Alpha Emitting Galaxies around a Quasar at z ∼ 5.7. *ApJ*, 834 (1):83, January 2017. doi: 10.3847/1538-4357/834/1/83.

Soyoung Kim, Massimo Stiavelli, M. Trenti, C. M. Pavlovsky, S. G. Djorgovski, C. Scarlata, D. Stern, A. Mahabal, D. Thompson,

M. Dickinson, N. Panagia, and G. Meylan. The Environments of High-Redshift Quasi-Stellar Objects. *ApJ*, 695(2):809–817, April 2009. doi: 10.1088/0004-637X/695/2/809.

Roberto Decarli, Fabian Walter, Bram P. Venemans, Eduardo Bañados, Frank Bertoldi, Chris Carilli, Xiaohui Fan, Emanuele Paolo Farina, Chiara Mazzucchelli, Dominik Riechers, Hans-Walter Rix, Michael A. Strauss, Ran Wang, and Yujin Yang. An ALMA [C II] Survey of 27 Quasars at z ¿ 5.94. *ApJ*, 854(2): 97, February 2018. doi: 10.3847/1538-4357/aaa5aa.

Nathen H. Nguyen, Paulina Lira, Benny Trakhtenbrot, Hagai Netzer, Claudia Cicone, Roberto Maiolino, and Ohad Shemmer. ALMA Observations of Quasar Host Galaxies at z=4.8. *ApJ*, 895(1):74, May 2020. doi: 10.3847/1538-4357/ab8bd3.

Benny Trakhtenbrot, Paulina Lira, Hagai Netzer, Claudia Cicone, Roberto Maiolino, and Ohad Shemmer. ALMA Observations Show Major Mergers Among the Host Galaxies of Fast-growing, High-redshift Supermassive Black Holes. *ApJ*, 836(1):8, February 2017. doi: 10.3847/1538-4357/836/1/8.

Gaël Noirot, Joël Vernet, Carlos De Breuck, Dominika Wylezalek, Audrey Galametz, Daniel Stern, Simona Mei, Mark Brodwin, Elizabeth A. Cooke, Anthony H. Gonzalez, Nina A. Hatch, Alessandro Rettura, and Spencer Adam Stanford. HST Grism Confirmation of Two z=2 Structures from the Clusters around Radio-loud AGN (CARLA) Survey. *ApJ*, 830(2):90, October 2016. doi: 10.3847/0004-637X/830/2/90.

Charles C. Steidel, Max Pettini, and Donald Hamilton. Lyman Imaging of High-Redshift Galaxies.III.New Observations of Four QSO Fields. *AJ*, 110:2519, December 1995. doi: 10.1086/117709.

Mauro Giavalisco. Lyman-Break Galaxies. *ARA&A*, 40:579–641, January 2002. doi: 10.1146/annurev.astro.40.121301.111837.

Alice E. Shapley, Charles C. Steidel, Max Pettini, and Kurt L. Adelberger. Rest-Frame Ultraviolet Spectra of z~3 Lyman Break Galaxies. *ApJ*, 588(1):65–89, May 2003. doi: 10.1086/373922.

Dejene Zewdie, Roberto J. Assef, Chiara Mazzucchelli, Manuel Aravena, Andrew W. Blain, Tanio Díaz-Santos, Peter R. M. Eisenhardt, Hyunsung D. Jun, Daniel Stern, Chao-Wei Tsai, and "and" Jingwen W. Wu. An Overdensity of Lyman Break Galaxies Around the Hot Dust-Obscured Galaxy WISE J224607.56−052634.9. *arXiv e-prints*, art. arXiv:2306.17163, June 2023. doi: 10.48550/arXiv. 2306.17163.

M. Pović, M. Huertas-Company, J. A. L. Aguerri, I. Márquez, J. Masegosa, C. Husillos, A. Molino, D. Cristóbal-Hornillos, J. Perea, N. Benítez, A. del Olmo, A. Fernández-Soto, Y. Jiménez-Teja, M. Moles, E. Alfaro, T. Aparicio-Villegas, B. Ascaso, T. Broadhurst, J. Cabrera-Caño, F. J. Castander, J. Cepa, M. Fernand ez Lorenzo, M. Cerviño, R. M. González Delgado, L. Infante, C. López-Sanjuan, V. J. Martínez, I. Matute, I. Oteo, A. M. Pérez-García, F. Prada, and J. M. Quintana. The ALHAMBRA survey: reliable morphological catalogue of 22 051 early- and late-type galaxies. *MNRAS*, 435(4):3444–3461, Nov 2013. doi: 10.1093/mnras/stt1538.

K. Schawinski, C. M. Urry, B. D. Simmons, L. Fortson, S. Kaviraj, W. C. Keel, C. J. Lintott, K. L. Masters, R. C. Nichol, M. Sarzi, R. Skibba, E. Treister, K. W. Willett, O. I. Wong, and S. K. Yi. The green valley is a red herring: Galaxy Zoo reveals two evolutionary

pathways towards quenching of star formation in early- and late-type galaxies. *MNRAS*, 440:889–907, May 2014. doi: 10.1093/mnras/stu327.

Antoine Mahoro, Mirjana Pović, and Pheneas Nkundabakura. Star formation of far-IR AGN and non-AGN galaxies in the green valley: possible implication of AGN positive feedback. *MNRAS*, 471(3): 3226–3233, Nov 2017. doi: 10.1093/mnras/stx1762.

J. P. Nogueira-Cavalcante, T. S. Gonçalves, K. Menéndez-Delmestre, and K. Sheth. Star formation quenching in green valley galaxies at $0.5 \lesssim z \lesssim 1.0$ and constraints with galaxy morphologies. *MNRAS*, 473(1):1346–1358, Jan 2018. doi: 10.1093/mnras/stx2399.

J. Brinchmann, S. Charlot, T. M. Heckman, G. Kauffmann, C. Tremonti, and S. D. M. White. Stellar masses, star formation rates, metallicities and AGN properties for 200,000 galaxies in the SDSS Data Release Two (DR2). *ArXiv Astrophysics e-prints*, June 2004.

K. E. Whitaker, P. G. van Dokkum, G. Brammer, and M. Franx. The Star Formation Mass Sequence Out to z = 2.5. *ApJL*, 754: L29, August 2012. doi: 10.1088/2041-8205/754/2/L29.

K. Guo, X. Z. Zheng, and H. Fu. The Intrinsic Scatter along the Main Sequence of Star-forming Galaxies at z ˜ 0.7. *ApJ*, 778:23, November 2013. doi: 10.1088/0004-637X/778/1/23.

S. Salim, J. C. Lee, R. Davé, and M. Dickinson. On the Mass-Metallicity-Star Formation Rate Relation for Galaxies at z=2. *ApJ*, 808:25, July 2015. doi: 10.1088/0004-637X/808/1/25.

Antoine Mahoro, Mirjana Pović, Pheneas Nkundabakura, Beatrice Nyiransengiyumva, and Petri Väisänen. Star formation in far-IR AGN and non-AGN galaxies in the green valley - II. Morphological analysis. *MNRAS*, 485(1):452–463, May 2019. doi: 10.1093/mnras/stz434.

A. Dressler and J. E. Gunn. Spectroscopy of galaxies in distant clusters. II - The population of the 3C 295 cluster. *ApJ*, 270:7–19, July 1983. doi: 10.1086/161093.

Ann I. Zabludoff, Dennis Zaritsky, Huan Lin, Douglas Tucker, Yasuhiro Hashimoto, Stephen A. Shectman, Augustus Oemler, and Robert P. Kirshner. The Environment of "E+A" Galaxies. *ApJ*, 466:104, July 1996. doi: 10.1086/177495.

K. Matsubayashi, M. Yagi, T. Goto, A. Akita, H. Sugai, A. Kawai, A. Shimono, and T. Hattori. Spatially resolved spectroscopic observations of a possible e+a progenitor: Sdss j160241.00+521426.9. *The Astrophysical Journal*, 729(1):29, Feb 2011. ISSN 1538-4357. doi: 10.1088/0004-637x/729/1/29. URL http://dx.doi.org/10.1088/0004-637X/729/1/29.

O. Ilbert, M. Salvato, E. Le Floc'h, H. Aussel, P. Capak, H. J. McCracken, B. Mobasher, J. Kartaltepe, N. Scoville, D. B. Sanders, S. Arnouts, K. Bundy, P. Cassata, J. P. Kneib, A. Koekemoer, O. Le Fèvre, S. Lilly, J. Surace, Y. Taniguchi, L. Tasca, D. Thompson, L. Tresse, M. Zamojski, G. Zamorani, and E. Zucca. Galaxy Stellar Mass Assembly Between 0.2 &lt; z &lt; 2 from the S-COSMOS Survey. *ApJ*, 709(2):644–663, February 2010. doi: 10.1088/0004-637X/709/2/644.

K. G. Noeske, B. J. Weiner, S. M. Faber, C. Papovich, D. C. Koo, R. S. Somerville, K. Bundy, C. J. Conselice, J. A. Newman,

D. Schiminovich, E. Le Floc'h, A. L. Coil, G. H. Rieke, J. M. Lotz, J. R. Primack, P. Barmby, M. C. Cooper, M. Davis, R. S. Ellis, G. G. Fazio, P. Guhathakurta, J. Huang, S. A. Kassin, D. C. Martin, A. C. Phillips, R. M. Rich, T. A. Small, C. N. A. Willmer, and G. Wilson. Star Formation in AEGIS Field Galaxies since z=1.1: The Dominance of Gradually Declining Star Formation, and the Main Sequence of Star-forming Galaxies. *ApJL*, 660:L43–L46, May 2007. doi: 10.1086/517926.

D. Elbaz, E. Daddi, D. Le Borgne, M. Dickinson, D. M. Alexander, R.-R. Chary, J.-L. Starck, W. N. Brandt, M. Kitzbichler, E. MacDonald, M. Nonino, P. Popesso, D. Stern, and E. Vanzella. The reversal of the star formation-density relation in the distant universe. *A&A*, 468:33–48, June 2007. doi: 10.1051/0004-6361:20077525.

E. Daddi, D. M. Alexander, M. Dickinson, R. Gilli, A. Renzini, D. Elbaz, A. Cimatti, R. Chary, D. Frayer, F. E. Bauer, W. N. Brandt, M. Giavalisco, N. A. Grogin, M. Huynh, J. Kurk, M. Mignoli, G. Morrison, A. Pope, and S. Ravindranath. Multiwavelength Study of Massive Galaxies at z~2. II. Widespread Compton-thick Active Galactic Nuclei and the Concurrent Growth of Black Holes and Bulges. *ApJ*, 670:173–189, November 2007. doi: 10.1086/521820.

A. Karim, E. Schinnerer, A. Martínez-Sansigre, M. T. Sargent, A. van der Wel, H.-W. Rix, O. Ilbert, V. Smolčić, C. Carilli, M. Pannella, A. M. Koekemoer, E. F. Bell, and M. Salvato. The Star Formation History of Mass-selected Galaxies in the COSMOS Field. *ApJ*, 730:61, April 2011. doi: 10.1088/0004-637X/730/2/61.

K. E. Whitaker, M. Franx, J. Leja, P. G. van Dokkum, A. Henry, R. E. Skelton, M. Fumagalli, I. G. Momcheva, G. B. Brammer,

I. Labbé, E. J. Nelson, and J. R. Rigby. Constraining the Low-mass Slope of the Star Formation Sequence at $0.5 \leq z \leq 2.5$. *ApJ*, 795:104, November 2014. doi: 10.1088/0004-637X/795/2/104.

C. Schreiber, M. Pannella, D. Elbaz, M. Béthermin, H. Inami, M. Dickinson, B. Magnelli, T. Wang, H. Aussel, E. Daddi, S. Juneau, X. Shu, M. T. Sargent, V. Buat, S. M. Faber, H. C. Ferguson, M. Giavalisco, A. M. Koekemoer, G. Magdis, G. E. Morrison, C. Papovich, P. Santini, and D. Scott. The Herschel view of the dominant mode of galaxy growth from z = 4 to the present day. *A&A*, 575:A74, March 2015. doi: 10.1051/0004-6361/201425017.

S. K. Leslie, L. J. Kewley, D. B. Sanders, and N. Lee. Quenching star formation: insights from the local main sequence. *MNRAS*, 455:L82–L86, January 2016. doi: 10.1093/mnrasl/slv135.

M. Pović, I. Márquez, H. Netzer, J. Masegosa, R. Nordon, E. Pérez, and W. Schoenell. Star formation and AGN activity in the most luminous LINERs in the local universe. *MNRAS*, 462:2878–2903, November 2016. doi: 10.1093/mnras/stw1842.

T. S. Gonçalves, D. C. Martin, K. Menéndez-Delmestre, T. K. Wyder, and A. Koekemoer. Quenching Star Formation at Intermediate Redshifts: Downsizing of the Mass Flux Density in the Green Valley. *ApJ*, 759:67, November 2012. doi: 10.1088/0004-637X/759/1/67.

J. Moustakas, A. L. Coil, J. Aird, M. R. Blanton, R. J. Cool, D. J. Eisenstein, A. J. Mendez, K. C. Wong, G. Zhu, and S. Arnouts. PRIMUS: Constraints on Star Formation Quenching and Galaxy Merging, and the Evolution of the Stellar Mass Function from z = 0-1. *ApJ*, 767:50, April 2013. doi: 10.1088/0004-637X/767/1/50.

A. van der Wel, M. Franx, P. G. van Dokkum, R. E. Skelton, I. G. Momcheva, K. E. Whitaker, G. B. Brammer, E. F. Bell, H. W. Rix, S. Wuyts, H. C. Ferguson, B. P. Holden, G. Barro, A. M. Koekemoer, Yu-Yen Chang, E. J. McGrath, B. Häussler, A. Dekel, P. Behroozi, M. Fumagalli, J. Leja, B. F. Lundgren, M. V. Maseda, E. J. Nelson, D. A. Wake, S. G. Patel, I. Labbé, S. M. Faber, N. A. Grogin, and D. D. Kocevski. 3D-HST+CANDELS: The Evolution of the Galaxy Size-Mass Distribution since z = 3. *ApJ*, 788(1):28, June 2014. doi: 10.1088/0004-637X/788/1/28.

Lamiya Mowla, Arjen van der Wel, Pieter van Dokkum, and Tim B. Miller. A Mass-dependent Slope of the Galaxy Size-Mass Relation out to z=3: Further Evidence for a Direct Relation between Median Galaxy Size and Median Halo Mass. *ApJL*, 872(1):L13, February 2019. doi: 10.3847/2041-8213/ab0379.

E. Pérez, R. Cid Fernandes, R. M. González Delgado, R. García-Benito, S. F. Sánchez, B. Husemann, D. Mast, J. R. Rodón, D. Kupko, N. Backsmann, A. L. de Amorim, G. van de Ven, J. Walcher, L. Wisotzki, C. Cortijo-Ferrero, and CALIFA Collaboration. The Evolution of Galaxies Resolved in Space and Time: A View of Inside-out Growth from the CALIFA Survey. *ApJL*, 764: L1, February 2013. doi: 10.1088/2041-8205/764/1/L1.

Zhizheng Pan, Jinrong Li, Weipeng Lin, Jing Wang, Lulu Fan, and Xu Kong. From Outside-in to Inside-out: Galaxy Assembly Mode Depends on Stellar Mass. *ApJL*, 804(2):L42, May 2015. doi: 10. 1088/2041-8205/804/2/L42.

Héctor J. Ibarra-Medel, Sebastián F. Sánchez, Vladimir Avila-Reese, Héctor M. Hernández-Toledo, J. Jesús González, Niv Drory, Kevin Bundy, Dmitry Bizyaev, Mariana Cano-Díaz, Elena

Malanushenko, Kaike Pan, Alexandre Roman-Lopes, and Daniel Thomas. SDSS IV MaNGA: the global and local stellar mass assemby histories of galaxies. *MNRAS*, 463(3):2799–2818, December 2016. doi: 10.1093/mnras/stw2126.

R. García-Benito, R. M. González Delgado, E. Pérez, R. Cid Fernandes, C. Cortijo-Ferrero, R. López Fernández, A. L. de Amorim, E. A. D. Lacerda, N. Vale Asari, S. F. Sánchez, and et al. The spatially resolved star formation history of califa galaxies. *Astronomy & Astrophysics*, 608:A27, Dec 2017. ISSN 1432-0746. doi: 10.1051/0004-6361/201731357. URL http://dx.doi.org/10.1051/0004-6361/201731357.

Qing Liu, Enci Wang, Zesen Lin, Yulong Gao, Haiyang Liu, Berzaf Berhane Teklu, and Xu Kong. Elevation or Suppression? The Resolved Star Formation Main Sequence of Galaxies with Two Different Assembly Modes. *ApJ*, 857(1):17, April 2018. doi: 10.3847/1538-4357/aab3d5.

S. F. Sánchez, V. Avila-Reese, H. Hernandez-Toledo, E. Cortes-Suárez, A. Rodríguez-Puebla, H. Ibarra-Medel, M. Cano-Díaz, J. K. Barrera-Ballesteros, C. A. Negrete, A. R. Calette, A. de Lorenzo-Cáceres, R. A. Ortega-Minakata, E. Aquino, O. Valenzuela, J. C. Clemente, T. Storchi-Bergmann, R. Riffel, J. Schimoia, R. A. Riffel, S. B. Rembold, J. R. Brownstein, K. Pan, R. Yates, N. Mallmann, and T. Bitsakis. SDSS IV MaNGA - Properties of AGN Host Galaxies. *RMxAA*, 54:217–260, April 2018.

Enci Wang, Cheng Li, Ting Xiao, Lin Lin, Matthew Bershady, David R. Law, Michael Merrifield, Sebastian F. Sanchez, Rogemar A. Riffel, Rogerio Riffel, and et al. Sdss-iv manga: Star formation cessation in low-redshift galaxies. i. dependence on stellar

mass and structural properties. *The Astrophysical Journal*, 856(2): 137, Apr 2018. ISSN 1538-4357. doi: 10.3847/1538-4357/aab263. URL http://dx.doi.org/10.3847/1538-4357/aab263.

L. Morselli, A. Renzini, P. Popesso, and G. Erfanianfar. The effect of disc inclination on the main sequence of star-forming galaxies. *MNRAS*, 462(3):2355–2365, November 2016. doi: 10.1093/mnras/ stw1750.

Erica June Nelson, Pieter G. van Dokkum, Natascha M. Förster Schreiber, Marijn Franx, Gabriel B. Brammer, Ivelina G. Momcheva, Stijn Wuyts, Katherine E. Whitaker, Rosalind E. Skelton, Mattia Fumagalli, Christopher C. Hayward, Mariska Kriek, Ivo Labbé, Joel Leja, Hans-Walter Rix, Linda J. Tacconi, Arjen van der Wel, Frank C. van den Bosch, Pascal A. Oesch, Claire Dickey, and Johannes Ulf Lange. Where Stars Form: Inside-out Growth and Coherent Star Formation from HST Hα Maps of 3200 Galaxies across the Main Sequence at 0.7 &lt; z &lt; 1.5. *ApJ*, 828(1):27, September 2016. doi: 10.3847/0004-637X/828/1/27.

Francesco Belfiore, Roberto Maiolino, Kevin Bundy, Karen Masters, Matthew Bershady, Grecco A. Oyarzún, Lihwai Lin, Mariana Cano-Diaz, David Wake, Ashley Spindler, Daniel Thomas, Joel R. Brownstein, Niv Drory, and Renbin Yan. SDSS IV MaNGA - sSFR profiles and the slow quenching of discs in green valley galaxies. *MNRAS*, 477(3):3014–3029, July 2018. doi: 10.1093/mnras/sty768.

S. Tacchella, C. M. Carollo, N. M. Förster Schreiber, A. Renzini, A. Dekel, R. Genzel, P. Lang, S. J. Lilly, C. Mancini, M. Onodera, L. J. Tacconi, S. Wuyts, and G. Zamorani. Dust Attenuation, Bulge Formation, and Inside-out Quenching of Star Formation in

Star-forming Main Sequence Galaxies at z=2. *ApJ*, 859(1):56, May 2018. doi: 10.3847/1538-4357/aabf8b.

Michael Aumer, Simon D. M. White, and Thorsten Naab. The diverse formation histories of simulated disc galaxies. *Monthly Notices of the Royal Astronomical Society*, 441(4):3679–3695, Jun 2014. ISSN 0035-8711. doi: 10.1093/mnras/stu818. URL http://dx.doi.org/10.1093/mnras/stu818.

Vladimir Avila-Reese, Alejandro González-Samaniego, Pedro Colín, Héctor Ibarra-Medel, and Aldo Rodríguez-Puebla. The Global and Radial Stellar Mass Assembly of Milky Way-sized Galaxies. *ApJ*, 854(2):152, February 2018. doi: 10.3847/1538-4357/aaab69.

Rachel Mandelbaum, Uroš Seljak, Guinevere Kauffmann, Christopher M. Hirata, and Jonathan Brinkmann. Galaxy halo masses and satellite fractions from galaxy-galaxy lensing in the Sloan Digital Sky Survey: stellar mass, luminosity, morphology and environment dependencies. *MNRAS*, 368(2):715–731, May 2006. doi: 10.1111/j.1365-2966.2006.10156.x.

Charlie Conroy and Risa H. Wechsler. Connecting Galaxies, Halos, and Star Formation Rates Across Cosmic Time. *ApJ*, 696(1):620–635, May 2009. doi: 10.1088/0004-637X/696/1/620.

Benjamin P. Moster, Rachel S. Somerville, Christian Maulbetsch, Frank C. van den Bosch, Andrea V. Macciò, Thorsten Naab, and Ludwig Oser. Constraints on the Relationship between Stellar Mass and Halo Mass at Low and High Redshift. *ApJ*, 710(2):903–923, February 2010. doi: 10.1088/0004-637X/710/2/903.

Peter S. Behroozi, Charlie Conroy, and Risa H. Wechsler. A Comprehensive Analysis of Uncertainties Affecting the Stellar Mass-Halo

Mass Relation for 0 &lt; z &lt; 4. *ApJ*, 717(1):379–403, July 2010. doi: 10.1088/0004-637X/717/1/379.

Qi Guo, Simon White, Cheng Li, and Michael Boylan-Kolchin. How do galaxies populate dark matter haloes? *MNRAS*, 404(3):1111–1120, May 2010. doi: 10.1111/j.1365-2966.2010.16341.x.

Surhud More, Frank C. van den Bosch, Marcello Cacciato, Ramin Skibba, H. J. Mo, and Xiaohu Yang. Satellite kinematics - III. Halo masses of central galaxies in SDSS. *MNRAS*, 410(1):210–226, January 2011. doi: 10.1111/j.1365-2966.2010.17436.x.

A. Leauthaud, J. Tinker, K. Bundy, P. S. Behroozi, R. Massey, J. Rhodes, M. R. George, J.-P. Kneib, A. Benson, R. H. Wechsler, M. T. Busha, P. Capak, M. Cortês, O. Ilbert, A. M. Koekemoer, O. Le Fèvre, S. Lilly, H. J. McCracken, M. Salvato, T. Schrabback, N. Scoville, T. Smith, and J. E. Taylor. New Constraints on the Evolution of the Stellar-to-dark Matter Connection: A Combined Analysis of Galaxy-Galaxy Lensing, Clustering, and Stellar Mass Functions from z = 0.2 to z =1. *ApJ*, 744:159, January 2012. doi: 10.1088/0004-637X/744/2/159.

F. Shankar, A. Lapi, P. Salucci, G. De Zotti, and L. Danese. New Relationships between Galaxy Properties and Host Halo Mass, and the Role of Feedbacks in Galaxy Formation. *ApJ*, 643:14–25, May 2006. doi: 10.1086/502794.

H. Aihara, C. Allende Prieto, D. An, S. F. Anderson, É. Aubourg, E. Balbinot, T. C. Beers, A. A. Berlind, S. J. Bickerton, D. Bizyaev, M. R. Blanton, J. J. Bochanski, A. S. Bolton, J. Bovy, W. N. Brandt, J. Brinkmann, P. J. Brown, J. R. Brownstein, N. G. Busca, H. Campbell, M. A. Carr, Y. Chen, C. Chiappini, J. Comparat, N. Connolly, M. Cortes, R. A. C. Croft, A. J. Cuesta, L. N.

da Costa, J. R. A. Davenport, K. Dawson, S. Dhital, A. Ealet, G. L. Ebelke, E. M. Edmondson, D. J. Eisenstein, S. Escoffier, M. Esposito, M. L. Evans, X. Fan, B. Femenía Castellá, A. Font-Ribera, P. M. Frinchaboy, J. Ge, B. A. Gillespie, G. Gilmore, J. I. González Hernández, J. R. Gott, A. Gould, E. K. Grebel, J. E. Gunn, J.-C. Hamilton, P. Harding, D. W. Harris, S. L. Hawley, F. R. Hearty, S. Ho, D. W. Hogg, J. A. Holtzman, K. Honscheid, N. Inada, I. I. Ivans, L. Jiang, J. A. Johnson, C. Jordan, W. P. Jordan, E. A. Kazin, D. Kirkby, M. A. Klaene, G. R. Knapp, J.-P. Kneib, C. S. Kochanek, L. Koesterke, J. A. Kollmeier, R. G. Kron, H. Lampeitl, D. Lang, J.-M. Le Goff, Y. S. Lee, Y.-T. Lin, D. C. Long, C. P. Loomis, S. Lucatello, B. Lundgren, R. H. Lupton, Z. Ma, N. MacDonald, S. Mahadevan, M. A. G. Maia, M. Makler, E. Malanushenko, V. Malanushenko, R. Mandelbaum, C. Maraston, D. Margala, K. L. Masters, C. K. McBride, P. M. McGehee, I. D. McGreer, B. Ménard, J. Miralda-Escudé, H. L. Morrison, F. Mullally, D. Muna, J. A. Munn, H. Murayama, A. D. Myers, T. Naugle, A. F. Neto, D. C. Nguyen, R. C. Nichol, R. W. O'Connell, R. L. C. Ogando, M. D. Olmstead, D. J. Oravetz, N. Padmanabhan, N. Palanque-Delabrouille, K. Pan, P. Pandey, I. Pâris, W. J. Percival, P. Petitjean, R. Pfaffenberger, J. Pforr, S. Phleps, C. Pichon, M. M. Pieri, F. Prada, A. M. Price-Whelan, M. J. Raddick, B. H. F. Ramos, C. Reylé, J. Rich, G. T. Richards, H.-W. Rix, A. C. Robin, H. J. Rocha-Pinto, C. M. Rockosi, N. A. Roe, E. Rollinde, A. J. Ross, N. P. Ross, B. M. Rossetto, A. G. Sánchez, C. Sayres, D. J. Schlegel, K. J. Schlesinger, S. J. Schmidt, D. P. Schneider, E. Sheldon, Y. Shu, J. Simmerer, A. E. Simmons, T. Sivarani, S. A. Snedden, J. S. Sobeck, M. Steinmetz, M. A. Strauss, A. S. Szalay, M. Tanaka, A. R. Thakar, D. Thomas,

J. L. Tinker, B. M. Tofflemire, R. Tojeiro, C. A. Tremonti, J. Van-
denberg, M. Vargas Magaña, L. Verde, N. P. Vogt, D. A. Wake,
J. Wang, B. A. Weaver, D. H. Weinberg, M. White, S. D. M. White,
B. Yanny, N. Yasuda, C. Yeche, and I. Zehavi. The Eighth Data
Release of the Sloan Digital Sky Survey: First Data from SDSS-III.
*ApJS*, 193:29, April 2011. doi: 10.1088/0067-0049/193/2/29.

D. G. York, J. Adelman, J. E. Anderson, Jr., S. F. Anderson, J. An-
nis, N. A. Bahcall, J. A. Bakken, R. Barkhouser, S. Bastian,
E. Berman, W. N. Boroski, S. Bracker, C. Briegel, J. W. Briggs,
J. Brinkmann, R. Brunner, S. Burles, L. Carey, M. A. Carr, F. J.
Castander, B. Chen, P. L. Colestock, A. J. Connolly, J. H. Crocker,
I. Csabai, P. C. Czarapata, J. E. Davis, M. Doi, T. Dombeck,
D. Eisenstein, N. Ellman, B. R. Elms, M. L. Evans, X. Fan, G. R.
Federwitz, L. Fiscelli, S. Friedman, J. A. Frieman, M. Fukugita,
B. Gillespie, J. E. Gunn, V. K. Gurbani, E. de Haas, M. Haldeman,
F. H. Harris, J. Hayes, T. M. Heckman, G. S. Hennessy, R. B. Hind-
sley, S. Holm, D. J. Holmgren, C.-h. Huang, C. Hull, D. Husby,
S.-I. Ichikawa, T. Ichikawa, Ž. Ivezić, S. Kent, R. S. J. Kim, E. Kin-
ney, M. Klaene, A. N. Kleinman, S. Kleinman, G. R. Knapp, J. Ko-
rienek, R. G. Kron, P. Z. Kunszt, D. Q. Lamb, B. Lee, R. F. Leger,
S. Limmongkol, C. Lindenmeyer, D. C. Long, C. Loomis, J. Love-
day, R. Lucinio, R. H. Lupton, B. MacKinnon, E. J. Mannery,
P. M. Mantsch, B. Margon, P. McGehee, T. A. McKay, A. Meiksin,
A. Merelli, D. G. Monet, J. A. Munn, V. K. Narayanan, T. Nash,
E. Neilsen, R. Neswold, H. J. Newberg, R. C. Nichol, T. Nicin-
ski, M. Nonino, N. Okada, S. Okamura, J. P. Ostriker, R. Owen,
A. G. Pauls, J. Peoples, R. L. Peterson, D. Petravick, J. R. Pier,
A. Pope, R. Pordes, A. Prosapio, R. Rechenmacher, T. R. Quinn,
G. T. Richards, M. W. Richmond, C. H. Rivetta, C. M. Rockosi,

K. Ruthmansdorfer, D. Sandford, D. J. Schlegel, D. P. Schneider, M. Sekiguchi, G. Sergey, K. Shimasaku, W. A. Siegmund, S. Smee, J. A. Smith, S. Snedden, R. Stone, C. Stoughton, M. A. Strauss, C. Stubbs, M. SubbaRao, A. S. Szalay, I. Szapudi, G. P. Szokoly, A. R. Thakar, C. Tremonti, D. L. Tucker, A. Uomoto, D. Van-den Berk, M. S. Vogeley, P. Waddell, S.-i. Wang, M. Watanabe, D. H. Weinberg, B. Yanny, N. Yasuda, and SDSS Collaboration. The Sloan Digital Sky Survey: Technical Summary. *AJ*, 120:1579–1587, September 2000. doi: 10.1086/301513.

S. Salim, R. M. Rich, S. Charlot, J. Brinchmann, B. D. Johnson, D. Schiminovich, M. Seibert, R. Mallery, T. M. Heckman, K. Forster, P. G. Friedman, D. C. Martin, P. Morrissey, S. G. Neff, T. Small, T. K. Wyder, L. Bianchi, J. Donas, Y.-W. Lee, B. F. Madore, B. Milliard, A. S. Szalay, B. Y. Welsh, and S. K. Yi. UV Star Formation Rates in the Local Universe. *ApJS*, 173:267–292, December 2007. doi: 10.1086/519218.

M. Pović, I. Márquez, J. Masegosa, J. Perea, A. del Olmo, C. Simpson, J. A. L. Aguerri, B. Ascaso, Y. Jiménez-Teja, and C. López-Sanjuan. The impact from survey depth and resolution on the morphological classification of galaxies. *MNRAS*, 453(2):1644–1668, Oct 2015. doi: 10.1093/mnras/stv1663.

L. J. Kewley, C. A. Heisler, M. A. Dopita, and S. Lumsden. Optical Classification of Southern Warm Infrared Galaxies. *ApJS*, 132: 37–71, January 2001. doi: 10.1086/318944.

G. Kauffmann, S. D. M. White, T. M. Heckman, B. Ménard, J. Brinchmann, S. Charlot, C. Tremonti, and J. Brinkmann. The environmental dependence of the relations between stellar mass,

structure, star formation and nuclear activity in galaxies. *MN-RAS*, 353:713–731, September 2004. doi: 10.1111/j.1365-2966. 2004.08117.x.

Sara L. Ellison, Hossen Teimoorinia, David J. Rosario, and J. Trevor Mendel. The star formation rates of active galactic nuclei host galaxies. *MNRAS*, 458(1):L34–L38, May 2016. doi: 10.1093/ mnrasl/slw012.

C. J. Lintott, K. Schawinski, A. Slosar, K. Land, S. Bamford, D. Thomas, M. J. Raddick, R. C. Nichol, A. Szalay, D. Andreescu, P. Murray, and J. Vandenberg. Galaxy Zoo: morphologies derived from visual inspection of galaxies from the Sloan Digital Sky Survey. *MNRAS*, 389:1179–1189, September 2008. doi: 10.1111/j.1365-2966.2008.13689.x.

C. Lintott, K. Schawinski, S. Bamford, A. Slosar, K. Land, D. Thomas, E. Edmondson, K. Masters, R. C. Nichol, M. J. Raddick, A. Szalay, D. Andreescu, P. Murray, and J. Vandenberg. Galaxy Zoo 1: data release of morphological classifications for nearly 900 000 galaxies. *MNRAS*, 410:166–178, January 2011. doi: 10.1111/j.1365-2966.2010.17432.x.

S. P. Bamford, R. C. Nichol, I. K. Baldry, K. Land, C. J. Lintott, K. Schawinski, A. Slosar, A. S. Szalay, D. Thomas, M. Torki, D. Andreescu, E. M. Edmondson, C. J. Miller, P. Murray, M. J. Raddick, and J. Vandenberg. Galaxy Zoo: the dependence of morphology and colour on environment*. *MNRAS*, 393:1324–1352, March 2009. doi: 10.1111/j.1365-2966.2008.14252.x.

L. C. Ho. Nuclear Activity in Nearby Galaxies. *ARA&A*, 46:475–539, September 2008. doi: 10.1146/annurev.astro.45.051806.110546.

Karen L. Masters, Moein Mosleh, A. Kathy Romer, Robert C. Nichol, Steven P. Bamford, Kevin Schawinski, Chris J. Lintott, Dan Andreescu, Heather C. Campbell, Ben Crowcroft, Isabelle Doyle, Edward M. Edmondson, Phil Murray, M. Jordan Raddick, Anže Slosar, Alexander S. Szalay, and Jan Vandenberg. Galaxy Zoo: passive red spirals. *MNRAS*, 405(2):783–799, June 2010. doi: 10.1111/j.1365-2966.2010.16503.x.

Cai-Na Hao, Yong Shi, Yanmei Chen, Xiaoyang Xia, Qiusheng Gu, Rui Guo, Xiaoling Yu, and Songlin Li. Spatially Resolved Studies of Local Massive Red Spiral Galaxies. *ApJL*, 883(2):L36, October 2019. doi: 10.3847/2041-8213/ab42e5.

Smriti Mahajan, Kriti Kamal Gupta, Rahul Rana, M. J. I. Brown, S. Phillipps, Joss Bland-Hawthorn, M. N. Bremer, S. Brough, B. W. Holwerda, A. M. Hopkins, J. Loveday, Kevin Pimbblet, and Lingyu Wang. Galaxy And Mass Assembly (GAMA): properties and evolution of red spiral galaxies. *MNRAS*, 491(1):398–408, January 2020. doi: 10.1093/mnras/stz2993.

J. A. Cardelli, G. C. Clayton, and J. S. Mathis. The relationship between infrared, optical, and ultraviolet extinction. *ApJ*, 345: 245–256, October 1989. doi: 10.1086/167900.

Katherine Alatalo, Sabrina L. Cales, Philip N. Appleton, Lisa J. Kewley, Mark Lacy, Ute Lisenfeld, Kristina Nyland , and Jeffrey A. Rich. Catching Quenching Galaxies: The Nature of the WISE Infrared Transition Zone. *ApJL*, 794(1):L13, October 2014. doi: 10.1088/2041-8205/794/1/L13.

Cheng Li, Enci Wang, Lin Lin, Matthew A. Bershady, Kevin Bundy, Christy A. Tremonti, Ting Xiao, Renbin Yan, Dmitry Bizyaev, Michael Blanton, and et al. P-manga: Gradients in recent star

formation histories as diagnostics for galaxy growth and death. *The Astrophysical Journal*, 804(2):125, May 2015. ISSN 1538-4357. doi: 10.1088/0004-637x/804/2/125. URL http://dx.doi.org/10.1088/0004-637X/804/2/125.

Luciana Bianchi, Bernie Shiao, and David Thilker. Revised catalog of galex ultraviolet sources. i. the all-sky survey: Guvcat˙ais. *The Astrophysical Journal Supplement Series*, 230(2):24, Jun 2017. ISSN 1538-4365. doi: 10.3847/1538-4365/aa7053. URL http://dx.doi.org/10.3847/1538-4365/aa7053.

Gabriella De Lucia and Stefano Borgani. On the stellar populations of massive galaxies. *Monthly Notices of the Royal Astronomical Society: Letters*, 426(1):L61–L65, Aug 2012. ISSN 1745-3925. doi: 10.1111/j.1745-3933.2012.01324.x. URL http://dx.doi.org/10.1111/j.1745-3933.2012.01324.x.

P. A. James and S. M. Percival. Stellar population constraints on the ages of galactic bars. *Monthly Notices of the Royal Astronomical Society*, 457(1):917–925, Jan 2016. ISSN 1365-2966. doi: 10.1093/mnras/stv2978. URL http://dx.doi.org/10.1093/mnras/stv2978.

R. Cid Fernandes, G. Stasińska, A. Mateus, and N. Vale Asari. A comprehensive classification of galaxies in the Sloan Digital Sky Survey: how to tell true from fake AGN? *MNRAS*, 413(3):1687–1699, May 2011. doi: 10.1111/j.1365-2966.2011.18244.x.

C McPartland, D B Sanders, L J Kewley, and S K Leslie. Dissecting the main sequence: Agn activity and bulge growth in the local universe. *Monthly Notices of the Royal Astronomical Society: Letters*, 482(1):L129–L133, Oct 2018. ISSN 1745-3933.

doi: 10.1093/mnrasl/sly202. URL http://dx.doi.org/10.1093/mnrasl/sly202.

Jinyi Yang, Feige Wang, Xiaohui Fan, Aaron J. Barth, Joseph F. Hennawi, Riccardo Nanni, Fuyan Bian, Frederick B. Davies, Emanuele P. Farina, Jan-Torge Schindler, Eduardo Bañados, Roberto Decarli, Anna-Christina Eilers, Richard Green, Hengxiao Guo, Linhua Jiang, Jiang-Tao Li, Bram Venemans, Fabian Walter, Xue-Bing Wu, and Minghao Yue. Probing Early Supermassive Black Hole Growth and Quasar Evolution with Near-infrared Spectroscopy of 37 Reionization-era Quasars at 6.3 ¡ z ≤ 7.64. *ApJ*, 923 (2):262, December 2021. doi: 10.3847/1538-4357/ac2b32.

Emanuele Paolo Farina, Jan-Torge Schindler, Fabian Walter, Eduardo Bañados, Frederick B. Davies, Roberto Decarli, Anna-Christina Eilers, Xiaohui Fan, Joseph F. Hennawi, Chiara Mazzucchelli, Romain A. Meyer, Benny Trakhtenbrot, Marta Volonteri, Feige Wang, Gábor Worseck, Jinyi Yang, Thales A. Gutcke, Bram P. Venemans, Sarah E. I. Bosman, Tiago Costa, Gisella De Rosa, Alyssa B. Drake, and Masafusa Onoue. The X-shooter/ALMA Sample of Quasars in the Epoch of Reionization. II. Black Hole Masses, Eddington Ratios, and the Formation of the First Quasars. *ApJ*, 941(2):106, December 2022. doi: 10.3847/1538-4357/ac9626.

Volker Springel, Simon D. M. White, Adrian Jenkins, Carlos S. Frenk, Naoki Yoshida, Liang Gao, Julio Navarro, Robert Thacker, Darren Croton, John Helly, John A. Peacock, Shaun Cole, Peter Thomas, Hugh Couchman, August Evrard, Jörg Colberg, and Frazer Pearce. Simulations of the formation, evolution and clustering of galaxies and quasars. *Nature*, 435(7042):629–636, June

2005. doi: 10.1038/nature03597.

Marta Volonteri and Martin J. Rees. Quasars at z=6: The Survival of the Fittest. *ApJ*, 650(2):669–678, October 2006. doi: 10.1086/507444.

Tiago Costa, Debora Sijacki, Michele Trenti, and Martin G. Haehnelt. The environment of bright QSOs at z $\sim$ 6: star-forming galaxies and X-ray emission. *MNRAS*, 439(2):2146–2174, April 2014. doi: 10.1093/mnras/stu101.

Mélanie Habouzit, Marta Volonteri, Rachel S. Somerville, Yohan Dubois, Sébastien Peirani, Christophe Pichon, and Julien Devriendt. The diverse galaxy counts in the environment of high-redshift massive black holes in Horizon-AGN. *MNRAS*, 489(1): 1206–1229, October 2019. doi: 10.1093/mnras/stz2105.

Charles C. Steidel, Kurt L. Adelberger, Alice E. Shapley, Max Pettini, Mark Dickinson, and Mauro Giavalisco. Lyman Break Galaxies at Redshift z ˜3: Survey Description and Full Data Set. *ApJ*, 592(2):728–754, August 2003. doi: 10.1086/375772.

Cristina García-Vergara, Matus Rybak, Jacqueline Hodge, Joseph F. Hennawi, Roberto Decarli, Jorge González-López, Fabrizio Arrigoni-Battaia, Manuel Aravena, and Emanuele P. Farina. ALMA Reveals a Large Overdensity and Strong Clustering of Galaxies in Quasar Environments at z 4. *ApJ*, 927(1):65, March 2022. doi: 10.3847/1538-4357/ac469d.

Jaclyn B. Champagne, Roberto Decarli, Caitlin M. Casey, Bram Venemans, Eduardo Bañados, Fabian Walter, Frank Bertoldi, Xiaohui Fan, Emanuele Paolo Farina, Chiara Mazzucchelli, Dominik A. Riechers, Michael A. Strauss, Ran Wang, and Yujin Yang.

No Evidence for Millimeter Continuum Source Overdensities in the Environments of z $\gtrsim$ 6 Quasars. *ApJ*, 867(2):153, November 2018. doi: 10.3847/1538-4357/aae396.

Romain A. Meyer, Roberto Decarli, Fabian Walter, Qiong Li, Ran Wang, Chiara Mazzucchelli, Eduardo Bañados, Emanuele P. Farina, and Bram Venemans. Constraining Galaxy Overdensities around Three z 6.5 Quasars with ALMA and MUSE. *ApJ*, 927(2):141, March 2022. doi: 10.3847/1538-4357/ac4f67.

R. Decarli, F. Walter, B. P. Venemans, E. Bañados, F. Bertoldi, C. Carilli, X. Fan, E. P. Farina, C. Mazzucchelli, D. Riechers, H. W. Rix, M. A. Strauss, R. Wang, and Y. Yang. Rapidly star-forming galaxies adjacent to quasars at redshifts exceeding 6. *Nature*, 545 (7655):457–461, May 2017. doi: 10.1038/nature22358.

Marco Mignoli, Roberto Gilli, Roberto Decarli, Eros Vanzella, Barbara Balmaverde, Nico Cappelluti, Letizia P. Cassarà, Andrea Comastri, Felice Cusano, Kazushi Iwasawa, Stefano Marchesi, Isabella Prandoni, Cristian Vignali, Fabio Vito, Giovanni Zamorani, Marco Chiaberge, and Colin Norman. Web of the giant: Spectroscopic confirmation of a large-scale structure around the z = 6.31 quasar SDSS J1030+0524. *A&A*, 642:L1, October 2020. doi: 10.1051/0004-6361/202039045.

M. Magliocchetti, P. Popesso, M. Brusa, M. Salvato, C. Laigle, H. J. McCracken, and O. Ilbert. The clustering properties of radio-selected AGN and star-forming galaxies up to redshifts z $\sim$ 3. *MNRAS*, 464(3):3271–3280, January 2017. doi: 10.1093/mnras/stw2541.

E. Retana-Montenegro and H. J. A. Röttgering. Probing the radio loud/quiet AGN dichotomy with quasar clustering. *A&A*, 600:A97, April 2017. doi: 10.1051/0004-6361/201526433.

Masaru Ajiki, Yoshiaki Taniguchi, Takashi Murayama, Yasuhiro Shioya, Tohru Nagao, Shunji S. Sasaki, Yuichiro Hatakeyama, Taichi Morioka, Asuka Yokouchi, Mari I. Takahashi, and Osamu Koizumi. New Corroborative Evidence for the Overdensity of Galaxies around the Radio-Loud Quasar SDSS J0836+0054 at z = 5.8. *PASJ*, 58:499–502, June 2006. doi: 10.1093/pasj/58.3.499.

B. P. Venemans, H. J. A. Röttgering, G. K. Miley, W. J. M. van Breugel, C. de Breuck, J. D. Kurk, L. Pentericci, S. A. Stanford, R. A. Overzier, S. Croft, and H. Ford. Protoclusters associated with z ¿ 2 radio galaxies . I. Characteristics of high redshift protoclusters. *A&A*, 461(3):823–845, January 2007. doi: 10.1051/0004-6361:20053941.

Sarah E. I. Bosman, Koki Kakiichi, Romain A. Meyer, Max Gronke, Nicolas Laporte, and Richard S. Ellis. Three Ly$\alpha$ Emitting Galaxies within a Quasar Proximity Zone at z ∼ 5.8. *ApJ*, 896(1):49, June 2020. doi: 10.3847/1538-4357/ab85cd.

Hyunsung D. Jun, Roberto J. Assef, Franz E. Bauer, Andrew Blain, Tanio Díaz-Santos, Peter R. M. Eisenhardt, Daniel Stern, Chao-Wei Tsai, L. Wright, Edward, and Jingwen Wu. Spectral Classification and Ionized Gas Outflows in z ∼ 2 WISE-selected Hot Dust-obscured Galaxies. *ApJ*, 888(2):110, January 2020. doi: 10.3847/1538-4357/ab5e7b.

Chao-Wei Tsai, Peter R. M. Eisenhardt, Hyunsung D. Jun, Jingwen Wu, Roberto J. Assef, Andrew W. Blain, Tanio Díaz-Santos, Suzy F. Jones, Daniel Stern, Edward L. Wright, and Sherry C. C.

Yeh. Super-Eddington Accretion in the WISE-selected Extremely Luminous Infrared Galaxy W2246-0526. *ApJ*, 868(1):15, November 2018. doi: 10.3847/1538-4357/aae698.

Jingwen Wu, Hyunsung D. Jun, Roberto J. Assef, Chao-Wei Tsai, Edward L. Wright, Peter R. M. Eisenhardt, Andrew Blain, Daniel Stern, Tanio Díaz-Santos, Kelly D. Denney, Brian T. Hayden, Saul Perlmutter, Greg Aldering, Kyle Boone, and Parker Fagre-lius. Eddington-limited Accretion in z $\sim$ 2 WISE-selected Hot, Dust-obscured Galaxies. *ApJ*, 852(2):96, January 2018. doi: 10.3847/1538-4357/aa9ff3.

J. I. Penney, A. W. Blain, D. Wylezalek, N. A. Hatch, C. Lons-dale, A. Kimball, R. J. Assef, J. J. Condon, P. R. M. Eisen-hardt, S. F. Jones, M. Kim, M. Lacy, S. I. Muldrew, S. Petty, A. Sajina, A. Silva, D. Stern, T. Diaz-Santos, C. W. Tsai, and J. Wu. The environments of luminous radio-WISE selected in-frared galaxies. *MNRAS*, 483(1):514–528, February 2019. doi: 10.1093/mnras/sty3128.

Charles C. Steidel, Mauro Giavalisco, Max Pettini, Mark Dickinson, and Kurt L. Adelberger. Spectroscopic Confirmation of a Popula-tion of Normal Star-forming Galaxies at Redshifts Z ¿ 3. *ApJL*, 462:L17, May 1996. doi: 10.1086/310029.

Charles C. Steidel, Kurt L. Adelberger, Mauro Giavalisco, Mark Dickinson, and Max Pettini. Lyman-Break Galaxies at z¿~4 and the Evolution of the Ultraviolet Luminosity Density at High Red-shift. *ApJ*, 519(1):1–17, July 1999. doi: 10.1086/307363.

E. Bertin and S. Arnouts. SExtractor: Software for source extraction. *A&AS*, 117:393–404, June 1996. doi: 10.1051/aas:1996164.

J. L. Tonry, C. W. Stubbs, K. R. Lykke, P. Doherty, I. S. Shivvers, W. S. Burgett, K. C. Chambers, K. W. Hodapp, N. Kaiser, R. P. Kudritzki, E. A. Magnier, J. S. Morgan, P. A. Price, and R. J. Wainscoat. The Pan-STARRS1 Photometric System. *ApJ*, 750(2): 99, May 2012. doi: 10.1088/0004-637X/750/2/99.

Yutaro Tachibana and A. A. Miller. A Morphological Classification Model to Identify Unresolved PanSTARRS1 Sources: Application in the ZTF Real-time Pipeline. *PASP*, 130(994):128001, December 2018. doi: 10.1088/1538-3873/aae3d9.

Piero Madau. Radiative Transfer in a Clumpy Universe: The Colors of High-Redshift Galaxies. *ApJ*, 441:18, March 1995. doi: 10.1086/ 175332.

G. D. Coleman, C. C. Wu, and D. W. Weedman. Colors and magnitudes predicted for high redshift galaxies. *ApJS*, 43:393–416, July 1980. doi: 10.1086/190674.

F. Castelli and R. L. Kurucz. Is missing Fe I opacity in stellar atmospheres a significant problem? *A&A*, 419:725–733, May 2004. doi: 10.1051/0004-6361:20040079.

Adam J. Burgasser. The SpeX Prism Library: 1000+ low-resolution, near-infrared spectra of ultracool M, L, T and Y dwarfs. In *Astronomical Society of India Conference Series*, volume 11 of *Astronomical Society of India Conference Series*, pages 7–16, January 2014.

Daniela Calzetti, Lee Armus, Ralph C. Bohlin, Anne L. Kinney, Jan Koornneef, and Thaisa Storchi-Bergmann. The Dust Content and Opacity of Actively Star-forming Galaxies. *ApJ*, 533(2):682–695, April 2000. doi: 10.1086/308692.

Christina C. Williams, Emma Curtis-Lake, Kevin N. Hainline, Jacopo Chevallard, Brant E. Robertson, Stephane Charlot, Ryan Endsley, Daniel P. Stark, Christopher N. A. Willmer, Stacey Alberts, Ricardo Amorin, Santiago Arribas, Stefi Baum, Andrew Bunker, Stefano Carniani, Sara Crandall, Eiichi Egami, Daniel J. Eisenstein, Pierre Ferruit, Bernd Husemann, Michael V. Maseda, Roberto Maiolino, Timothy D. Rawle, Marcia Rieke, Renske Smit, Sandro Tacchella, and Chris J. Willott. The JWST Extragalactic Mock Catalog: Modeling Galaxy Populations from the UV through the Near-IR over 13 Billion Years of Cosmic History. *ApJS*, 236 (2):33, June 2018. doi: 10.3847/1538-4365/aabcbb.

P. Schechter. An analytic expression for the luminosity function for galaxies. *ApJ*, 203:297–306, January 1976. doi: 10.1086/154079.

Jaclyn B. Champagne, Caitlin M. Casey, Steven L. Finkelstein, Micaela Bagley, Olivia R. Cooper, Rebecca L. Larson, Arianna S. Long, and Feige Wang. A Mixture of LBG Overdensities in the Fields of Three $6 < z < 7$ Quasars: Implications for the Robustness of Photometric Selection. *arXiv e-prints*, art. arXiv:2304.10437, April 2023. doi: 10.48550/arXiv.2304.10437.

Feige Wang, Jinyi Yang, Joseph F. Hennawi, Xiaohui Fan, Fengwu Sun, Jaclyn B. Champagne, Tiago Costa, Melanie Habouzit, Ryan Endsley, Zihao Li, Xiaojing Lin, Romain A. Meyer, Jan-Torge Schindler, Yunjing Wu, Eduardo Bañados, Aaron J. Barth, Aklant K. Bhowmick, Rebekka Bieri, Laura Blecha, Sarah Bosman, Zheng Cai, Luis Colina, Thomas Connor, Frederick B. Davies, Roberto Decarli, Gisella De Rosa, Alyssa B. Drake, Eiichi Egami, Anna-Christina Eilers, Analis E. Evans, Emanuele Paolo Farina, Zoltan Haiman, Linhua Jiang, Xiangyu Jin, Hyunsung D. Jun,

Koki Kakiichi, Yana Khusanova, Girish Kulkarni, Mingyu Li, Weizhe Liu, Federica Loiacono, Alessandro Lupi, Chiara Mazzucchelli, Masafusa Onoue, Maria A. Pudoka, Sofia Rojas-Ruiz, Yue Shen, Michael A. Strauss, Wei Leong Tee, Benny Trakhtenbrot, Maxime Trebitsch, Bram Venemans, Marta Volonteri, Fabian Walter, Zhang-Liang Xie, Minghao Yue, Haowen Zhang, Huanian Zhang, and Siwei Zou. A SPectroscopic survey of biased halos In the Reionization Era (ASPIRE): JWST Reveals a Filamentary Structure around a z=6.61 Quasar. *arXiv e-prints*, art. arXiv:2304.09894, April 2023. doi: 10.48550/arXiv.2304.09894.

R. J. Assef, F. E. Bauer, A. W. Blain, M. Brightman, T. Díaz-Santos, P. R. M. Eisenhardt, H. D. Jun, D. Stern, C. W. Tsai, D. J. Walton, and J. W. Wu. Imaging Polarization of the Blue-excess Hot Dust-obscured Galaxy WISE J011601.41-050504.0. *ApJ*, 934 (2):101, August 2022. doi: 10.3847/1538-4357/ac77fc.

B. Balmaverde, R. Gilli, M. Mignoli, M. Bolzonella, M. Brusa, N. Cappelluti, A. Comastri, E. Sani, E. Vanzella, C. Vignali, F. Vito, and G. Zamorani. Primordial environment of supermassive black holes. II. Deep Y- and J-band images around the z 6.3 quasar SDSS J1030+0524. *A&A*, 606:A23, October 2017. doi: 10.1051/0004-6361/20173068310.48550/arXiv.1706.02317.

George K. Miley, Roderik A. Overzier, Zlatan I. Tsvetanov, Rychard J. Bouwens, Narciso Benítez, John P. Blakeslee, Holland C. Ford, Garth D. Illingworth, Marc Postman, Piero Rosati, Mark Clampin, George F. Hartig, Andrew W. Zirm, Huub J. A. Röttgering, Bram P. Venemans, David R. Ardila, Frank Bartko, Tom J. Broadhurst, Robert A. Brown, Chris J. Burrows, E. S. Cheng, Nicholas J. G. Cross, Carlos De Breuck, Paul D. Feldman,

Marijn Franx, David A. Golimowski, Caryl Gronwall, Leopoldo Infante, André R. Martel, Felipe Menanteau, Gerhardt R. Meurer, Marco Sirianni, Randy A. Kimble, John E. Krist, William B. Sparks, Hien D. Tran, Richard L. White, and Wei Zheng. A large population of 'Lyman-break' galaxies in a protocluster at redshift z ~4.1. *Nature*, 427(6969):47–50, January 2004. doi: 10.1038/nature02125.

H. T. Intema, B. P. Venemans, J. D. Kurk, M. Ouchi, T. Kodama, H. J. A. Röttgering, G. K. Miley, and R. A. Overzier. Large-scale structure of Lyman break galaxies around a radio galaxy protocluster at z ∼ 4. *A&A*, 456(2):433–437, September 2006. doi: 10.1051/0004-6361:2006481210.48550/arXiv.astro-ph/0606298.

Roderik A. Overzier, R. J. Bouwens, N. J. G. Cross, B. P. Venemans, G. K. Miley, A. W. Zirm, N. Benítez, J. P. Blakeslee, D. Coe, R. Demarco, H. C. Ford, N. L. Homeier, G. D. Illingworth, J. D. Kurk, A. R. Martel, S. Mei, I. Oliveira, H. J. A. Röttgering, Z. I. Tsvetanov, and W. Zheng. Lyman Break Galaxies, Lyα Emitters, and a Radio Galaxy in a Protocluster at z = 4.1. *ApJ*, 673(1):143–162, January 2008. doi: 10.1086/52434210.48550/arXiv.astro-ph/0601223.

B. P. Venemans, J. D. Kurk, G. K. Miley, H. J. A. Röttgering, W. van Breugel, C. L. Carilli, C. De Breuck, H. Ford, T. Heckman, P. McCarthy, and L. Pentericci. The Most Distant Structure of Galaxies Known: A Protocluster at z=4.1. *ApJL*, 569(1):L11–L14, April 2002. doi: 10.1086/340563.

B. P. Venemans, H. J. A. Röttgering, R. A. Overzier, G. K. Miley, C. De Breuck, J. D. Kurk, W. van Breugel, C. L. Carilli, H. Ford, T. Heckman, P. McCarthy, and L. Pentericci. Discovery of six

Lyα emitters near a radio galaxy at z ∼ 5.2. *A&A*, 424:L17–L20, September 2004. doi: 10.1051/0004-6361:200400041.

B. P. Venemans, H. J. A. Röttgering, G. K. Miley, J. D. Kurk, C. De Breuck, R. A. Overzier, W. J. M. van Breugel, C. L. Carilli, H. Ford, T. Heckman, L. Pentericci, and P. McCarthy. Properties of Lyα emitters around the radio galaxy MRC 0316 257. *A&A*, 431(3):793–812, March 2005. doi: 10.1051/0004-6361:20042038.

J. H. Mayo, J. Vernet, C. De Breuck, A. Galametz, N. Seymour, and D. Stern. Overdensities of 24 μm sources in the vicinities of high-redshift radio galaxies. *A&A*, 539:A33, March 2012. doi: 10.1051/0004-6361/201118254.

Roderik A. Overzier, G. K. Miley, R. J. Bouwens, N. J. G. Cross, A. W. Zirm, N. Benítez, J. P. Blakeslee, M. Clampin, R. Demarco, H. C. Ford, G. F. Hartig, G. D. Illingworth, A. R. Martel, H. J. A. Röttgering, B. Venemans, D. R. Ardila, F. Bartko, L. D. Bradley, T. J. Broadhurst, D. Coe, P. D. Feldman, M. Franx, D. A. Golimowski, T. Goto, C. Gronwall, B. Holden, N. Homeier, L. Infante, R. A. Kimble, J. E. Krist, S. Mei, F. Menanteau, G. R. Meurer, V. Motta, M. Postman, P. Rosati, M. Sirianni, W. B. Sparks, H. D. Tran, Z. I. Tsvetanov, R. L. White, and W. Zheng. Clustering of Star-forming Galaxies Near a Radio Galaxy at z=5.2. *ApJ*, 637(1):58–73, January 2006. doi: 10.1086/498234.

Kazuaki Ota, Bram P. Venemans, Yoshiaki Taniguchi, Nobunari Kashikawa, Fumiaki Nakata, Yuichi Harikane, Eduardo Bañados, Roderik Overzier, Dominik A. Riechers, Fabian Walter, Jun Toshikawa, Takatoshi Shibuya, and Linhua Jiang. Large-scale Environment of a z = 6.61 Luminous Quasar Probed by Lyα Emitters and Lyman Break Galaxies. *ApJ*, 856(2):109, April 2018. doi:

10.3847/1538-4357/aab35b.

Daichi Kashino, Simon J. Lilly, Jorryt Matthee, Anna-Christina Eilers, Ruari Mackenzie, Rongmon Bordoloi, and Robert A. Simcoe. EIGER. I. A Large Sample of [O III]-emitting Galaxies at 5.3 ¡ z ¡ 6.9 and Direct Evidence for Local Reionization by Galaxies. *ApJ*, 950(1):66, June 2023. doi: 10.3847/1538-4357/acc588.

Jorryt Matthee, Ruari Mackenzie, Robert A. Simcoe, Daichi Kashino, Simon J. Lilly, Rongmon Bordoloi, and Anna-Christina Eilers. EIGER. II. First Spectroscopic Characterization of the Young Stars and Ionized Gas Associated with Strong H$\beta$ and [O III] Line Emission in Galaxies at z = 5-7 with JWST. *ApJ*, 950 (1):67, June 2023. doi: 10.3847/1538-4357/acc846.

Lulu Fan, Suzy F. Jones, Yunkun Han, and Kirsten K. Knudsen. The SCUBA-2 850 $\mu$m Follow-up of WISE-selected, Luminous Dust-obscured Quasars. *PASP*, 129(982):124101, December 2017. doi: 10.1088/1538-3873/aa8e91.

R. G. Bower, A. J. Benson, R. Malbon, J. C. Helly, C. S. Frenk, C. M. Baugh, S. Cole, and C. G. Lacey. Breaking the hierarchy of galaxy formation. *MNRAS*, 370(2):645–655, August 2006. doi: 10.1111/j.1365-2966.2006.10519.x.

Chris A. Collins, John P. Stott, Matt Hilton, Scott T. Kay, S. Adam Stanford, Michael Davidson, Mark Hosmer, Ben Hoyle, Andrew Liddle, Ed Lloyd-Davies, Robert G. Mann, Nicola Mehrtens, Christopher J. Miller, Robert C. Nichol, A. Kathy Romer, Martin Sahlén, Pedro T. P. Viana, and Michael J. West. Early assembly of the most massive galaxies. *Nature*, 458(7238):603–606, April 2009. doi: 10.1038/nature07865.

Guinevere Kauffmann, Jörg M. Colberg, Antonaldo Diaferio, and Simon D. M. White. Clustering of galaxies in a hierarchical universe - II. Evolution to high redshift. *MNRAS*, 307(3):529–536, August 1999. doi: 10.1046/j.1365-8711.1999.02711.x.

N. Scoville, H. Aussel, M. Brusa, P. Capak, C. M. Carollo, M. Elvis, M. Giavalisco, L. Guzzo, G. Hasinger, C. Impey, J. P. Kneib, O. LeFevre, S. J. Lilly, B. Mobasher, A. Renzini, R. M. Rich, D. B. Sanders, E. Schinnerer, D. Schminovich, P. Shopbell, Y. Taniguchi, and N. D. Tyson. The Cosmic Evolution Survey (COSMOS): Overview. *ApJS*, 172(1):1–8, September 2007. doi: 10.1086/516585.

M. Schirmer. THELI: Convenient Reduction of Optical, Near-infrared, and Mid-infrared Imaging Data. *ApJS*, 209(2):21, December 2013. doi: 10.1088/0067-0049/209/2/21.

Gaia Collaboration, A. Vallenari, A. G. A. Brown, T. Prusti, J. H. J. de Bruijne, F. Arenou, C. Babusiaux, M. Biermann, O. L. Creevey, C. Ducourant, D. W. Evans, L. Eyer, R. Guerra, A. Hutton, C. Jordi, S. A. Klioner, U. L. Lammers, L. Lindegren, X. Luri, F. Mignard, C. Panem, D. Pourbaix, S. Randich, P. Sartoretti, C. Soubiran, P. Tanga, N. A. Walton, C. A. L. Bailer-Jones, U. Bastian, R. Drimmel, F. Jansen, D. Katz, M. G. Lattanzi, F. van Leeuwen, J. Bakker, C. Cacciari, J. Castañeda, F. De Angeli, C. Fabricius, M. Fouesneau, Y. Frémat, L. Galluccio, A. Guerrier, U. Heiter, E. Masana, R. Messineo, N. Mowlavi, C. Nicolas, K. Nienartowicz, F. Pailler, P. Panuzzo, F. Riclet, W. Roux, G. M. Seabroke, R. Sordo, F. Thévenin, G. Gracia-Abril, J. Portell, D. Teyssier, M. Altmann, R. Andrae, M. Audard, I. Bellas-Velidis, K. Benson, J. Berthier, R. Blomme, P. W. Burgess, D. Busonero,

G. Busso, H. Cánovas, B. Carry, A. Cellino, N. Cheek, G. Clementini, Y. Damerdji, M. Davidson, P. de Teodoro, M. Nuñez Campos, L. Delchambre, A. Dell'Oro, P. Esquej, J. Fernández-Hernández, E. Fraile, D. Garabato, P. García-Lario, E. Gosset, R. Haigron, J. L. Halbwachs, N. C. Hambly, D. L. Harrison, J. Hernández, D. Hestroffer, S. T. Hodgkin, B. Holl, K. Janßen, G. Jevardat de Fombelle, S. Jordan, A. Krone-Martins, A. C. Lanzafame, W. Löffler, O. Marchal, P. M. Marrese, A. Moitinho, K. Muinonen, P. Osborne, E. Pancino, T. Pauwels, A. Recio-Blanco, C. Reylé, M. Riello, L. Rimoldini, T. Roegiers, J. Rybizki, L. M. Sarro, C. Siopis, M. Smith, A. Sozzetti, E. Utrilla, M. van Leeuwen, U. Abbas, P. Ábrahám, A. Abreu Aramburu, C. Aerts, J. J. Aguado, M. Ajaj, F. Aldea-Montero, G. Altavilla, M. A. Álvarez, J. Alves, F. Anders, R. I. Anderson, E. Anglada Varela, T. Antoja, D. Baines, S. G. Baker, L. Balaguer-Núñez, E. Balbinot, Z. Balog, C. Barache, D. Barbato, M. Barros, M. A. Barstow, S. Bartolomé, J. L. Bassilana, N. Bauchet, U. Becciani, M. Bellazzini, A. Berihuete, M. Bernet, S. Bertone, L. Bianchi, A. Binnenfeld, S. Blanco-Cuaresma, A. Blazere, T. Boch, A. Bombrun, D. Bossini, S. Bouquillon, A. Bragaglia, L. Bramante, E. Breedt, A. Bressan, N. Brouillet, E. Brugaletta, B. Bucciarelli, A. Burlacu, A. G. Butkevich, R. Buzzi, E. Caffau, R. Cancelliere, T. Cantat-Gaudin, R. Carballo, T. Carlucci, M. I. Carnerero, J. M. Carrasco, L. Casamiquela, M. Castellani, A. Castro-Ginard, L. Chaoul, P. Charlot, L. Chemin, V. Chiaramida, A. Chiavassa, N. Chornay, G. Comoretto, G. Contursi, W. J. Cooper, T. Cornez, S. Cowell, F. Crifo, M. Cropper, M. Crosta, C. Crowley, C. Dafonte, A. Dapergolas, M. David, P. David, P. de Laverny, F. De Luise, R. De March, J. De Ridder, R. de Souza, A. de Torres, E. F.

del Peloso, E. del Pozo, M. Delbo, A. Delgado, J. B. Delisle, C. Demouchy, T. E. Dharmawardena, P. Di Matteo, S. Diakite, C. Diener, E. Distefano, C. Dolding, B. Edvardsson, H. Enke, C. Fabre, M. Fabrizio, S. Faigler, G. Fedorets, P. Fernique, A. Fienga, F. Figueras, Y. Fournier, C. Fouron, F. Fragkoudi, M. Gai, A. Garcia-Gutierrez, M. Garcia-Reinaldos, M. García-Torres, A. Garofalo, A. Gavel, P. Gavras, E. Gerlach, R. Geyer, P. Giacobbe, G. Gilmore, S. Girona, G. Giuffrida, R. Gomel, A. Gomez, J. González-Núñez, I. González-Santamaría, J. J. González-Vidal, M. Granvik, P. Guillout, J. Guiraud, R. Gutiérrez-Sánchez, L. P. Guy, D. Hatzidimitriou, M. Hauser, M. Haywood, A. Helmer, A. Helmi, M. H. Sarmiento, S. L. Hidalgo, T. Hilger, N. Hładczuk, D. Hobbs, G. Holland, H. E. Huckle, K. Jardine, G. Jasniewicz, A. Jean-Antoine Piccolo, Ó. Jiménez-Arranz, A. Jorissen, J. Juaristi Campillo, F. Julbe, L. Karbevska, P. Kervella, S. Khanna, M. Kontizas, G. Kordopatis, A. J. Korn, Á. Kóspál, Z. Kostrzewa-Rutkowska, K. Kruszyńska, M. Kun, P. Laizeau, S. Lambert, A. F. Lanza, Y. Lasne, J. F. Le Campion, Y. Lebreton, T. Lebzelter, S. Leccia, N. Leclerc, I. Lecoeur-Taibi, S. Liao, E. L. Licata, H. E. P. Lindstrøm, T. A. Lister, E. Livanou, A. Lobel, A. Lorca, C. Loup, P. Madrero Pardo, A. Magdaleno Romeo, S. Managau, R. G. Mann, M. Manteiga, J. M. Marchant, M. Marconi, J. Marcos, M. M. S. Marcos Santos, D. Marín Pina, S. Marinoni, F. Marocco, D. J. Marshall, L. Martin Polo, J. M. Martín-Fleitas, G. Marton, N. Mary, A. Masip, D. Massari, A. Mastrobuono-Battisti, T. Mazeh, P. J. McMillan, S. Messina, D. Michalik, N. R. Millar, A. Mints, D. Molina, R. Molinaro, L. Molnár, G. Monari, M. Monguió, P. Montegriffo, A. Montero, R. Mor, A. Mora, R. Morbidelli, T. Morel, D. Morris, T. Muraveva,

C. P. Murphy, I. Musella, Z. Nagy, L. Noval, F. Ocaña, A. Ogden, C. Ordenovic, J. O. Osinde, C. Pagani, I. Pagano, L. Palaversa, P. A. Palicio, L. Pallas-Quintela, A. Panahi, S. Payne-Wardenaar, X. Peñalosa Esteller, A. Penttilä, B. Pichon, A. M. Piersimoni, F. X. Pineau, E. Plachy, G. Plum, E. Poggio, A. Prša, L. Pulone, E. Racero, S. Ragaini, M. Rainer, C. M. Raiteri, N. Rambaux, P. Ramos, M. Ramos-Lerate, P. Re Fiorentin, S. Regibo, P. J. Richards, C. Rios Diaz, V. Ripepi, A. Riva, H. W. Rix, G. Rixon, N. Robichon, A. C. Robin, C. Robin, M. Roelens, H. R. O. Rogues, L. Rohrbasser, M. Romero-Gómez, N. Rowell, F. Royer, D. Ruz Mieres, K. A. Rybicki, G. Sadowski, A. Sáez Núñez, A. Sagristà Sellés, J. Sahlmann, E. Salguero, N. Samaras, V. Sanchez Gimenez, N. Sanna, R. Santoveña, M. Sarasso, M. Schultheis, E. Sciacca, M. Segol, J. C. Segovia, D. Ségransan, D. Semeux, S. Shahaf, H. I. Siddiqui, A. Siebert, L. Siltala, A. Silvelo, E. Slezak, I. Slezak, R. L. Smart, O. N. Snaith, E. Solano, F. Solitro, D. Souami, J. Souchay, A. Spagna, L. Spina, F. Spoto, I. A. Steele, H. Steidelmüller, C. A. Stephenson, M. Süveges, J. Surdej, L. Szabados, E. Szegedi-Elek, F. Taris, M. B. Taylor, R. Teixeira, L. Tolomei, N. Tonello, F. Torra, J. Torra, G. Torralba Elipe, M. Trabucchi, A. T. Tsounis, C. Turon, A. Ulla, N. Unger, M. V. Vaillant, E. van Dillen, W. van Reeven, O. Vanel, A. Vecchiato, Y. Viala, D. Vicente, S. Voutsinas, M. Weiler, T. Wevers, Ł. Wyrzykowski, A. Yoldas, P. Yvard, H. Zhao, J. Zorec, S. Zucker, and T. Zwitter. Gaia Data Release 3. Summary of the content and survey properties. *A&A*, 674:A1, June 2023. doi: 10.1051/0004-6361/202243940.

J. R. Weaver, O. B. Kauffmann, O. Ilbert, H. J. McCracken, A. Moneti, S. Toft, G. Brammer, M. Shuntov, I. Davidzon, B. C. Hsieh,

C. Laigle, A. Anastasiou, C. K. Jespersen, J. Vinther, P. Capak, C. M. Casey, C. J. R. McPartland, B. Milvang-Jensen, B. Mobasher, D. B. Sanders, L. Zalesky, S. Arnouts, H. Aussel, J. S. Dunlop, A. Faisst, M. Franx, L. J. Furtak, J. P. U. Fynbo, K. M. L. Gould, T. R. Greve, S. Gwyn, J. S. Kartaltepe, D. Kashino, A. M. Koekemoer, V. Kokorev, O. Le Fèvre, S. Lilly, D. Masters, G. Magdis, V. Mehta, Y. Peng, D. A. Riechers, M. Salvato, M. Sawicki, C. Scarlata, N. Scoville, R. Shirley, J. D. Silverman, A. Sneppen, V. Smolcić, C. Steinhardt, D. Stern, M. Tanaka, Y. Taniguchi, H. I. Teplitz, M. Vaccari, W. H. Wang, and G. Zamorani. COSMOS2020: A Panchromatic View of the Universe to z 10 from Two Complementary Catalogs. *ApJS*, 258 (1):11, January 2022. doi: 10.3847/1538-4365/ac3078.

Željko Ivezić, Steven M. Kahn, J. Anthony Tyson, Bob Abel, Emily Acosta, Robyn Allsman, David Alonso, Yusra AlSayyad, Scott F. Anderson, John Andrew, James Roger P. Angel, George Z. Angeli, Reza Ansari, Pierre Antilogus, Constanza Araujo, Robert Armstrong, Kirk T. Arndt, Pierre Astier, Éric Aubourg, Nicole Auza, Tim S. Axelrod, Deborah J. Bard, Jeff D. Barr, Aurelian Barrau, James G. Bartlett, Amanda E. Bauer, Brian J. Bauman, Sylvain Baumont, Ellen Bechtol, Keith Bechtol, Andrew C. Becker, Jacek Becla, Cristina Beldica, Steve Bellavia, Federica B. Bianco, Rahul Biswas, Guillaume Blanc, Jonathan Blazek, Roger D. Blandford, Josh S. Bloom, Joanne Bogart, Tim W. Bond, Michael T. Booth, Anders W. Borgland, Kirk Borne, James F. Bosch, Dominique Boutigny, Craig A. Brackett, Andrew Bradshaw, William Nielsen Brandt, Michael E. Brown, James S. Bullock, Patricia Burchat, David L. Burke, Gianpietro

Cagnoli, Daniel Calabrese, Shawn Callahan, Alice L. Callen, Jeffrey L. Carlin, Erin L. Carlson, Srinivasan Chandrasekharan, Glenaver Charles-Emerson, Steve Chesley, Elliott C. Cheu, Hsin-Fang Chiang, James Chiang, Carol Chirino, Derek Chow, David R. Ciardi, Charles F. Claver, Johann Cohen-Tanugi, Joseph J. Cockrum, Rebecca Coles, Andrew J. Connolly, Kem H. Cook, Asantha Cooray, Kevin R. Covey, Chris Cribbs, Wei Cui, Roc Cutri, Philip N. Daly, Scott F. Daniel, Felipe Daruich, Guillaume Daubard, Greg Daues, William Dawson, Francisco Delgado, Alfred Dellapenna, Robert de Peyster, Miguel de Val-Borro, Seth W. Digel, Peter Doherty, Richard Dubois, Gregory P. Dubois-Felsmann, Josef Durech, Frossie Economou, Tim Eifler, Michael Eracleous, Benjamin L. Emmons, Angelo Fausti Neto, Henry Ferguson, Enrique Figueroa, Merlin Fisher-Levine, Warren Focke, Michael D. Foss, James Frank, Michael D. Freemon, Emmanuel Gangler, Eric Gawiser, John C. Geary, Perry Gee, Marla Geha, Charles J. B. Gessner, Robert R. Gibson, D. Kirk Gilmore, Thomas Glanzman, William Glick, Tatiana Goldina, Daniel A. Goldstein, Iain Goodenow, Melissa L. Graham, William J. Gressler, Philippe Gris, Leanne P. Guy, Augustin Guyonnet, Gunther Haller, Ron Harris, Patrick A. Hascall, Justine Haupt, Fabio Hernandez, Sven Herrmann, Edward Hileman, Joshua Hoblitt, John A. Hodgson, Craig Hogan, James D. Howard, Dajun Huang, Michael E. Hufer, Patrick Ingraham, Walter R. Innes, Suzanne H. Jacoby, Bhuvnesh Jain, Fabrice Jammes, M. James Jee, Tim Jenness, Garrett Jernigan, Darko Jevremović, Kenneth Johns, Anthony S. Johnson, Margaret W. G. Johnson, R. Lynne Jones, Claire Juramy-Gilles, Mario Jurić, Jason S. Kalirai, Nitya J. Kallivayalil, Bryce Kalmbach, Jeffrey P. Kantor, Pierre Karst, Mansi M. Kasliwal,

Heather Kelly, Richard Kessler, Veronica Kinnison, David Kirkby, Lloyd Knox, Ivan V. Kotov, Victor L. Krabbendam, K. Simon Krughoff, Petr Kubánek, John Kuczewski, Shri Kulkarni, John Ku, Nadine R. Kurita, Craig S. Lage, Ron Lambert, Travis Lange, J. Brian Langton, Laurent Le Guillou, Deborah Levine, Ming Liang, Kian-Tat Lim, Chris J. Lintott, Kevin E. Long, Margaux Lopez, Paul J. Lotz, Robert H. Lupton, Nate B. Lust, Lauren A. MacArthur, Ashish Mahabal, Rachel Mandelbaum, Thomas W. Markiewicz, Darren S. Marsh, Philip J. Marshall, Stuart Marshall, Morgan May, Robert McKercher, Michelle McQueen, Joshua Meyers, Myriam Migliore, Michelle Miller, David J. Mills, Connor Miraval, Joachim Moeyens, Fred E. Moolekamp, David G. Monet, Marc Moniez, Serge Monkewitz, Christopher Montgomery, Christopher B. Morrison, Fritz Mueller, Gary P. Muller, Freddy Muñoz Arancibia, Douglas R. Neill, Scott P. Newbry, Jean-Yves Nief, Andrei Nomerotski, Martin Nordby, Paul O'Connor, John Oliver, Scot S. Olivier, Knut Olsen, William O'Mullane, Sandra Ortiz, Shawn Osier, Russell E. Owen, Reynald Pain, Paul E. Palecek, John K. Parejko, James B. Parsons, Nathan M. Pease, J. Matt Peterson, John R. Peterson, Donald L. Petravick, M. E. Libby Petrick, Cathy E. Petry, Francesco Pierfederici, Stephen Pietrowicz, Rob Pike, Philip A. Pinto, Raymond Plante, Stephen Plate, Joel P. Plutchak, Paul A. Price, Michael Prouza, Veljko Radeka, Jayadev Rajagopal, Andrew P. Rasmussen, Nicolas Regnault, Kevin A. Reil, David J. Reiss, Michael A. Reuter, Stephen T. Ridgway, Vincent J. Riot, Steve Ritz, Sean Robinson, William Roby, Aaron Roodman, Wayne Rosing, Cecille Roucelle, Matthew R. Rumore, Stefano Russo, Abhijit Saha, Benoit Sassolas, Terry L. Schalk, Pim

Schellart, Rafe H. Schindler, Samuel Schmidt, Donald P. Schneider, Michael D. Schneider, William Schoening, German Schumacher, Megan E. Schwamb, Jacques Sebag, Brian Selvy, Glenn H. Sembroski, Lynn G. Seppala, Andrew Serio, Eduardo Serrano, Richard A. Shaw, Ian Shipsey, Jonathan Sick, Nicole Silvestri, Colin T. Slater, J. Allyn Smith, R. Chris Smith, Shahram Sobhani, Christine Soldahl, Lisa Storrie-Lombardi, Edward Stover, Michael A. Strauss, Rachel A. Street, Christopher W. Stubbs, Ian S. Sullivan, Donald Sweeney, John D. Swinbank, Alexander Szalay, Peter Takacs, Stephen A. Tether, Jon J. Thaler, John Gregg Thayer, Sandrine Thomas, Adam J. Thornton, Vaikunth Thukral, Jeffrey Tice, David E. Trilling, Max Turri, Richard Van Berg, Daniel Vanden Berk, Kurt Vetter, Francoise Virieux, Tomislav Vucina, William Wahl, Lucianne Walkowicz, Brian Walsh, Christopher W. Walter, Daniel L. Wang, Shin-Yawn Wang, Michael Warner, Oliver Wiecha, Beth Willman, Scott E. Winters, David Wittman, Sidney C. Wolff, W. Michael Wood-Vasey, Xiuqin Wu, Bo Xin, Peter Yoachim, and Hu Zhan. LSST: From Science Drivers to Reference Design and Anticipated Data Products. *ApJ*, 873(2): 111, March 2019. doi: 10.3847/1538-4357/ab042c.